Optimization of Processing Parameters and Development of a Radon Trapping System for the NEWS-G Dark Matter Detector

by

Patrick O'Brien

A thesis submitted in partial fulfillment of the requirements of for the degree of

Master of Science

Department of Physics
University of Alberta

Abstract

The direct detection for a dark matter particle is reaching increasingly lower sensitivities and the New Experiments With Spheres-Gas (NEWS-G) collaboration is one of the experiments at the forefront of this. Currently being installed at SNOLAB two kilometres underground, the Spherical Proportional Counter (SPC) used by NEWS-G is designed to detect Weakly Interacting Massive Particles (WIMPs) with a mass less than 1 GeV/c^2, with a corresponding cross-section of $10^{-}41$ cm^2. A calibration run using pure methane was commissioned at the Laboratoire Souterrain de Modane (LSM) using ^{37}Ar, a radioactive gas with two well-characterized decay energies (270 eV and 2.8 keV). The signals from these decay events within the volume of the detector can then be analyzed to accurately map the energy of an event to the detector response. In the presented work, I optimized several processing parameters to ensure the characteristic values from the signals are accurate. In addition, I designed and constructed a radon trapping system in the Piro Lab at the University of Alberta to find the optimal conditions and material to trap radon from detector gases for the NEWS-G experiment at SNOLAB. A closed-loop circulation system was constructed to test two radon trapping materials: Carboxen® 1000 (Sigma Aldrich) and silver zeolite produced by Extraordinary Adsorbents, a company based in Edmonton, Canada. The radon adsorption in nitrogen, argon, and an argon-methane mixture at ambient and dry ice temperatures was then measured, and the performance of each material with different combinations of the above parameters was determined and compared.

Preface

The work done in this thesis is my personal contribution to the NEWS-G collaboration while at the University of Alberta (UofA) under the supervision of Dr. Marie-Cécile Piro. This collaboration is lead by Dr. Gilles Gerber at Queen's University, while Dr. Marie-Cécile Piro is the Principal Investigator for the collaboration at the UofA. It is divided among two projects, the details and results of which are highlighted in Chapter 4, Chapter 5, and Chapter 6. The processing methods described in Chapter 4 was done with the assistance of Daniel Durnford, and the analysis was my original work. There was also input from Francisco Vazquez de Sola when defining the intended analysis goals.

Chapter 5 and Chapter 6 involves the design, construction, and testing of the Radon Trapping System (RTS). I was responsible for the design, construction, testing, and analysis of this system. Elements of the trap design were taken from the NEWS-G gas handling system, with important information and discussions provided by Dr. Philippe Gros and Sean Crawford. Yuqi Deng, Carter Garrah, Daniel Durnford, and Dr. Marie-Cécile Piro assisted in the data collection and maintaining the temperature of the trap during testing.

To grandma. Thank you for all of the letters.

"Remember kids, the only difference between screwing around and science is writing it down."
Adam Savage, 2012

Acknowledgements

In physics, it is said that we stand on the shoulders of giants, and there are many giants in my life without whom I could have not succeeded in this degree. There have been many challenges throughout the last two years, including a pandemic that brought the world to a standstill, but research continued nonetheless. This was only done through the help of my colleagues Daniel, Yuqi, and Carter, who provided excellent conversations, technical assistance, and answered many late-night and early-morning questions. The NEWS-G collaboration is also to thank for providing me with multiple projects along with support and opportunities to share my research. During this graduate degree, I have met many incredible people that have supported me and who I owe many thanks. First and foremost I would like to thank Zoe for being incredibly supportive, understanding, and cooperative while I have worked through this degree. She has brought a lot of joy into my life and has kept me healthy and sane. Her family has also become my second family, and I am eternally thankful for them allowing me to escape from the city and spend time with some animals. I would like to thank Brittany for being one of my first friends in Edmonton, and for always being kind and understanding. Our conversations always helped me feel more comfortable with my decisions. I also want to thank Sean for the in-depth talks about anything under the sun, along with the board games, and for always providing cute pictures of your animals. Thank you also to Max, Zoë, and Owen for providing some much-needed down(force)time throughout the last two years, and I hope our traditions continue. I also hope traditions continue with Margaret, Leon, Roger, and the rest of the gang in which cooking plays a central role. As a former member of the GPSA, I would like to thank everyone with who I worked for their camaraderie and energy. A special thanks to Bruce Sutherland for inspiring me in his class and showing me that there is more I can do with physics than previously thought. Thank you also to my supervisory committee for ensuring that I stayed on the right track, and to Craig for some important conversations.

Finally, I would like to thank my supervisor Marie-Cécile for supporting me and advocating for me when needed. She was able to teach me how to think critically and communicate well in an academic manner while introducing me to many new concepts. Along with reading this thesis multiple times, she continually encouraged me to work hard, posed many challenging questions, and ultimately taught me to chase only one rabbit at a time.

Contents

List of Tables

List of Figures

List of Abbreviations

Abbreviation	Meaning
DM	Dark Matter
CMB	Cosmic Microwave Background
RTS	Radon Trapping System
NEWS-G	New Experiments With Spheres - Gas
WIMP	Weakly Interacting Massive Particle
SPC	Spherical Proportional Counter
LSM	Laboratoire Souterrain de Modane
RT	Room Temperature
DI	Dry Ice
GHS	Gas Handling System
BGA	Binary Gas Analyzer
UofA	University of Alberta
DAQ	Data Acquisition

Chapter 1

Introduction

The presence of invisible mass in the universe has been known for over a century, with much of the evidence coming from astronomical observations [1]. This invisible mass is referred to as dark matter (DM), and it has been proposed to take a variety of forms. The hypotheses about DM have significantly progressed since its first introduction and collaborations are striving to discover a DM particle. The New Experiments With Spheres - Gas (NEWS-G) experiment is one such collaboration aimed at detecting Weakly Interacting Massive Particles (WIMPs), a proposed DM particle candidate. This experiment has been designed to search for low-mass WIMPs through the use of a gas-filled Spherical Proportional Counter (SPC). Several tests and a physics run were conducted with this device at the Laboratoire Souterrain de Modane (LSM) using pure methane [2]. Given that the NEWS-G experiment is a proportional counter, it is expected that the signal produced within the detector will be proportional to the energy of the event. To directly correlate the energy to the signal, analysis can be done based on events produced by radioactive elements placed in and around the detector. This process uses software to analyze the trace of the pulse and measures different significant values from each event signal. To ensure that the data produced from the pure methane run accurately reflects the original signal measured, several processing optimizations must be done. These optimizations can also be applied for the commissioning of the NEWS-G installation at the SNOLAB facility 2 kilometres underground.

This installation is configured for low-energy rare event searches, which require ultra-low background activity. This need provides many challenges for the construction and operation of the detector including the removal of radioactive contaminants from

the detector materials and gas. While work has been ongoing to remove radioactive contaminants like uranium-238 (^{238}U), thorium-232 (^{232}Th), and their progenitors, from the inner copper surface of the spherical detector, this thesis will present investigation techniques for radon mitigation in gas. Radon gas interferes with the operation of the detector when it decays and releases an alpha particle. This contributes to the background of the detector, which should be minimized to reach the intended sensitivities to WIMPs.

This thesis will expose the results of two different projects, providing optimal parameters and conditions for the NEWS-G experiment. To begin, Chapter 2 will lay out the history and discoveries concerning DM along with its characterization. The various DM candidates will be discussed, including methods to detect DM particles. Chapter 3 discusses all aspects of the NEWS-G DM detector. Originally designed to detect low-energy neutrons and hypothetical axions, the SPC has evolved to achieve high sensitivities using the forefront of material science while still featuring a reduced operational complexity. The following Chapter 4 delves into the work I did to optimize the processing parameters of the software system used to analyze signals from the detector. This was done to ensure that the detector can be accurately calibrated based on signals created by known radioactive sources.

Radon and its effects on the NEWS-G experiment are then discussed in Chapter 5 to motivate the research conducted in this thesis. The experimental setup and procedure are also outlined, including the different technologies used to collect data. Chapter 6 then outlines the different experiments performed to remove radon from the carrier gas and their respective results. Several conclusions are discussed from these findings and recommendations are made for the implementation of the radon mitigation system for the NEWS-G installation at SNOLAB.

Chapter 2

Dark Matter

2.1 Discovery of Missing Matter

2.1.1 Initial Discoveries

Towards the end of the nineteenth century, it was thought that physics was nearing completion as a science. Aside from edge cases like black body radiation, physics could be explained using classical mechanics. Today we know that there was a lot to be left to learn about physics [3]. During this period, William Thomson, better known as Lord Kelvin, argued that stars within the Milky Way galaxy should behave like particles in a gas that are influenced only by gravity[1]. For stars in hydrostatic equilibrium, which describes most galaxies, the mass of the collection of objects and its speed of rotation can be related. Based on the rotational velocity of the Milky Way, Lord Kelvin posited that many of the stars may be dark bodies [4]. The relationship between mass and rotational velocity proved to be a solid ground for research over the next century, and a plot in Figure 2.1 from 2000 confirms this relationship in the case of galaxies [5]. In 1906, Henri Poincaré discussed (and disagreed with) the work of Lord Kelvin in "The Milky Way and the Theory of Gases", in which the term "matière obscure" or "dark matter" in English, was used [6].

Several years after the suggestion of dark matter (DM) within the galaxy, some notable scientists began using the idea of measuring stellar velocities to investigate the presence of DM. Two Dutch astronomers, Jacobus Kapteyn and his student Jan

[1]It is now known that there are collections of stars and other materials similar to our own Milky way, namely galaxies

Oort used separate observations of nearby stars (on the scale of the galaxies) to theorize the motion of the stars and the density of matter [7] [8]. While it was still thought that DM consisted of faint stars, the work of Kapteyn, Oort, and others opened the door for researching the invisible masses in the universe.

One year after Oort published his aforementioned article, Fritz Zwicky made similar observations, but on the intergalactic scale. Through observations of the redshifts of galactic clusters (particularly the Coma cluster) made by Edwin Hubble and Milton Humason in 1931 [9], Zwicky applied the virial theorem to calculate the mass of the Coma cluster [10].

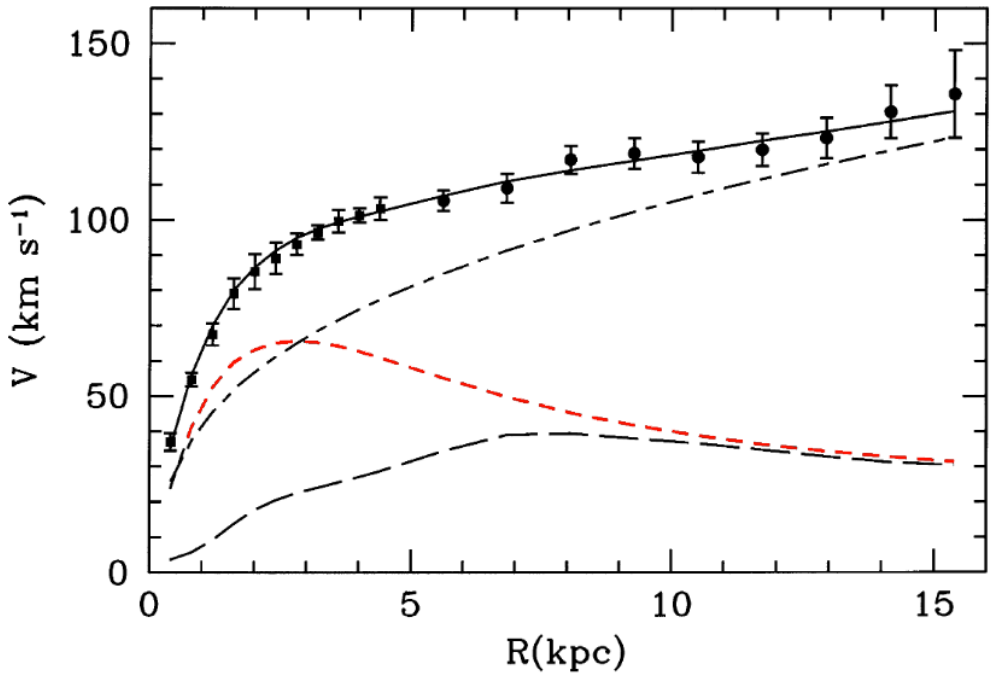

Figure 2.1: The various rotational velocities of the galaxy M33. The measured rotation curves of cold atomic gas are indicated by the dots, while the velocities from the best-fit model are the continuous solid line. The best-fit mass model arises from visible stars within the stellar disk, which is the largely Keplerian velocity curve; red dashed line. Contributions of mass from gas within the galaxy (long dashed line) is traced through electromagnetic radiation using radio and millimetre frequencies. A roughly spherical distribution of mass surrounding the galaxy known as the halo also contributes (dot-dashed line) to the best-fit model. There is insufficient baryonic mass to account for the observed mass of the halo [5].

The virial theorem originates in thermodynamics and relates the time-averaged total kinetic energy of a system of stable, discrete particles that are bound by po-

tential forces (like gravity), to the total potential energy of the system. The virial theorem is expressed as

$$\langle T \rangle = -\frac{1}{2} \sum_{k=1}^{N} \langle \mathbf{F}_k \cdot \mathbf{r}_k \rangle, \tag{2.1}$$

where $\mathbf{F}_k$ is the force acting on an individual particle, $\mathbf{r}_k$ is the position of the particle, both averaged over time. These variables, along with a numerical constant of $-\frac{1}{2}$, equate to $\langle T \rangle$, the time-averaged potential energy of the system.

Zwicky made several calculations based on astronomical observations, estimating that 800 galaxies were in the cluster, each with a mass of 10^9 solar masses, as proposed by Hubble [9]. Using the virial theorem, Zwicky found a velocity dispersion of 80 km/s based on his estimates. Using doppler-shift measurements of emission lines from nebulae, the actual velocity dispersion of the Coma cluster was found to be over 1000 km/s [10]. This result implies that the Coma cluster would have to be about 400 times denser than what is found based on luminous light. This light-producing matter is commonly referred to as baryonic matter, which consists of protons, neutrons, and every atom. Therefore, the existence of a non-luminous (non-baryonic), DM was once again proposed.

In 1937, Zwicky refined his calculations for the mass of the Coma cluster [11]. In doing so, the high mass-to-light ratio persisted, indicating that there was 500 times more mass in the Coma cluster than indicated by luminous mass. It is noted that these calculations used a Hubble constant of $H_0 = 558$ km/s/Mpc, which is inaccurate compared to the currently accepted value of $H_0 = 69.8 \pm 0.8$ (stat) ± 1.7 (sys) km/s/Mpc [12]. The value yielded by Zwicky can be divided by the ratio of the differing Hubble constants. This calculation gives a mass-to-light ratio of 60.8. This value is significantly lower than what Zwicky produced, but still provides evidence for invisible mass in the Coma cluster.

The work of Zwicky encouraged others to observe other large astronomical masses. Some of these people include Horace Babcock and (once again) Jan Oort. Babcock measured and discussed the rotation curves of the Andromeda galaxy [13], while Oort studied the large non-visible halo of the galaxy NGC 3115 [14]. The work from these two, and many more, provided mounting evidence for the existence of hidden mass.

2.1.2 Galactic Rotation Curves

Several decades after the initial work of Fritz Zwicky and others, Kent Ford and Vera Rubin used a new, more precise spectrograph to measure the velocity curves of edge-on spiral galaxies. While the methodology of converting the Doppler-shifted wavelengths to velocities had been done previously, Rubin and Ford could measure the velocities with greater precision. Paired with the work of Ken Freeman and their earlier work in 1970 [15], Ruben, Ford, and Norbert Thonnard published their results in a 1980 paper. This publication conclusively indicated that most of the 21 galaxies observed contained non-luminous matter [16].

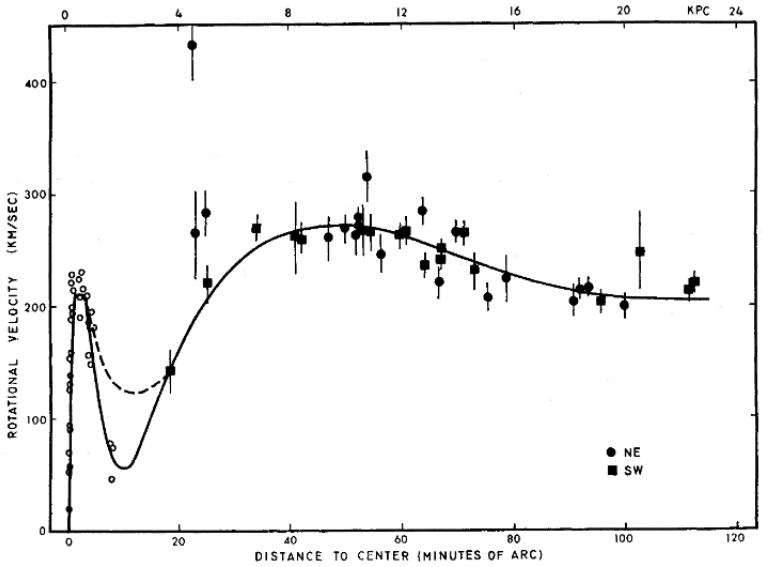

Figure 2.2: Plot of rotational velocities observed in the Andromeda galaxy based on radius from spectroscopic measurements. The solid line is a fit of the rotation curve using a: fifth-order polynomial fit for $R \leq 12'$; fourth-order polynomial for $R > 12'$. The dashed curve is a different rotation curve obtained using a higher inner minimum. The hollow dots are from N II regions, while the remaining filled points come from O or early-type B stars (grouped together as OB associations [15].

To determine the velocity curve of a galaxy, observations of H II regions (regions of interstellar ionized hydrogen) and N II (ionized nitrogen gas) regions were made with a spectrograph. These regions are distributed throughout the M31 galaxy, providing information at differing radii from the galactic core. Using the more precisely determined (compared to Babcock [13]) Doppler-shifted wavelengths measured from each of 67 H II regions, Rubin *et al.* could better determine the velocities of these regions based on the measured redshift (or blueshift) from the ionized gas regions.

The resulting velocities from these calculations are plotted in Figure 2.2. The gravitational force experienced by these gas regions can be inferred from the velocities, and the variance of the velocities from the Keplerian model indicates a contribution of mass greater than that of just the visible mass. In Figure 2.2, the velocity of the measured gas clouds remain relatively flat, instead of following the Keplerian model from just the visible mass like the one presented in Figure 2.1.

2.1.3 Gravitational Lensing

Other evidence for DM also exists aside from galactic rotation curves. Through the use of telescopes like the Hubble Space Telescope, the effects of gravitational lensing can be well observed.

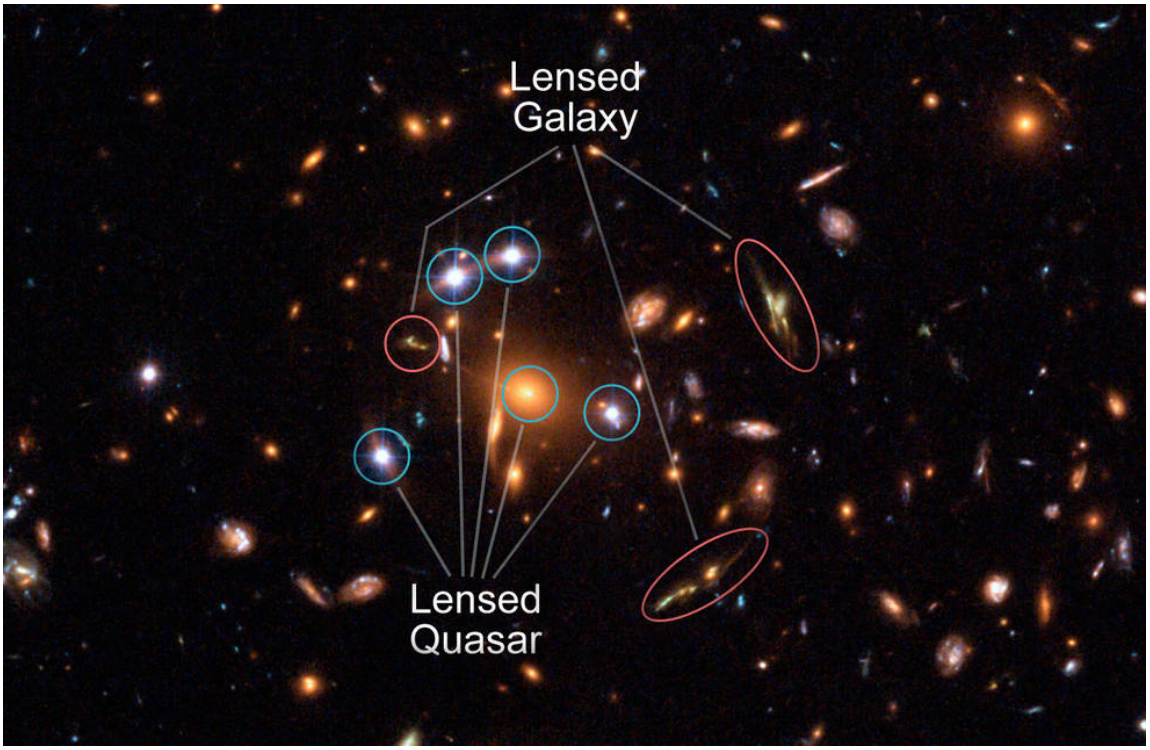

Figure 2.3: Gravitationally lensed light captured by the Hubble Space Telescope. Multiple images of the same astronomical bodies behind the lensing mass are visible. The quasar is SDSS J1004+4112 [17].

Gravitational lensing occurs around massive objects, like galaxies or black holes, when light passes through spacetime that has been warped by the gravitational field. While gravitational lensing can occur around any object with mass, more massive objects have a larger influence on nearby passing light. In general, light is deflected

by the mass, and the degree of deflection depends on the mass of the object. This allows light directly behind an astronomical body to be seen on the other side. Gravitational lensing can also create multiple images of the same object as shown in Figure 2.3.

Since the deflection of light depends on the mass, calculations based on General Relativity can be made to determine the expected lensing effect from the luminous mass. In the case of Figure 2.3, the quasar SDSS J1004+1422 is lensed by a galactic cluster. Based solely on the luminous mass, the separation between images of the quasar are too far apart. This implies that DM must be present in the galactic cluster for the quasar images to be where they were observed [18].

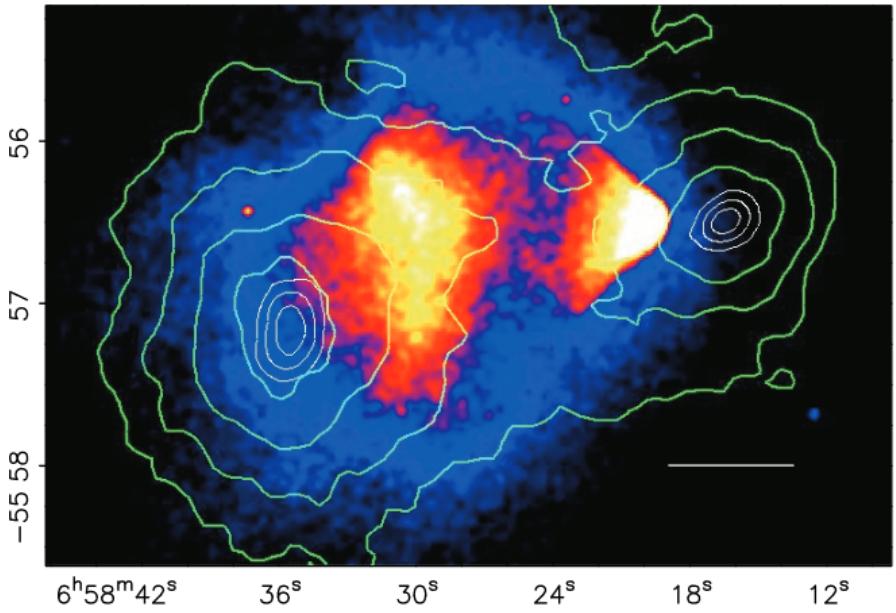

Figure 2.4: The Bullet Cluster as imaged by the Chandra X-ray Observatory. The green contours indicate the gravitational potential and were constructed through measurements of weak lensing. The white scale bar is a distance of 200 kpc. The gradient from white to blue indicates the intensity of X-rays from the collision [19].

The Bullet Cluster is another example where gravitational lensing indicates the existence of DM. In Figure 2.4, large regions of plasma created from the collision of two gas clouds are shown from their emitted X-rays. The colliding gases slowed down due to frictional forces, heating in the process. Weak gravitational lensing does not produce significant shifts in the path of light like multiple images of objects produced in Figure 2.3. Instead, the deflection of light is not measured based on one background source, but with minor distortions in the light passing close to

large masses. The deflections can then be used to infer the mass of the astronomical structures. For the Bullet Cluster, the DM only interacts through the gravitational force, meaning that it is able to pass through (essentially) without collision. The X-rays emitted from the colliding baryonic matter (which is at a temperature of 10^6 K) allowed for the calculation of the centre-of-mass (COM) for the visible matter allowing it to be compared to the total COM. The result from this comparison indicates that the total mass of the system (dark matter and X-ray producing components) is seven times greater than that of just the plasma (X-ray producing) mass. While this is the observed mass ratio, certain models (such as with constant acceleration) indicate the true ratio can be as high as 49:1 (total mass: plasma mass) [19].

2.1.4 Cosmic Microwave Background

Evidence for DM from the Cosmic Microwave Background (CMB) also exists in the form of anisotropies. When the universe had sufficiently cooled after the Big Bang, the combination of electrons and nuclei could occur, forming atoms. During this period of recombination, thermal radiation was no longer significantly scattered through Thomson scattering, causing the Universe to become transparent to photons. The CMB was created from the last-scattered photons and reflects the state of the Universe at this time.

Observations of the CMB indicate that it is nearly isotropic at a temperature of 2.728 ± 0.004 K [20]. There are minute microKelvin (μk) fluctuations from this isotropic background, referred to as anisotropies. These anisotropies hint at the gravitational influence that DM had during this period. In Figure 2.5, the power spectrum of the CMB at differing angular scales is shown, with three notable peaks. The first two acoustic peaks (around $\ell = 200, \ell = 500$, respectively) indicate the effects of baryonic matter including the pressure of the matter when the universe became transparent. The third prominent peak ($\ell = 800$) is described from DM, which is unaffected by baryonic pressure due to a lack of electromagnetic interaction.

The comparison of the relative amplitudes of the peaks can be used to determine the density of baryonic and DM. From the Planck Collaboration [21], the densities found were:

$$\text{Dark matter density} : \Omega_c h^2 = 0.120 \pm 0.001 \tag{2.2}$$

$$\text{Baryon density} : \Omega_b h^2 = 0.0224 \pm 0.0001 \tag{2.3}$$

The value of h ($= \frac{H_0}{100}$[km/s/Mpc]) is the reduced Hubble constant, which is used to normalize the baryon density Ω_b and dark matter density Ω_c. From the values found, the density of DM in the universe is about five times greater than that of baryonic matter.

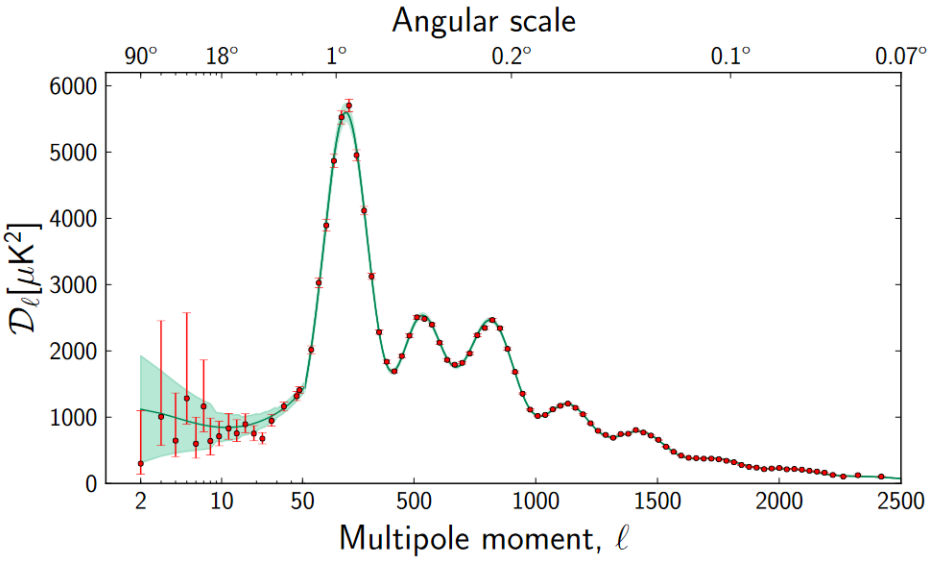

Figure 2.5: The power spectrum of the CMB with respect to the angular scale. The temperature fluctuations on the y-axis are based on microKelvins [22].

Current estimates from the Planck collaboration suggest that DM constitutes about 27% of the mass-energy density of the universe. Baryonic matter makes up only 5%, while dark energy is proposed as the remaining 68% [23]. From the astronomical observations of DM, the ΛCDM cosmological model arises. Λ indicates the cosmological constant in Einstein's field equations (of General Relativity) that represents dark energy, while CDM refers to Cold Dark Matter. To be considered cold, DM is non-relativistic and non-baryonic. If DM is relativistic, it is referred to as Hot Dark Matter (HDM). Warm DM also exists, but that is outside the scope of this thesis.

2.2 Dark Matter Candidates

There were (and are) numerous hypotheses about what constitutes DM as shown in Figure 2.6. Suggestions included interstellar gas [24] [25], but those findings were nullified in 1971 by Meekins *et al.*. Here, they state that the mass of the hot intracluster gas makes up less than 2% of the mass needed to describe the

gravitational binding [26]. Other proposals for DM included Massive Astrophysical Compact Halo Objects (MACHOs), which encompass black holes, neutron stars, brown dwarfs, disassociated planets, white dwarfs, and very dim red giants.

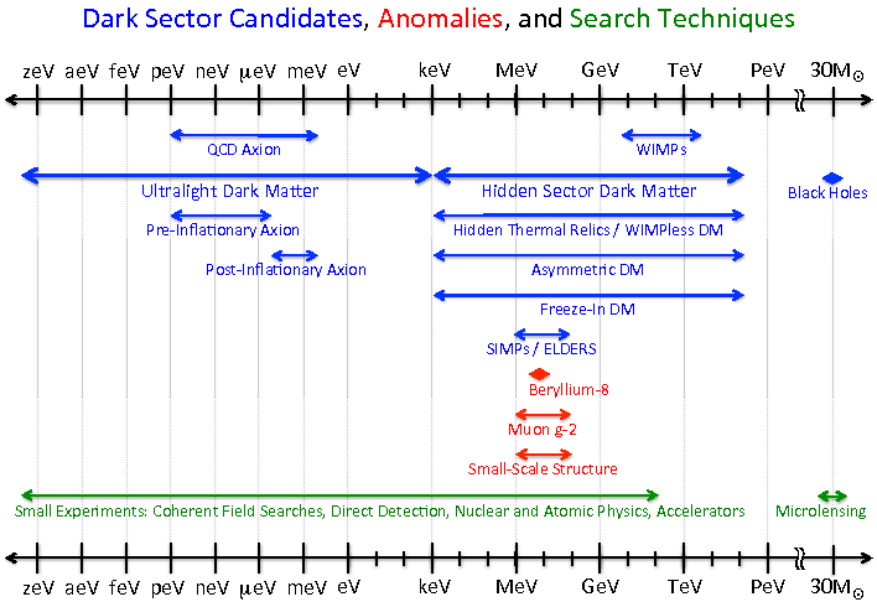

Figure 2.6: A chart indicating the mass ranges of various DM candidates [27].

In contrast, there are a variety of hypotheses that suggest DM is composed of an elementary particle (or particles). Neutrinos are one such example that have already been discovered. Weakly Interacting Massive Particles (WIMPs) are another particle that have yet to be discovered, and will be the subject of discussion in this thesis. Details about these as-of-yet undiscovered particles begin in Section 2.2.3.

Axions are another type of proposed DM particle predicted to be less massive and have significantly smaller cross-sections than WIMPs. The concept of an axion arises from the absence of strong charge parity (CP) violation and represents another form of CDM. Axions may also undergo slight interactions with photons in a strong magnetic field [28], but further discussion of this type of particle is outside the scope of this writing.

2.2.1 MACHOs

MACHOs are astronomical bodies that emit little or no electromagnetic radiation, making them invisible to distant observers. The referral to MACHOs as "halo objects" means that these objects are expected to be found in the halo regions of spiral galaxies, located outside of the main luminous zone [29].

An object like a black hole, when not located close to any visible matter, will be a true dark body, such that no light is emitted and all light directed at the black hole is absorbed. For objects like black holes, or any type of MACHO, to constitute the amount of DM suspected to be present in galaxies, they would be observable through gravitational lensing. Microlensing was used in particular, which occurs when light is bent around objects dark objects, allowing them to be detected even though they do not emit light. Searches were conducted to observe microlensing in the Large Magellanic Cloud (LMC) and the Small Magellanic Cloud (SMC). Based on the results from those observations, the lensing events expected from MACHOs were not present [30] [31]. From these results, MACHOs are not able to account for all of the mass of DM deduced from the CMB.

2.2.2 Neutrinos

One of the most popular theories for DM candidates lies in the world of the very small. There are several elementary particles, both known and unknown, that have been suggested as DM candidates. The idea of DM as a particle first came to light when particle physicists became increasingly interested in the issues of missing mass that cosmologists and astronomers were experiencing. As mentioned with the CMB anisotropies and Bullet Cluster, no baryonic particle is likely a DM candidate [30] [23].

Non-baryonic matter is a form of matter that is not commonly found or interacted with on a day-to-day basis and sits on the edge of theory and experiments. Particles like neutrinos are non-baryonic matter, and have been studied since 1956, when they were first directly detected [32].

Neutrinos were early candidates for DM particles based on their known properties. Neutrinos only interact via the weak nuclear force and gravity, and are stable, long-lived particles. Their weak interactivity made them ideal to explain the observations of DM. In particular, a study by Gershstein and Zeldovich published in 1966 theorized the production of neutrinos during the big bang [33]. It is noted that only

the electron and muon neutrinos were known at the time. Using variables like the Hubble constant and considering the oldest stars observed, a mass of less than 400 eV (electron Volts) was predicted for neutrinos [33]. A lower limit on the order of 10 eV was also predicted for neutrinos to account for the total mass of all DM. At the time of this thesis, the upper limit of the neutrino mass is around 1.1 eV. This means that neutrinos do not have the required mass to account for DM observations [34]. In addition, neutrinos are relativistic particles and would be classified as HDM, which does not accurately describe the stability of large-scale structures.

2.2.3 WIMPs

The idea of Weakly Interacting Massive Particles (WIMPs) was first introduced in the 1980s as the hypothesis of non-baryonic DM became popular. A WIMP is cold DM and falls under the previously mentioned ΛCDM model. Unlike a neutrino or any other known Standard Model (SM) particle, there is no clear definition of a WIMP. The only properties used to characterize a WIMP are that it is a CDM particle that interacts through gravity and the weak nuclear force. A weak force interaction involving the elastic scattering between a WIMP and baryonic matter is a potential method for detecting such particles. An example of a nuclear recoil reaction is shown in the Feynman diagram in Figure 2.7.

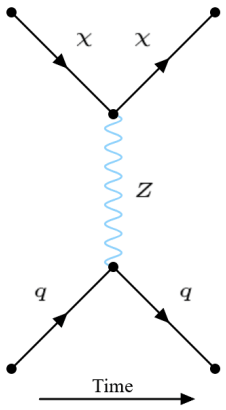

Figure 2.7: Feynman diagram of a predicted nuclear recoil from a DM particle. In this instance, the mediating force is the weak force, carried by the neutral Z boson. χ represents a DM particle, while q represents a quark in a nucleus.

While WIMPs remain a strong candidate as a DM particle, the effort to detect these elusive particles has been ongoing for forty years, as of 2021. These global efforts to search for WIMPs are becoming increasingly complex, using dif-

ferent methods for both indirect and direct detection of WIMPs. In 1984, Andrzej Drukier proposed that WIMPs could elastically scatter off of a nucleus [35]. Since then, advances in DM detection have been steadily progressing.

2.3 Search for WIMPs

There are three different methods in which WIMPs can be detected: indirect detection, production in colliders, and direct detection. Indirect detection concerns the observation of astronomical events, while the latter two methods involve processes taking place on Earth. WIMPs may be produced in high-energy collisions, such as those produced at the Large Hadron Collider (LHC). Meanwhile, direct detection is based on observations of nuclear recoil events initiated by a WIMP interaction. These three types of interactions are shown as a generic Feynman diagram in Figure 2.8.

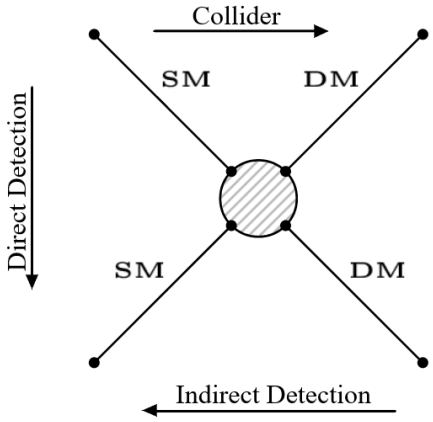

Figure 2.8: A Feynman diagram for DM interactions by direct searches, indirect searches, and collider productions. Changing the placement of the time axis (arrows) determines the type of interaction being described [36].

2.3.1 Indirect Detection and Collider Production

Indirect detection involves observations of unique phenomena by astronomers and cosmologists. WIMP searches of this type scan for excess Standard Model (SM) particles that may be produced from WIMP decay or annihilation. Particles like neutrinos, various energies of electromagnetic radiation, and charged cosmic rays could result from DM interactions.

By observing areas of the universe where DM congregates, like the centre of a galaxy, excess signals from particles with specific energies may be detected as indicators of WIMP decay or annihilation. Gamma rays, X-rays, and charged particles are being observed from various galactic cores to monitor for such events [37] [38]. There may exist events that would mimic a possible WIMP signal, requiring multiple measurements to confirm the existence of WIMPs [1]. A measurement from the Fermi Large Area Telescope provided strong evidence for WIMP annihilation by observing 130 GeV gamma photons, which may imply a DM mass of $m_\chi = 129.8 \pm 2.4^{+7}_{-3}$ GeV and a DM-DM partial annihilation cross-section of $(1.27 \pm 0.32^{+0.18}_{-0.28}) \times 10^{-27} \mathrm{cm}^3\mathrm{s}^{-1}$ [39]. This measurement is based on 50 detected photons, and several more years of data taking are required for a conclusive result.

Another region where WIMPs may congregate is the centre of the Sun. The annihilation or decay of a WIMP within the Sun may release a high-energy neutrino, which could be measured on Earth with a neutrino observatory. Experiments like AMANDA-II and IceCube are searching for these events [40].

The detection of DM particles may also occur in particle accelerators. In the Large Hadron Collider (LHC), proton-proton collisions could produce a DM particle, which would not be directly detected by the various LHC particle detectors. Since a WIMP has a low probability of interacting, other products from the WIMP production could instead be measured. If collision products are found to have significant amounts of missing energy and momentum, then a WIMP may have also been produced [41]. These production channels would have to be confirmed through other direct or indirect detections.

2.3.2 Direct Detection

Direct detection does not require astronomical observations or the production of WIMPs. Instead, it relies on a WIMP to pass through a dark matter detector. For direct detection to occur, the WIMP must undergo an interaction with baryonic matter, allowing the effects of the interaction to be observed. This tends to be in the form of a nuclear recoil, through spin-independent or spin-dependent interactions with a nucleus [42]. Spin-independent events do not depend on the spin of a nucleon and can lead to an increased cross-section due to other nucleons coherently contributing to the interaction. Spin-dependence is influenced by the net spin of the nucleons involved, which may lead to a smaller cross-section [43].

In 1986, the first experiment involving the direct detection of WIMPs placed the first measured constraints on the cross-section of a nucleus interaction. The experiment, based in the Homestake Mine in the United States of America (USA), was a joint effort between several American institutions and universities [44]. This experiment used a low-background germanium ionization detector originally designed to search for double beta decay and excluded DM particles between 20 GeV and 1 TeV.

Since that experiment in 1986, the upper limit for the cross-section and mass of a WIMP has been gradually reduced. The plot shown in Figure 2.9 demonstrates the work done by previous detectors of WIMPs. On the x-axis is the mass of a WIMP, and the y-axis shows the WIMP-nucleon cross-section. The cross-section can be thought of as the probability of an interaction between two particles. In this case, the WIMP-nucleon cross-section is less than 10^{-40}cm^2. The various lines within this plot show the results from different experiments, which have eliminated higher masses and cross-section values. The neutrino floor is a prominent aspect of the plot, indicated by the orange dashed line and yellow fill. Below this floor, detected WIMPs would have the same signals as neutrinos, making it difficult to distinguish between events from the two particles [45].

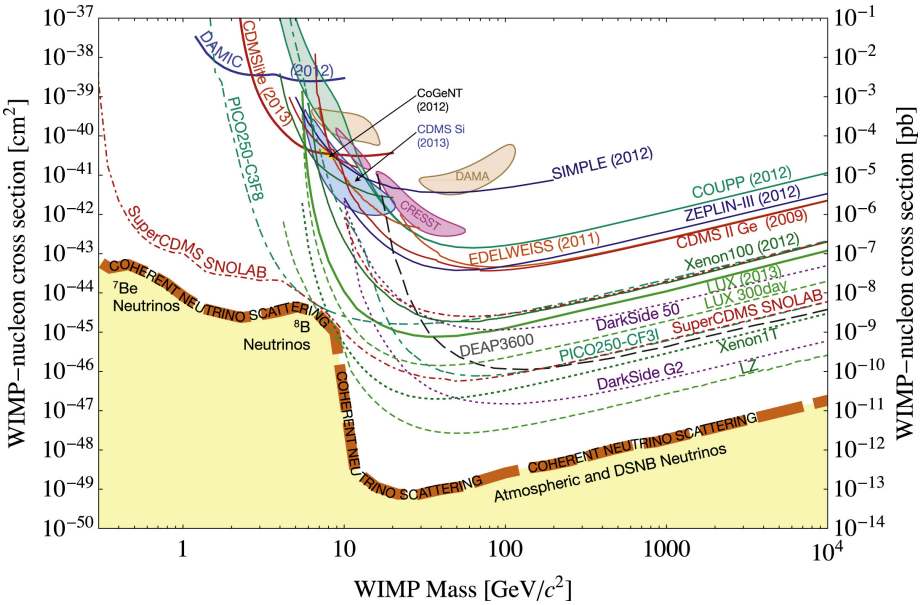

Figure 2.9: Upper limits on the cross-sectional area of a WIMP versus its mass. The different labeled lines indicate past and current experiments and their sensitivity to WIMPs. Further to the bottom left corner requires greater sensitivity. Areas above and to the right of the coloured lines have been ruled out as potential WIMP masses and cross-sections. The neutrino floor is represented as the yellow area [46].

2.3.3 Direct Detection Technologies

New low-mass detectors are being designed with cutting-edge technology to limit background sources, while still detecting a reliable signal for low energy events. These new and upcoming detectors are being produced with the help of advanced material science combined with improved design and construction techniques. Common methods being used for direct detection will be highlighted throughout the next several paragraphs. Given that there is a wide variety of detector technologies, many of the detectors are complementary to each other. Two different detectors with similar mass and cross-section detection ranges for WIMPs are able to provide support for one another should both detect a WIMP.

Cryogenic crystal detectors use the properties of super-cooled semiconductors to produce phonons and ionized charges to detect a nuclear recoil. These semiconductors are super-cooled to limit the amount of thermal energy in the system, creating an environment sensitive to small disturbances. When a WIMP-caused nuclear recoil occurs within the crystal, phonons are created in the crystal structure and can be recorded with thermal sensors. Electrons are also freed, leaving positively charged holes. The entire crystal has a voltage bias, allowing signals to also be produced from a changing current. Super Cryogenic Dark Matter Search (SuperCDMS), an example of this type of DM detector, is able to detect nuclear recoils as low as 10 eV, corresponding to a WIMP mass on the order of 1 GeV/c^2. At 1 GeVc^2, the expected cross-section is around 1×10^{-43}cm^2 [47].

Bubble chambers are designed with the idea of a liquid in a superheated state that undergoes a phase transition when energy is deposited into the active mass. This deposition of energy, if above a certain threshold, creates a nucleation sight within the fluid. Depending on the distance or number of interactions over which the energy is deposited, one or multiple bubbles can then be detected using cameras and acoustic sensors. PICO, which merged the PICASSO (Project In CAnada to Search for Supersymmetric Objects) and the COUPP (Chicagoland Observatory for Underground Particle Physics) collaborations, is an application of this technology. In the PICO detector, a superheated fluorocarbon is used as the active medium. The nucleation event depends on a threshold energy set by the pressure and temperature of the fluid. With this technology, PICO detectors can detect a WIMP with a mass on the order of 10 GeV and a cross-section of 3×10^{-41} cm^2 [48].

Noble gas scintillators convert an interaction between a particle and a nucleus

into a released photon. Depending on the wavelength of the photons produced, they can then be shifted to an appropriate wavelength that can be detected by a photodetector. Based on the arrival time of light to different photodetectors, the energy and type of interaction can be reconstructed. The DEAP-3600 (Dark matter Experiment using Argon Pulse-shape discrimination) uses 3600 kg of liquid argon as the scintillation material surrounded by 255 photomultiplier tubes (PMTs), with a wavelength shifter in between. The signal produced from a particle interaction in the argon then undergoes pulse-shape discrimination to remove background signals, and isolate possible WIMP events [49]. The DEAP-3600 detector is sensitive to a WIMP mass on the order of 50 GeV/c^2. For a WIMP mass of 100 GeV/c^2, a cross-section of 10^{-46}cm^2 is expected. A combination of a scintillating fluid and a bubble chamber technique, referred to as a Scintillating Bubble Chamber, is being researched by the SBC collaboration [50].

Spherical proportional counters (SPCs) consist of a metal, gas-filled sphere held at a high voltage from a central probe. SPCs are designed to maximize the volume-to-surface-area ratio of a detector since larger volumes have a higher chance of detecting a rare event. In an SPC, a nuclear recoil will ionize an atom. Since the sphere is held at a high voltage, the freed electron will drift towards the center of the detector. As the electron gains energy, it frees other electrons, creating a Townsend avalanche. The newly created positive ions then drift away from the anode, and the resulting change in the electric field is recorded as a signal. The avalanche of electrons has a negligible effect on the signal [51]. The New Experiments With Spheres - Gas (NEWS-G) DM detector is an SPC and is the subject of this thesis. The NEWS-G detector is designed to search for rare events, with the capability of detecting a WIMP mass as low as 0.1 GeV/c^2. The NEWS-G installation at the Sudbury Neutrino Observatory Laboratory (SNOLAB) has a predicted lower limit for WIMP mass and cross-section, as shown in Figure 2.10.

All of the aforementioned detectors are found or will be installed, at the SNOLAB facility in Sudbury, Ontario. This facility is located two kilometres underground. A large amount of rock above the facility creates a water equivalent of over six kilometres of shielding from cosmic radiation. The entire facility is also a clean room, providing an environment for low-background studies that is ideal when conducting rare event searches [52].

While the range for the mass and cross-section of WIMPS has been narrowed down throughout the years, this has made it more difficult for the direct detection of

these particles. The NEWS-G DM detector is designed to achieve greater sensitivity than previous detectors. In the following chapter, the physics and design of the NEWS-G DM detector will be discussed in detail.

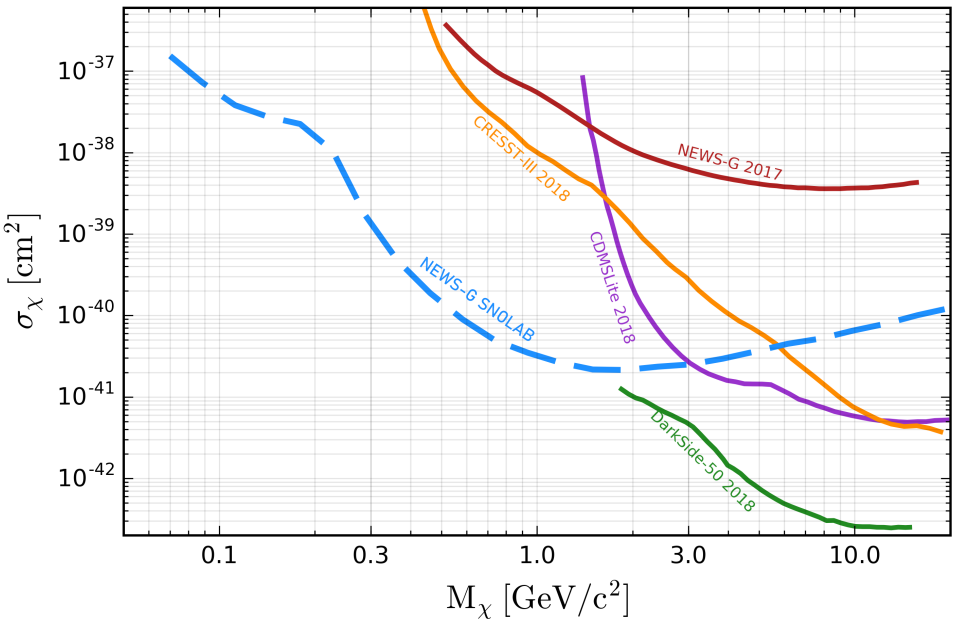

Figure 2.10: The predicted cross-section from the SNOLAB commissioning of the NEWS-G DM detector is shown in blue. Current limits were set by NEWS-G runs at the Laboratoire Souterrain de Modane (LSM), shown in red [53]. The limits of other WIMP detectors are shown as a comparison. *Plot provided by Daniel Durnford.*

Chapter 3

New Experiments With Spheres - Gas

3.1 Spherical Proportional Counters

NEWS-G is based on the concept of a Spherical Proportional Counter (SPC), with an internal volume of gas that utilizes a high-voltage central sensor. This high voltage sensor allows ionization events to be detected within the active volume. Gaseous detectors have been used in particle physics for decades, with the first notable detector being the multiwire proportional counter described by Charpak *et al.* in 1968 [54].

A proportional counter operates by amplifying an ionization event through the use of an electric field. The proportionality of such a detector means that the signal recorded by the detector is correlated to the energy of the ionization event. The magnitude of the amplification is dependent upon the voltage within the detector, which alters the overall gain.

For comparison, a Geiger-Müller counter is a type of gaseous detector that utilizes a potential difference, but will not produce a signal proportional to an ionizing event [55]. Instead, the counter produces an all-or-nothing response that is useful for recording the rate of ionizing events. Proportional counters can be used as Geiger-Müller counters if operated at a much higher voltage, but their main purpose is to provide information about the energy of the ionization event.

In this chapter, the design and physics of SPC detectors will be discussed, with

a focus on the NEWS-G DM detector.

3.1.1 The SPC Inception

The SPC was first proposed in 2008 by Ioannis Giomataris *et al.* as a solution for detecting low-energy rare events. The initial motivation behind the SPC was for the direct detection of DM particles and neutrinos, along with solar Kaluza-Klein (KK) axion decay by detecting resultant x-rays. By varying the type of gas used as the active target in the detector, neutrons in the energy range from around 0.025 eV to several MeV (thermal to fast) could also be detected. This would be particularly useful in measuring the background neutron activity in various laboratories, such as SNOLAB [51].

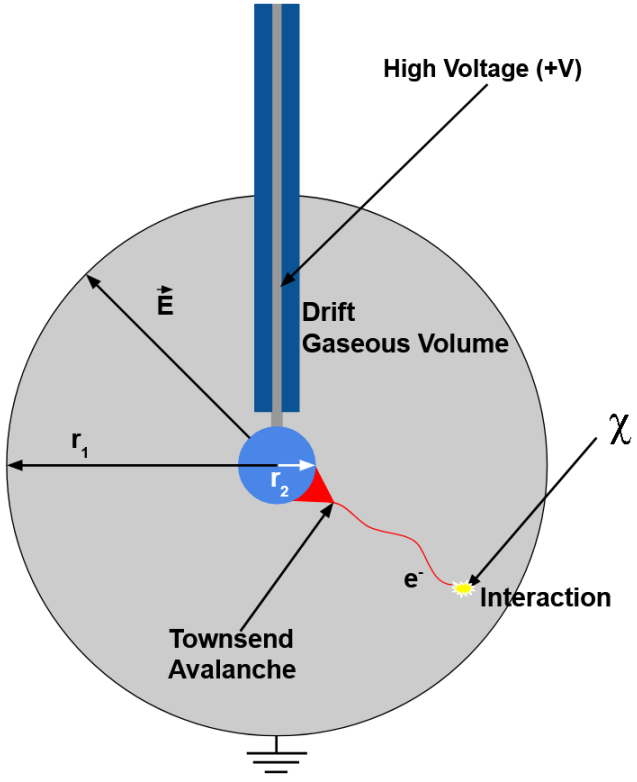

Figure 3.1: Diagram of the inner structure of the SPC . The outer spherical surface and central sensor support rod are grounded. A DM particle (χ) interacts with the internal gas. A single electron is shown drifting towards the anode, creating a Townsend avalanche when it nears. Components are not to scale [51].

For an SPC to properly operate, it requires three major components: an outer metal sphere that is grounded; an inert gas that can allow for low-energy ionization

events; and a central sensor held at a high voltage. These three components can be seen in Figure 3.1 with their appropriate labels. With this configuration, an SPC is able to detect nuclear recoils less than 1 GeV in ideal conditions. The original SPC detector first commissioned by Giomataris *et al.* consisted of a spherical copper vessel that was previously used as a radio-frequency cavity in the Large Electron-Positron Collider (LEP) [56].

A benefit of a spherical detector is that its surface-to-volume ratio is minimized. It is important to limit the surface area of the detector since many background events originate from the surface. These events include alpha decays from uranium progenitors, which can be found in detector materials [57]. By having a minimized surface-to-volume ratio, the sensitivity of the detector for low-energy rare events is increased [58]. Therefore, large-scale, high-mass spherical detectors can be designed and constructed in subterranean laboratories to detect such events.

3.1.2 Operating Principles

When a particle, potentially a WIMP, enters the volume of the detector, it has a chance of interacting with the nucleus of one of the gaseous atoms. This interaction results in an ionization event triggered by a nuclear recoil, causing the electron to be ejected from the atom. Typically, neutral particles like neutrons, photons, or proposed WIMPS will interact with a single atom to create a "point-like" event. In comparison, path events release many electrons and are produced from charged particles like muons or alpha particles.

Once these electrons are freed from their respective atoms, they are now subject to the electric field produced by the inner sensor, which is an anode. This electric field is discussed in detail in Section 3.2.2. Under the effects of the electric field, the electron will begin drifting towards the anode. The anode is the source of the electric field and is held at a voltage on the order of 1 kV. On the order of hundreds of microseconds, the electron drifts to the anode.

As the electrons come within several hundred micrometres of the anode, the large electric field gradient leads to many collisions and a subsequent exponential growth of freed electrons. This process is known as a Townsend avalanche and creates many positive ions [59]. The resulting positive ions are repelled by the high voltage and the resulting current induced on the anode is measured as a signal [60]. Depending on the arrival time of the primary electrons, the trace of the signal can

be different. These different signal shapes are indicative of the type of event that triggered the initial ionization.

Only a central sensor is required in an SPC, decreasing the complexity of the detector design. When scaling the detector to larger sizes, this configuration runs into some issues, which are discussed later in Section 3.2.3.

3.2 The Physics and Design of NEWS-G

As mentioned previously, the NEWS-G detector utilizes a gas-filled spherical volume with a central high voltage sensor to detect particle interactions. This process can be broken down into various components, beginning with the electric field produced by the anode. Within the electric field, a particle interaction occurs, and the resulting reaction depends on the gas species within the detector volume.

3.2.1 Gas Target

The gas or gas mixture within the detector is selected based on its chemical and atomic properties. The goal with gas selection is to have an appropriate detector response based on the particle interaction intended to be observed. For example, helium-3 works the best for the detection of low-energy neutrons with energies between 0.025 eV to several MeV. The average energy lost by an incident particle to create an ion pair (i.e. an electron and charged atom) is measured by the W-value in units of eV/ion pair. The W-value generally depends on the mass of an atom, in which a lower mass results in a higher W-value. The W-value is also greater than the ionization energy of a given atom [61].

Another important factor in the selection of gases involves the energy deposited through electronic and nuclear recoils. A nuclear recoil and an electronic recoil will not produce the same number of ions from interactions with the same energy. A nuclear recoil is considered "quenched" compared to the electronic recoil due to energy lost through other channels like heat, and the ratio between the ions produced for each type of interaction is known as the quenching factor. The quenching factor for a gas or gas-mixture must be well known to understand how the detector responds to low-energy particle interactions, including their respective nuclear recoils [62]. For the NEWS-G detectors, methane is used in combination with a noble gas. Noble gases are used based on their quenching factors, ionization abilities, and their general non-reactivity with most other elements.

Safety is also a concern when dealing with gases like methane, which may become explosive under certain conditions. Given the quenching factors and safety guidelines, the intended mixture for use with the NEWS-G detector in SNOLAB is a neon gas with a 10% composition of methane.

3.2.2 The Electric Field

The design of an ideal SPC is based on a hollow conducting sphere with a central charged sphere. The outer sphere is grounded, and acts as the cathode with a radius of r_1, while the central sensor is the anode with a radius of r_2. Without the support rod the electric field is spherically symmetric in this design and given an anode voltage V_0, the electric field can be calculated for all radii r between r_1 and r_2. The equation for this ideal electric field is given in Equation 3.1

$$E(r) = \frac{V_0}{r^2} \frac{1}{\frac{1}{r_1} - \frac{1}{r_2}} \tag{3.1}$$

In Figure 3.2, it is visible that this ideal electric field is not possible due to the support rod for the anode. This rod allows for a high voltage to be delivered to the anode, and a signal to be measured. This requires a more involved method to solve for the electric field since an analytical system is not possible. Instead, a numerical method can be used to solve for the electric field within the sphere based on its geometry and material properties.

These complex calculations are done using the COMSOL software. This program works through the process of finite element analysis (FEA). When simulating and solving for values in a complex electric field, FEA software divides a given surface or volume (usually provided as a Computer-Aided Design [CAD] file type) into many subsections or finite elements. Typically, boundary values are provided along with the CAD file, to give initial conditions on which the FEA can base its calculations. The FEA program then solves for each finite element piece and ends with stitching all of these elements together as a final solution. The electric field is shown in Figure 3.2.

Simulations for the detector, such as ion drift, use the calculated electric field. These simulations allow for the response of the detector to be predicted based on different initial energy inputs. Background activity can therefore be simulated as well as signals from rare-event interactions.

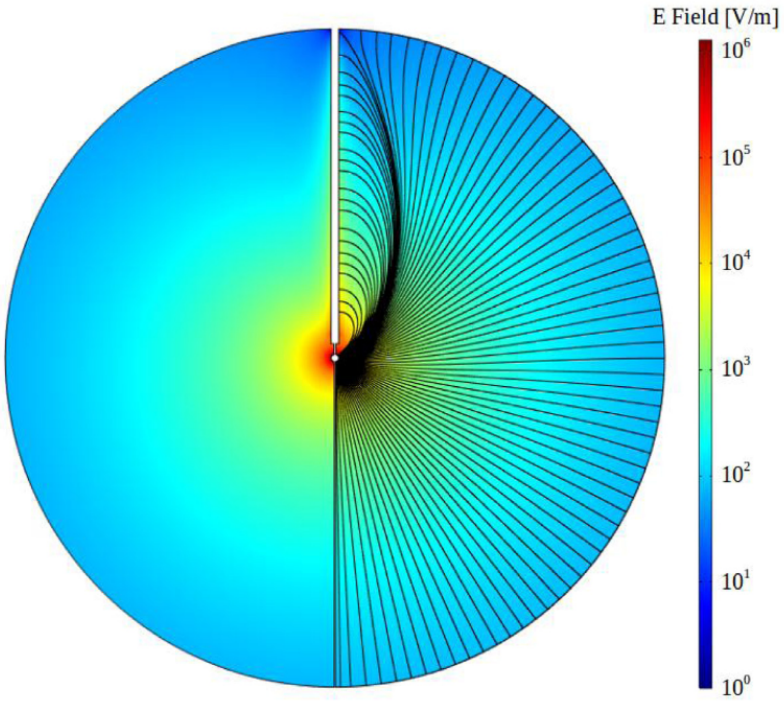

Figure 3.2: The simulated electric field of the NEWS-G SPC. The strength of the electric field is shown by the colour gradient. The black lines represent the field lines on the right part of the picture to allow the magnitude of the electric field to be properly seen. The bottom hemisphere (opposite the support rod) is approximately spherically symmetric, unlike the irregular field of the top hemisphere and close to the rod. The outer sphere and support rod are grounded [53].

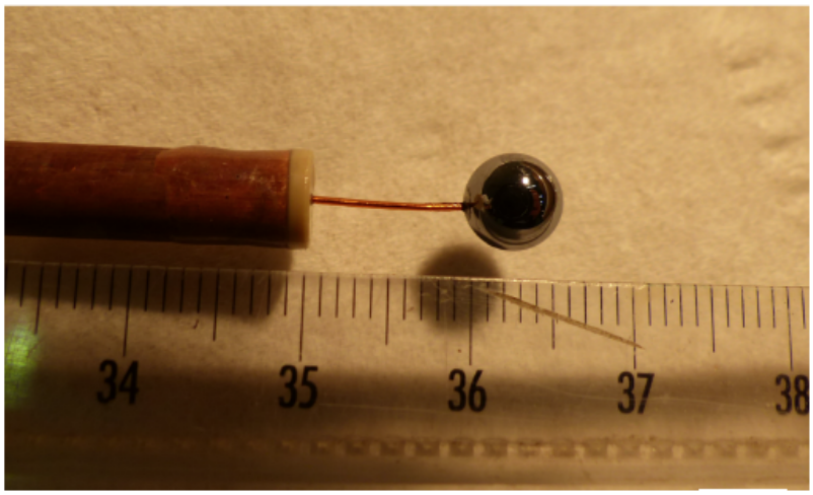

Figure 3.3: Image of the single central sensor (6.3mm Ø) for the NEWS-G detector. The sensor consists of a silcon ball bearing adhered to a copper wire. The wire then enters the support rod [63].

3.2.3 Detector Sensor

The original sensor for the SPC detector consisted of a ball bearing adhered to a copper wire, as shown in Figure 3.3. Since a single sensor can be used to detect events in the full detector volume, the complexity of the entire system is minimized compared to the many hundreds of channels used in detectors like DEAP-3600 [64]. A silicon ball bearing is used since it is electrically conductive, spherical, and easy to procure.

Within the detector, the voltage can be changed to alter its gain, which is also referred to as signal amplification. An increased electric field gradient is produced with a higher voltage, which increases the gain of the detector. The higher gain allows for ion mobility to increase, meaning that ions leave the central sensor faster to produce an amplified signal. This aids in reducing the effects that other contaminants within the gas may have on the system, commonly referred to as attachments [65]. More information on this can be found in Section 3.4.1. As the scale of an SPC increases, the voltage on the single anode must increase to account for the $1/r^2$ behaviour of the electric field. An increased voltage can cause unwanted sparks within the volume of the detector. The use of multiple anodes can decrease the voltage applied to each anode, which eliminates unwanted effects.

3.2.4 The Achinos Sensor

While a small, central anode decreases the complexity of the NEWS-G detector, it restricts the ability to create a larger scale detector. For larger detectors like the 140 cm diameter device being installed at SNOLAB, the electric field close to the inner surface is very weak, even with an anode voltage of 10 kV [66]. This weak field results in higher drift times, leading to poor electron collection efficiency. The detector stability also breaks down at high voltages and, as mentioned earlier, such voltages can create sparks within the detector [67].

To solve this issue, a central sensor with multiple balls has been constructed; this is referred to as the "achinos" sensor. The term achinos is Greek for sea urchin, which the sensor resembles in Figure 3.4. The achinos design consists of eleven anodes equidistant from one another and at the same radius from the centre of the detector. Each anode is a ball bearing that has a diameter on the order of one millimetre that has been adhered to an insulated copper wire. The central hub is made from a highly resistive epoxy so there is minimal interference with the electric

field [66].

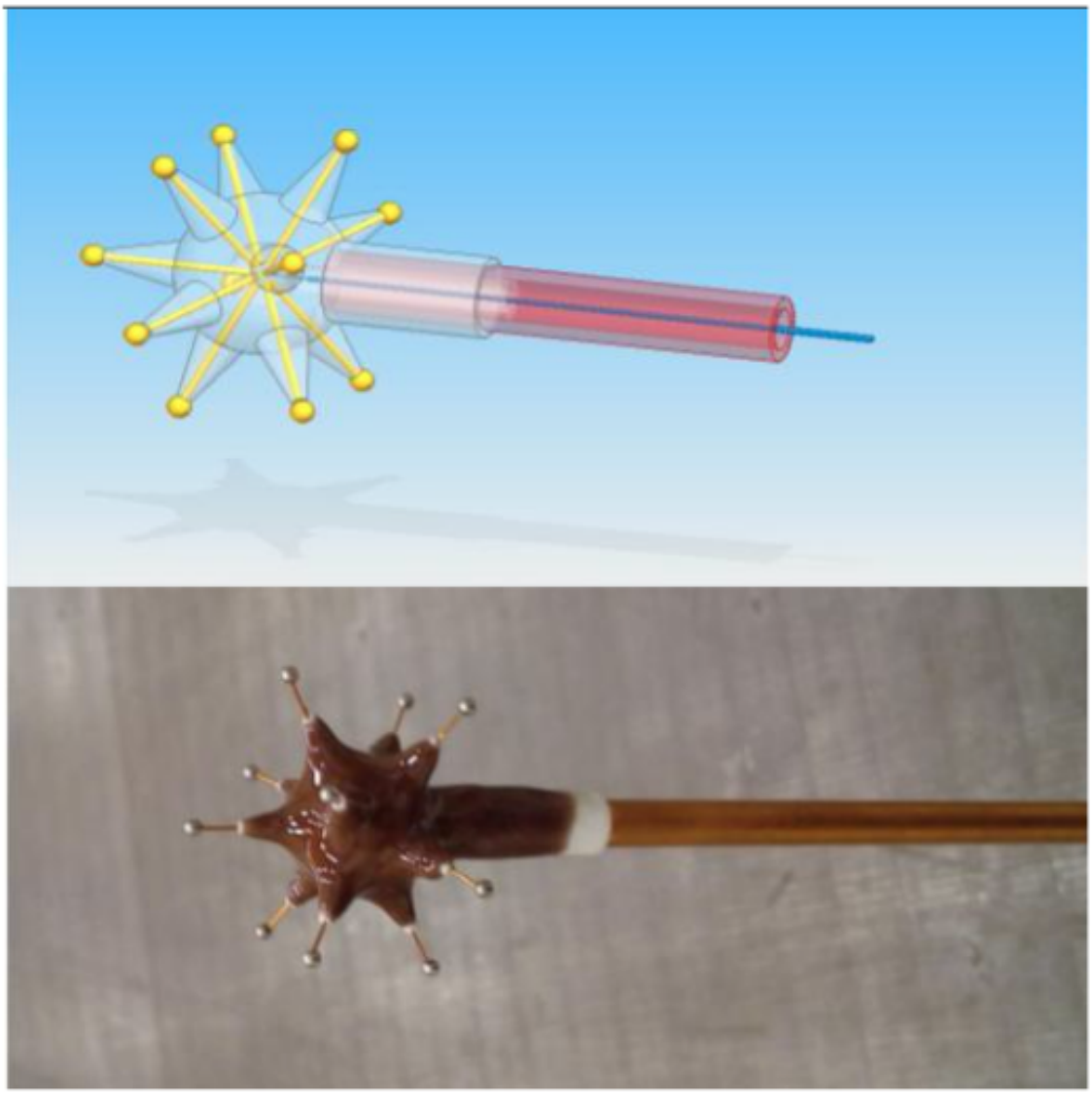

Figure 3.4: Top: A three-dimensional diagram of the achinos sensor, including internal wire connections. Bottom: An image of an achinos probe being used in the NEWS-G detector. The end balls on each protrusion provide the voltage for the detector and measure the signal of an event [65].

The use of multiple anodes allows for a higher electric field near the inner surface as compared to the single anode, while the voltage for each anode is comparatively smaller. The overall shape of the electric field is no greatly altered when compared to Figure 3.2 (except when close to the achinos) aside from an increase in the gradient. Therefore a high gain is possible, reducing the ion drift time while the electron collection efficiency increases. An additional benefit of the achinos is the possibility

that the location of an event in the volume of the detector could be found based on which anode a signal is measured from. Due to the increased complexity involved with monitoring eleven separate channels from the detector, the current solution is to group the anodes into two channels. The first channel consists of the five balls closest to the support rod ("North" channel), while the second channel groups together the remaining six balls ("South" channel).

By having two separate channels, the region of the spherical volume in which an event occurs can be estimated based on simulations of ion drift in the electric field. These simulations are outside the scope of this writing, but work is being done by various members of the NEWS-G collaboration on simulations for both ion drift and detector response to particle interactions.

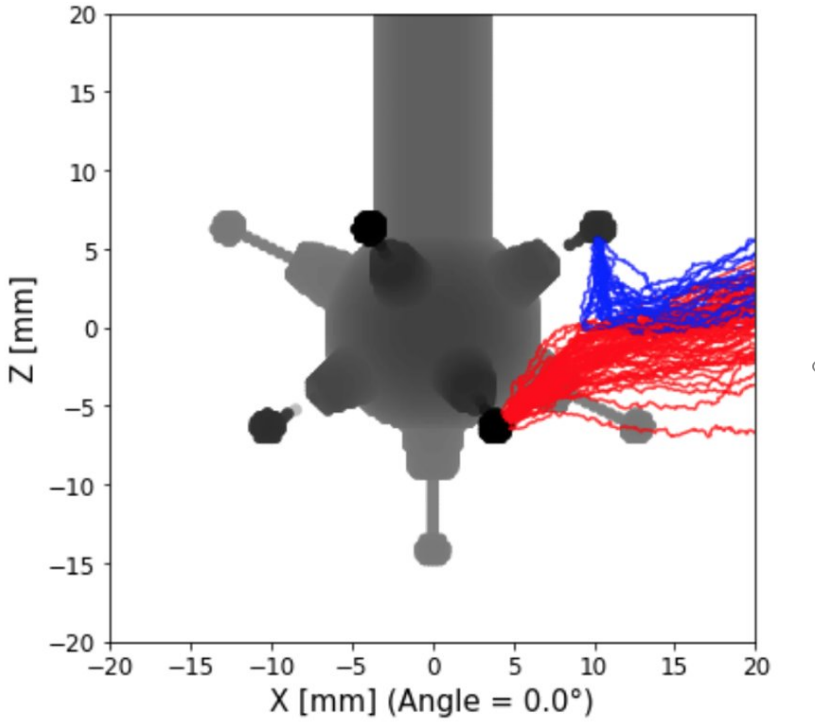

Figure 3.5: A simulation showing the paths that single electrons follow within the achinos detector. In this example, electrons from the same event are arriving at two different anodes, creating a shared event. Red lines are for the South channel and blue lines are for the North Channel. *Image credit to Carter Garrah.*

While having two different channels provides more information about the initial event, some information becomes more complex to decipher. The changes in the electric field by ions can be detected by multiple probes of the achinos, which may be recorded in separate channels. A shared event occurs when multiple electrons

from an event arrive concurrently at different probes in separate channels. Another phenomenon is the cross-talk, which occurs when the changing electric field caused by secondary ions around an anode in one channel also affects an anode (or anodes) in the other channel. Shared events and cross-talk will be discussed further in Chapter 4, but an example of a simulated shared event is shown in Figure 3.5.

3.2.5 Particle Interactions

The process that leads to a signal in the SPC begins with a particle interaction in the gaseous medium. There are several ways in which a particle may interact with the gas, which are listed below.

1. Charged particle interactions occur primarily with alpha particles, electrons, or muons. There are several ways in which the particle will interact with the gas.

    - An incoming charged particle will transfer energy to an atom, leading to the excitation of the atom. If the energy within this excited atom collides with a molecule in the gas with a lower ionization energy than for the atom, it will ionize the molecule. This is known as the Penning effect [68].

    - Bremsstrahlung radiation is produced in the form of a gamma or X-ray photon when a charged particle undergoes rapid acceleration during a collision [69].

    - Particles can scatter directly off of the nucleus, resulting in a nuclear recoil. Energy is absorbed by the nucleus and then transferred to an orbital electron, which becomes ionized. The resulting free electron is called an Auger electron. An Auger electron is not always produced, and the recoiling nucleus may just electronically interact with other atoms [70].

    - Ionization can also occur when the incoming particle interacts with the electronic cloud around an atom. The transfer of momentum to the electron can have enough energy to eject it from its orbital [71].

2. Photons can also create ionization events in the detector, interacting through three main mechanisms; the photoelectric effect, the Compton effect, and pair

production.

- First described by Einstein for metals, a photon can eject an electron from its atom. For this (the photoelectric effect) to occur, the photon must have an energy equal to or greater than the ionization energy of the electron orbital [72].

- Instead of being absorbed by the atom, the Compton effect occurs when a photon scatters off an electron directly, transferring its momentum and freeing the electron from the atom [69].

- The spontaneous creation of an electron-positron pair can occur when a photon with an energy of at least 1.2 MeV interacts with an atom in the detector. If no other forces are present, the pair will recombine due to their electric attraction and annihilate. In the electric field of an SPC, the pair may instead be pulled apart, with the electron drifting to the anode [71].

3. Neutral particle reactions occur through interactions between the incoming particle and the nucleus of an atom in the gas. These interactions can occur through either the strong nuclear force or the weak nuclear force; a WIMP is proposed to interact through the weak force.

As discussed previously in Section 3.1.2, once the electrons are freed, they begin drifting towards the anode at the centre of the detector. These resulting electrons are also subject to the charges particle interactions discussed.

3.2.6 Detector Signal and Calibration

In the volume of the detector, the electric field is based on the $1/r^2$ relation. As the electron nears the anode (a few hundred μm), it gains enough kinetic energy to begin ionizing other atoms within the gas creating a Townsend avalanche. Depending on the energy of the initial particle interaction, there can be one or more initial (primary) electrons. The number of electrons released directly influences the magnitude of the Townsend avalanche. The presence of more ions near the anode produces a larger change in the electric field.

As the secondary ions drift away from the anode, a signal is produced by the current induced on the anode. The wires connected to the spherical sensors in the achinos carry an analog signal ($\sim$ 1 mV) through the support rod to a connected amplifier. This amplifier both outputs a high voltage (provided by a high voltage power supply) to the anode and accepts the signal from the detector. The amplified signal then goes to an analog-to-digital converter in a Data Acquisition (DAQ) system, where the signal can be recorded and saved on a computer. Further discussion of the signal output and processing will be provided in Chapter 4.

Also discussed in more detail in the following chapter is the calibration of the detector. The output signal from the SPC is converted into a digital format that uses Arbitrary Digital Units (ADUs). This output must then be calibrated using well-known interaction energies from various radioactive sources. The NEWS-G collaboration favours argon-37 (^{37}Ar) as a radioactive calibration source. Through the electron capture process, ^{37}Ar has a distinct low-energy and high-energy decay mode with energies at 270 eV and 2.8 keV, respectively [73]. The NEWS-G collaboration can also use the two different energies during calibration runs to check that the response of the detector (and the measured signal) scales linearly with the energy of ionization events (i.e. checking the linearity of the detector). Other radioactive sources, like iron-55 (^{55}Fe) and americium-beryllium (AmBe) are also used with the detector as external calibration sources.

In addition, a pulsed ultraviolet (UV) laser ($\lambda = 213$ nm) is used for calibration and to monitor the stability of the detector. This UV laser travels through fibre optic cables, which are split into two different ends. The first end terminates at a photodetector that flags pulses and records their relative amplitude to provide information about power fluctuations. The other fibre optic cable enters the volume of the detector, where it is then directed onto the inner surface of the sphere. When the laser is on, it interacts with the detector material, which undergoes the photoelectric effect. The released photoelectrons act as a timing device for the ion drift time from the inner surface of the detector to the production of a signal [53].

3.3 Construction of NEWS-G

The NEWS-G detector was first commissioned at the Laboratoire Souterrain de Modane (LSM) facility in France, which is a low-background laboratory constructed underneath a mountain. At the time of writing, the newest generation 140 cm diam-

eter NEWS-G detector has been transferred from France to SNOLAB in Sudbury, Canada. This facility is over two kilometres underground and is a class-2000 clean-room, leading to very low levels of background radiation from dust. However, the facility is surrounded by rock, leading to high levels of radon in the environment. The combination of shielding from cosmic rays, and the low level of particulates in the facility result in an ideal location when searching for rare events.

3.3.1 Detector Materials

NEWS-G is predicted to be sensitive to DM particles with masses below 1 GeV and a cross-section below 10^{-41} cm^2, so must have optimal conditions to make these measurements. To mitigate the background events that may occur, radiopure materials must be used for the construction of the detector. For the hollow metallic sphere (that contains the gas) with a diameter of 1.40 m, C10100 (99.99%) copper was used [74]. Copper is both readily available and has no long-lived isotopes [75]. However, radioactive impurities such as uranium progenitors and cosmogenically activated copper can be found in the copper materials used.

To aid in the mitigation of unwanted background events like radioactive decay, the sphere is first well cleaned, electropolished, and then electroplated with copper. Commercial detergents are used to clean the inner surface of the sphere, followed by sanding to ensure the surface is smooth. The surface is then etched with an acidic solution that removes a thin layer of copper and contaminants, while also protecting the exposed copper from oxidation [76]. Before electroplating, the inner surface is electropolished, which removes copper from the sphere into an electrolytic solution. During this electropolishing process, an average of 24.7 μm of material was removed.

The inner surface of the sphere then acts as the cathode in the electroplating process, while another piece of copper acts as the anode. The reduced copper from the electrolytic solution is deposited on the surface. Contaminants present in the electrolytic solution may adhere to the surface during this process. The electroplated layer has very low activity on both upper and lower hemispheres, measured to be < 0.58 μBq/kg and < 0.26 μBq/kg, respectively for thorium-232 (^{232}Th) contamination, and < 0.24 μBq/kg and < 0.11 μBq/kg, respectively for uranium-238 (^{238}U) (measured at a 68% upper confidence limit) [74].

The gas itself must also be made pure through both the initial processing of the gas from the supplier and when it is prepared to enter the spherical detector. Due to

the presence of uranium in most materials, radioactive materials will be present in all of the surfaces with which the gas may be in contact. These include the bottles storing the gas, as well as the tubing and instruments used in the Gas Handling System.

Work is ongoing to investigate different materials for future SPC spheres, along with new methods to create a sphere using electroforming techniques. Along with the current installation of the NEWS-G detector in SNOLAB, other spheres exist for research and development purposes. These spheres, which vary in material composition, are not designed for rare event searches, but instead for testing technologies that may be applied to the SNOLAB detector. An image of the test sphere installed in the Piro Lab at the University of Alberta is shown in Figure 3.6.

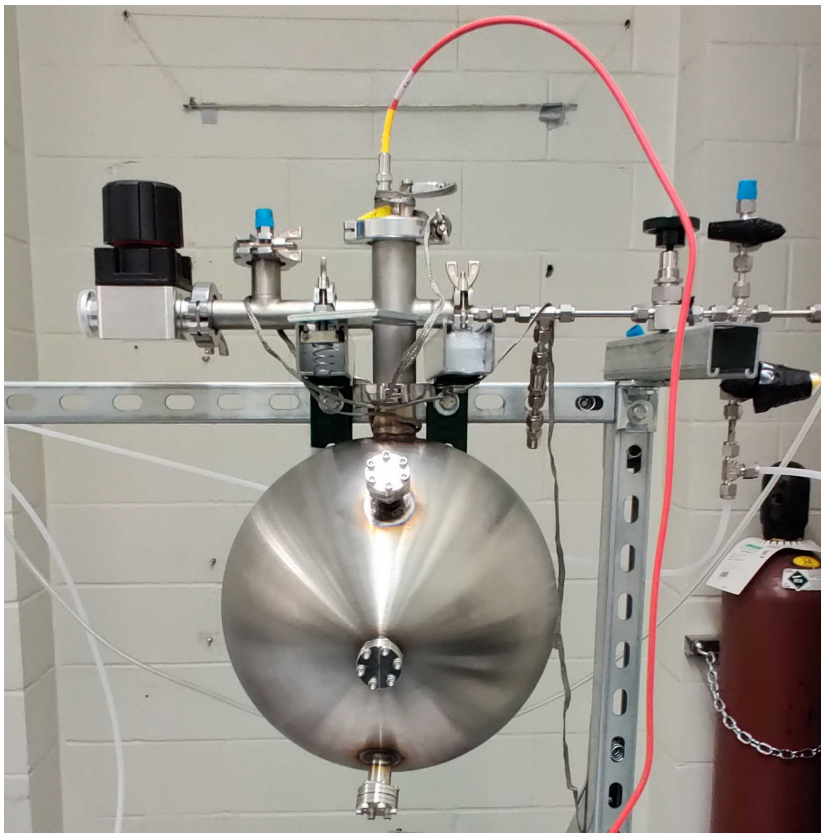

Figure 3.6: An image of the current sphere in the Piro Lab. This sphere has a diameter of 30 cm, and is configured for testing with the radon trapping system, along with future tests. The neck protruding from the sphere is connected to several gas handling components. The neck is also connected to the red cable, which both provides the high voltage and carries events signals.

3.4 Gas Handling, Shielding, and Electronics

3.4.1 Gas Handling System

The Gas Handling System (GHS) of the NEWS-G detector has multiple functions. It must create a high vacuum within, transfer gases to, and purify gases for, the detector. As shown in Figure 3.7, the GHS is a multi-component system that is broken down into six main sections, each with a specific function.

In the green section are four connected gas cylinders, each containing a different gas. As discussed previously, the gases being used have been selected based on their properties and the safety regulations of the SNOLAB facility. To avoid bringing pure methane into the facility, the methane-noble gas mixtures are premixed at the facility of the supplier before being transferred to the site of the experiment. The final gas will be a neon-methane mixture, but other gases like nitrogen, argon, and argon-methane are used for testing. When the detector is not in use, it is filled above atmospheric pressure with a non-reactive gas like argon to ensure that outside air will not enter the detector and to suppress outgassing within the detector.

The red section in the top-middle of the diagram is for gas purification. Gas coming from the bottles enters this section, and a pump circulates gas through the components of this section. While the details of the radon purification will be discussed further in Chapter 5, there are three main components to this system: the circulation pump; the gas purifier (Getter); and the radon trap. The circulation pump is in place to run a volume of gas through the other two components multiple times (at 1 L/min). The Getter removes unwanted gases such as oxygen and electronegative ion impurities like water vapour. The reasoning behind the removal of these two gases specifically, as well as the removal of radon gas by the radon trap, will be discussed in Chapter 5.

The yellow section is where the vacuum cart and Residual Gas Analyzer (RGA) are found. The turbo vacuum pump can be used on the entire system, including the sphere (i.e. detector). By creating a high vacuum environment in the GHS, gases like water vapour that may have adhered to inner surfaces can be gradually removed from the system. The quantity of impurities being removed from the system is checked using the RGA. The RGA is a mass spectrometer that operates at low pressures (1×10^{-7} Bar) and provides information about the relative concentrations of different gases [77]. Since the RGA operates only at low pressures, it cannot monitor gases when the detector is filled.

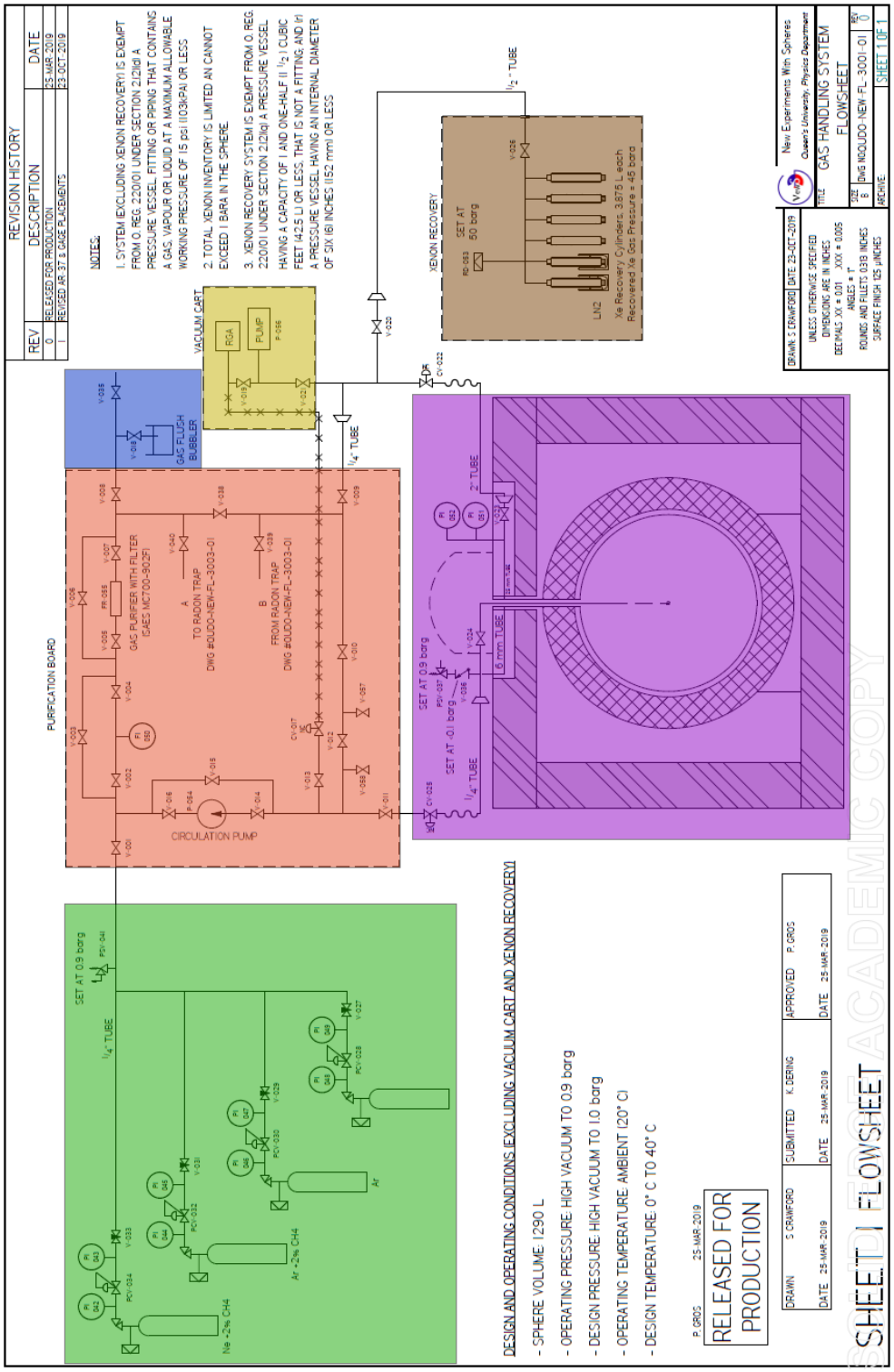

Figure 3.7: A diagram of the Gas Handling System designed and implemented for the NEWS-G SNOLAB commissioning. The coloured boxes indicate the gas supply (green), gas purification (red), vacuum and RGA (yellow), exhaust (blue), detector (purple), and xenon recovery system (brown). These sections are discussed in detail in the text. *Image supplied by Sean Crawford.*

Adjacent to the yellow vacuum system is the exhaust system for the GHS which is highlighted in blue. This is the location where gases can be exhausted in accordance with standard SNOLAB procedures.

Connected to the bulk of the GHS is the detector itself, highlighted in purple. A series of valves and pressure gauges allows a controlled injection of gas into the sphere from the circulation and purification system. In the diagram, it is noted that the detector is surrounded by a thick box, with an access point at the top of the sphere designed for gas input/output and electronics. This box is the shielding for the detector that protects against external backgrounds.

3.4.2 Shielding and Electronics

The shielding of the NEWS-G detector combines several different materials in layers to mitigate external backgrounds. The two main layers of this shield are lead and high-density polyethylene (HDPE). The spherical lead shield consists of 22-cm, low-activity, commercially available lead with an additional 3-cm thick inner surface of archaeological Roman lead. The Roman lead is sourced from ancient shipwrecks and has virtually no radioactivity (less than a few mBq/kg) from lead-210 (^{210}Pb) and was shielded from cosmic ray activation by the overburden of water [78]. As shown in Figure 3.8, the lead layer surrounds the copper sphere. The lead is surrounded by a stainless steel container that can have a nitrogen cover gas continuously flowing through.

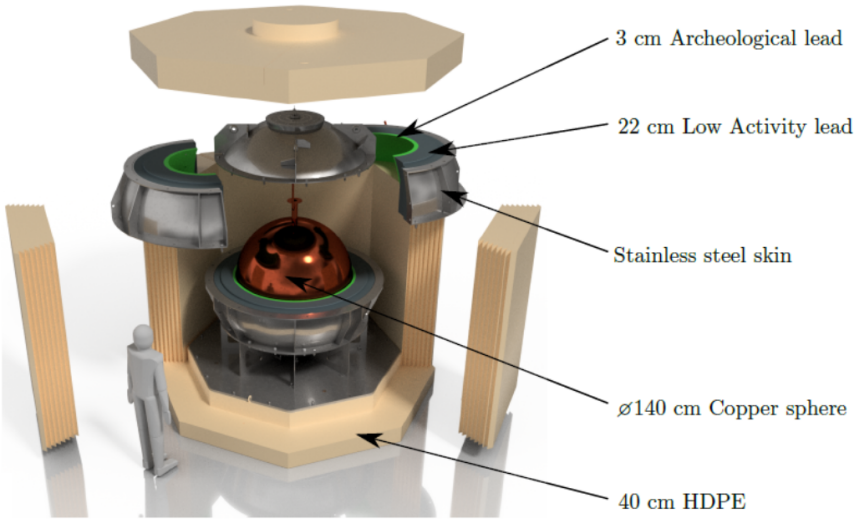

Figure 3.8: A cross-section of the different layers of the shielding for NEWS-G. From the outside in, the layers are HDPE, stainless steel, and archaeological lead [2].

The HDPE shield forms an hexagonal neutron shield around the lead and I was involved with its manufacturing and assembly at the University of Alberta. The shield is 40-cm thick and was constructed using 5-cm thick HDPE sheets that were machined and placed in a staggered arrangement. This design ensures that the minimum depth of the HDPE shield is 20 cm [79].

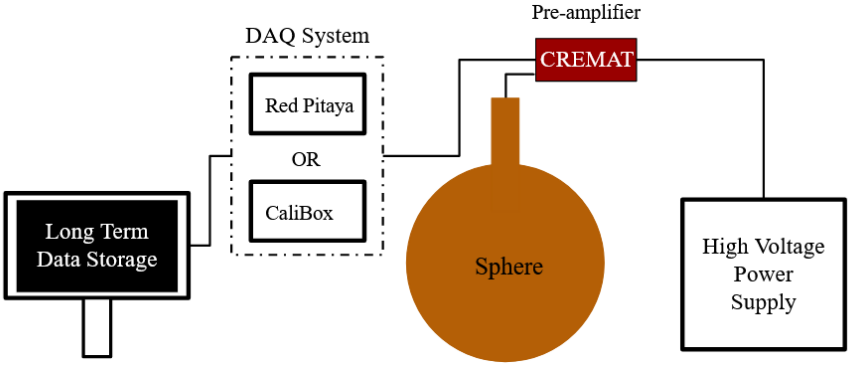

Figure 3.9: A diagram of the data acquisition system used with any NEWS-G SPC. Both the Red Pitaya and the Calibox are DAQ systems produced by different companies, but the Calibox is no longer manufactured. At the UofA, the Red Pitaya is used.

Data acquisition for the NEWS-G detector occurs using multiple electronic components shown in Figure 3.9. The high voltage supply is run to the CREMAT CR-110 pre-amplifier, which is connected to the anode of the sphere. Within the same high voltage connection between the sphere and the CREMAT, an event signal is transferred from the anode to the CREMAT. The signal is then amplified by a ratio of 1.4 V/pC and sent to the DAQ system. Multiple DAQ systems are in use with various NEWS-G prototypes, but they all run the SAMBA program. SAMBA, a program designed specifically for particle detector DAQ systems, provides initial data processing, filters, and triggers, and will be discussed more in Chapter 4.

While the design of the detector and its installation location take into account the mitigation of any background sources, methods to further decrease background activity are being investigated. The removal of radioactive gases from the gaseous active target is one such method in development and will be discussed in great detail in Chapter 5. Before this discussion, Chapter 4 will focus on the signals produced from the detector during its run at the LSM. Data processing techniques are in development, with a focus on accurately reconstructing event energies from the detector signals. Several optimizations can be made for processing parameters to ensure the information obtained from the trace of a signal is accurate.

Chapter 4

Optimizing Processing Parameters

4.1 Data Processing

Within the NEWS-G detector, the central sensor produces the high voltage required for Townsend avalanches, along with recording the current induced by the secondary ions drifting away from the anode. Changes in the electric field are sent as a current through several components and arrive at the Digital Acquisition (DAQ) system, where the signal is digitized. Once digitized, some preliminary processing is done. Several important steps in this process will be described in detail in this chapter including the storage and access of the data. The processing of data involves many complexities, such as creating cuts that improve the quality of the data. To ensure that the data being analyzed is processed consistently among the NEWS-G collaborators, standardizing and optimizing the initial data processing is imperative.

4.1.1 Data Recording

When an event occurs in the detector, the signal produced is analog. The signal is composed of small current changes and must be amplified. To minimize the amount of noise included in the signal during amplification, high-quality components with low intrinsic noise or interference must be used both in the detector and the amplifier. The wires within the support rod are shielded to prevent any interference that may alter a signal. The CREMAT CR-110 (CREMAT, Inc) amplifier adopted by the collaboration was specially constructed to minimize the noise introduced into the signal.

Once the signal has been amplified from the CREMAT, it is then sent to the DAQ system to be digitized. The DAQ system contains a chain of components in which the signal undergoes preliminary processing. Due to the various channels of the detector, the DAQ is equipped to accept up to three channels. As mentioned in Chapter 3, these channels are for the photodetector used for the UV laser, and either one channel for the single ball sensor, or two channels for the achinos sensor.

The conversion of the signal occurs in one of two DAQ systems: a CaliBox or a Red Pitaya. The CaliBox is a DAQ that is no longer produced [80], and so is being replaced with the Red Pitaya. The Red Pitaya contains open-source firmware and software, allowing for easier customization [81]. Either can be connected to the controlling computer and run the SAMBA program, which is responsible for the preliminary signal analysis.

4.1.2 SAMBA

SAMBA, initially designed for the EDELWEISS experiment (a dark matter detector that uses High-Purity Germanium bolometers at mK temperatures), operates on the DAQ system and the controlling computer [82]. SAMBA is a general-purpose firmware and software that uses a combination of FPGA (Field-Programmable Gate Array) and a GUI to record, process, and store data.

During data acquisition, filters can be applied to the incoming data, and further processing is done with a trigger. Triggers are used to identify signals within the continuous flow of data and save them as events. When a signal is processed by SAMBA, it centred in a 8000 μs window (at 4000 μs). Since the sampling rate is at 0.96 μs/sample, the window can be converted to one with a length of 8333 samples. This data is saved as a SAMBA file, which is then converted to a ROOT file and stored within the controlling computer [83]. The long-term storage for NEWS-G is on a server at Queen's University.

4.2 Detector Energy Response Calibration

Different methods can be used to calibrate an SPC. The desired outcome is to quantify the detector energy response for any given event. By using different radioactive sources with known decay energies, the response of the detector can be mapped, which includes checking the linearity of the detector. Argon-37 (^{37}Ar) is one such source that can be used for this calibration.

4.2.1 Argon-37 Calibration

There are several benefits to using ^{37}Ar in a gaseous detector, one of which is that the source is itself gaseous. When injected into a NEWS-G detector, the ^{37}Ar gas can diffuse homogeneously into the volume of the detector, creating events throughout the active volume of the detector. In comparison, solid sources are used on the outer surface of the detector, but most of the signals produced will originate near the inner surface.

Another benefit of ^{37}Ar is that it produces both low-energy (270 eV) and high-energy (2.8 keV) decays. These occur through the electron capture process, from either the L-shell electrons or the K-shell electrons, respectively. During the process of electron capture, an electron has a probability of being within a nucleon in the atom. When the electron is absorbed by this nucleon (i.e. a proton), the interaction produces a neutrino and a neutron, shown below as

$$p + e^{-} \rightarrow n + \nu_e.$$

The absorption of an electron into a nucleon creates a vacancy in its orbital. An electron in a higher orbital then fills the spot, releasing an X-ray, or producing an Auger electron. Since this reaction can occur at both the K-shell and L-shell of the argon atom, two distinct energies can be expected from the decays. These energies have been measured [84] [85] and an example of the energy distribution is shown in Figure 4.1.

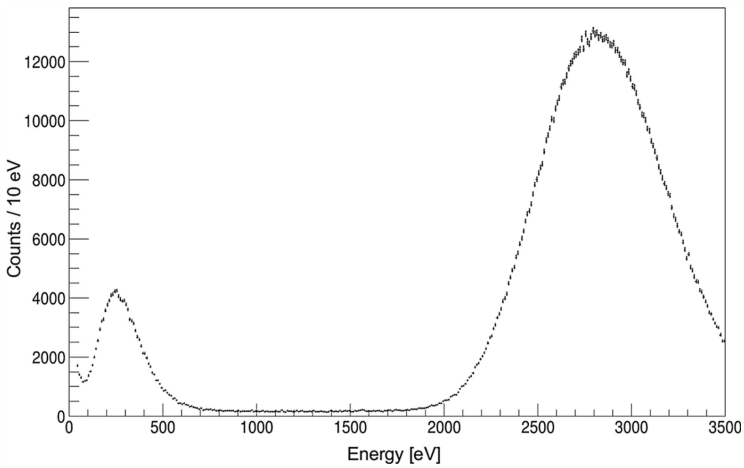

Figure 4.1: The energy distribution from the 270 eV and 2.8 keV decays of the ^{37}Ar isotope. These data were measured in an SPC at Queen's University [73]

.

When distributed throughout the detector volume, ^{37}Ar decays can be measured and recorded by the DAQ and storage systems. Details about the run parameters and conditions are also included, such as the gas pressure, anode voltage, and run time. The data that will be discussed in this thesis comes from a four-hour detector run (labelled "tj13s000") completed in the Laboratoire Souterrain de Modane (LSM) facility using pure methane. The gas was held at a pressure of 0.135 mBar and the anode voltage was 2030 V for the extent of the run in the 140 cm diameter sphere.

4.2.2 Use of Different Sources

Other sources can be used for detector calibration, such as iron-55 (^{55}Fe), which creates different X-ray energies around 6 keV [86]. Since ^{55}Fe is solid, it must be placed against the exterior of the detector. This has proven to be a challenge due to the shielding around the detector. To overcome this issue, two components were included in the NEWS-G detector at SNOLAB.

The first is a helical tube placed from the outside of the lead shielding to the outer surface of the sphere. When construction is completed, this will allow an external solid source to be placed against the sphere. The helical shape of the tube prevents background neutrons from reaching the detector.

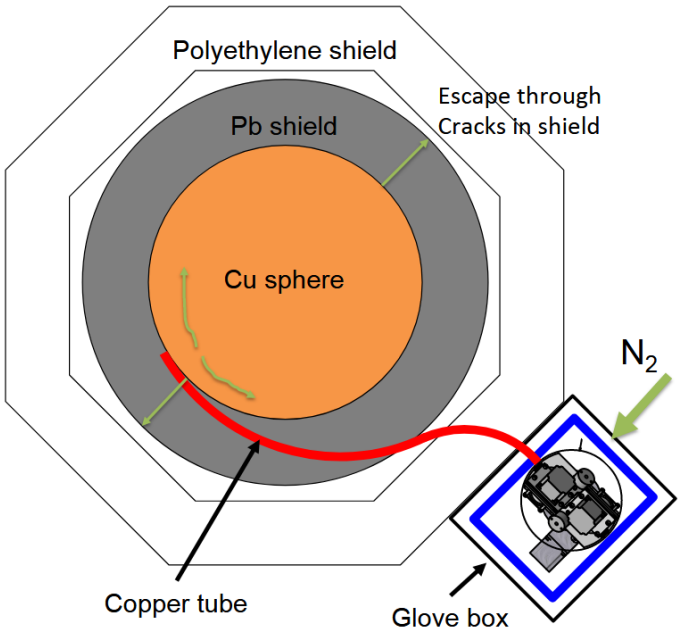

Figure 4.2: A diagram of the motor and tubing to deposit and remove radioactive sources from the outer surface of the detector. *Image credit to Pierre Gorel.*

The second component is a motor system that deposits and removes the source in the helical tube. I was responsible for machining several parts of this motor at the UofA, which are being assembled and tested at SNOLAB.

4.2.3 Signal Production

It is important to highlight how the signal being processed is produced in the first place. While this process was briefly discussed in Chapter 3, the exact mechanics that describe the two peaks shown in Figure 4.1 were not discussed.

To begin, when Ar^{37} undergoes a K-shell electron capture, both X-rays and Auger electrons can be produced. Multiple electrons can be produced from one interaction, but the energy is deposited locally. Energy can also escape through X-ray production, in which the photons escape the detector without interaction. Using an ideal example where only one 2.8 keV electron is produced, the first thing to happen is the production of primary electrons. The W-value, which was mentioned previously in Chapter 3, dictates the average energy required to create an electron-ion pair in the detector. This is highly dependent on the gas species, ionizing particle type, and the initial energy. When comparing the W-value to the energy of the particle (2.8 keV in this example), Equation 4.1 can be used to find the mean number of electron-ion pairs created.

$$\mu = \frac{E}{W(E)} \tag{4.1}$$

The value of μ is just the mean, while the actual number of electron-ion pairs produced is subject to statistical fluctuations. The fluctuations for a given number of primary electron-ion pairs produced, N, are characterized by σ_N, which yields the Fano factor:

$$F = \frac{\sigma_N^2}{\mu}. \tag{4.2}$$

This is approximately Gaussian for the 2.8 keV event and contributes to the spread of the 2.8 keV peak shown in Figure 4.1. For this distribution of primary ionization, the Fano factor is expected to be approximately 0.2. Events that produce a single primary electron are also subject to statistical fluctuations described by the Fano factor, but are not the area of focus for this thesis [63].

Once the electrons have been freed, they begin to drift towards the centre of the detector due to the high voltage applied to the anode. Within several hundred micrometres of the anode (or anodes, in the case of the achinos), the electric field intensity is around 10^5 V/cm, which triggers a Townsend avalanche. The large number of secondary ions produced follows a Gaussian based on the Central Limit Theorem [87], contributing to the spread of the 2.8 keV peak shown in Figure 4.1. The newly created positive ions from the Townsend avalanche are then repelled by the anode, and their movement away induces a current on the anode. This induced current is integrated by a charge sensitive pre-amplifier and then processed by the DAQ system.

4.3 Optimizing QUADIS Parameters

4.3.1 The QUADIS Data Processing Program

The QUADIS software is designed for the efficient calculation of event properties based on user-input parameters [80]. These parameters include well-known detector properties, such as gas pressure and voltage. Other parameters that are used in QUADIS are less objective and differ for varying experimental setups.

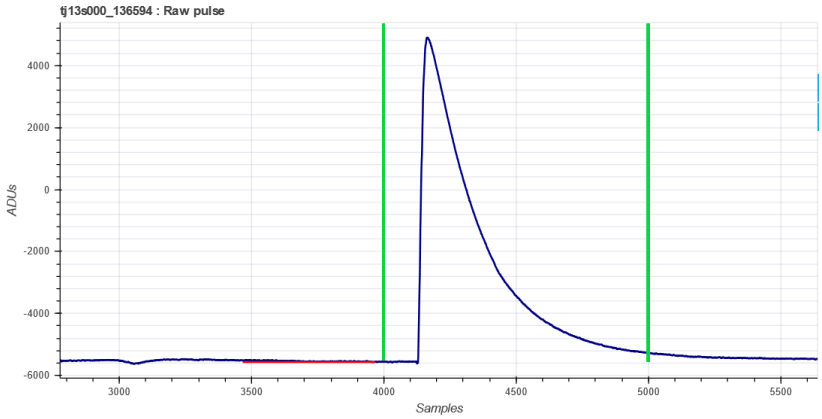

Figure 4.3: A raw pulse from the NEWS-G detector. The red line indicates the placement of the baseline window. The two green lines indicate an integration window size in which a pulse is considered. Here, the integration window has a width of 1100 samples. The left green vertical line is located at the start sample location. 1 sample = 0.96 μs.

A run can be processed by QUADIS based on information from a ROOT file. This file contains the raw pulses, along with the trigger information. An example

of a raw pulse is shown in Figure 4.3. The average baseline is then calculated based on an eight-sample width window, and the signal is adjusted for a baseline at zero Analog-to-Digital Units (ADU).

Several processes occur to improve the quality of the signal. First, a trapezoidal filter is applied to the signal, which helps find the start of the pulse (Figure 4.4(a)). Once the proper starting point is located, the baseline is then removed from the signal, and is found from averaging a window of samples prior to the start of the signal (Figure 4.4(b)). The signal is then deconvolved in order to remove distortion caused by the pre-amplifier response (Figure 4.4(c)). This removes the exponential tail that is produced by the rise time of the electronics. The pulse must then be deconvolved again using the reverse Fourier transform process to remove the effects of the induced current in the signal. Before this can happen, the signal is smeared to remove any non-continuous (spiky) segments of the pulse, ensuring it is smooth. Once the smoothing algorithm has been applied, the pulse can be deconvolved again, producing the original event pulse shape (Figure 4.4(d)).

The newly processed pulse can then be analyzed for its amplitude, and integrated within a specified window (Figure 4.4(e)). The width of this window is selected to include the signal from all primary electrons while not being too wide so as to include extra noise. This integration curve can then be used for calculations of the rise time. The latter is the time from the beginning of the integrated curve to the end. The values selected by the NEWS-G collaboration are at 10% and 90% of the total amplitude of the pulse. Other variables are measured for both the raw signal and the doubly deconvolved pulse. A value relevant to the work in this thesis is the amplitude of the pulse, which is proportional to the energy of the event recorded and is measured in ADU.

Each channel of the detector undergoes this process and the result is saved in a ROOT file. Two QUADIS parameters that have a significant impact on the result of data processing are the start sample and the aforementioned integration window width. The latter is the window in which a pulse is considered, while the former marks the starting point for the integration window. These are shown in Figure 4.3. A sample is related to the recording frequency of the system and 1 sample = 0.96 μs. The start sample location is also the basis for the baseline window. The effect of varying these two parameters are shown in Figure 4.5. The only difference between the two plots is the size of the integration window (a width of 400 samples compared to 900 samples), which is user-specified.

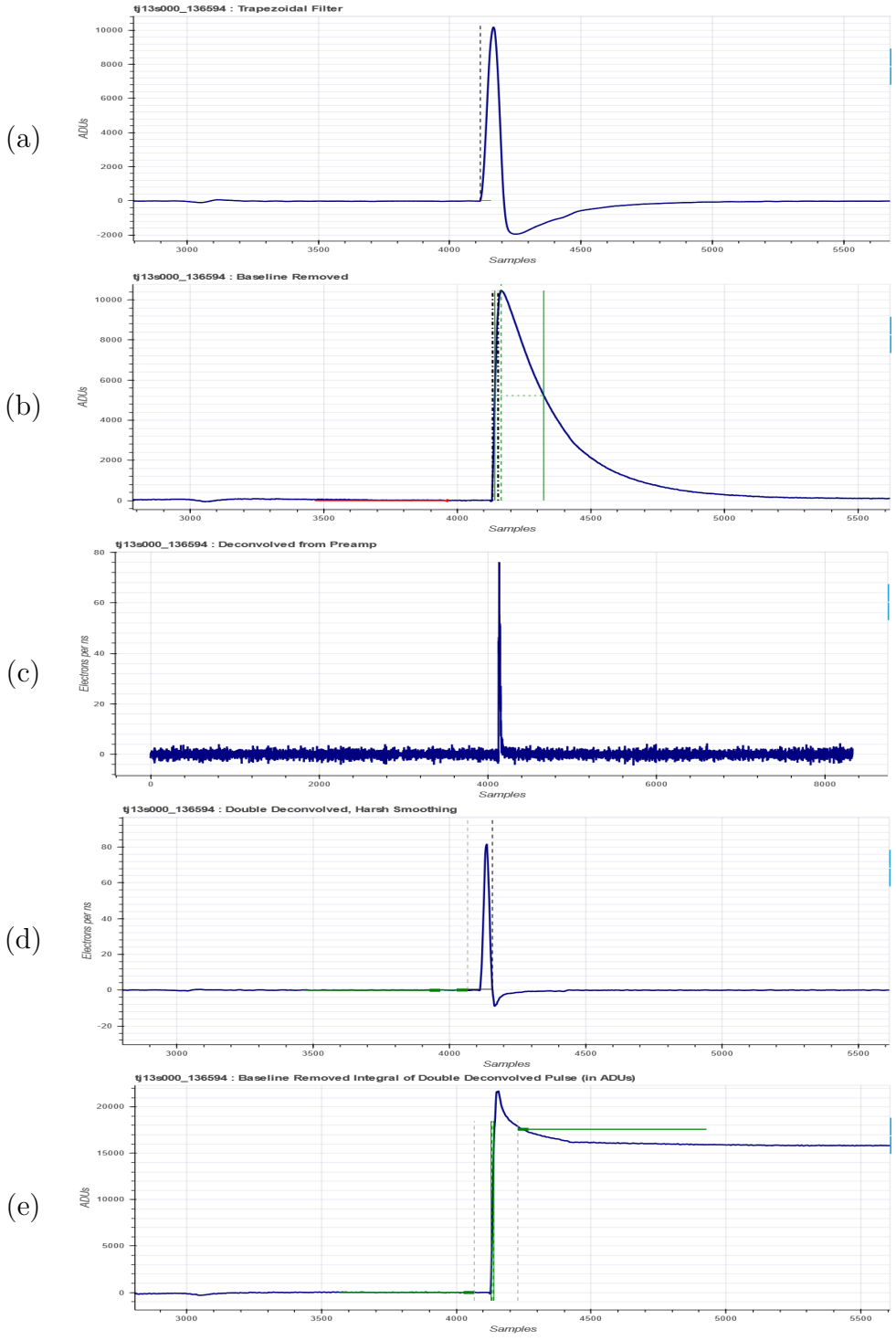

Figure 4.4: The different steps of double deconvolution done by QUADIS. (a) The application of a trapezoidal filter to find the start of the pulse. (b) Baseline removal based on the average value of an 8-sample window. (c) The pulse after the first deconvolution to remove the exponential tail created by the electronics. (d) The pulse after the second deconvolution to remove interference from ion-induced current on the anode. (e) The integrated doubly-deconvolved pulse. The original pulse is shown in Figure 4.3.

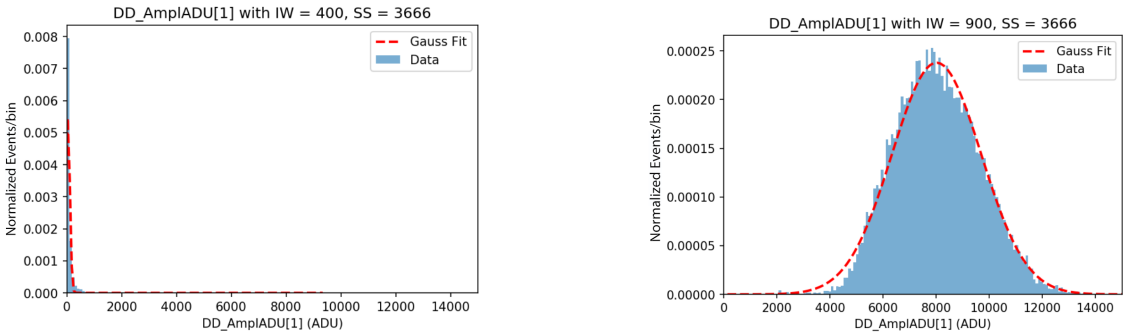

(a) (b)

Figure 4.5: Two histograms showing the 2.8 keV ^{37}Ar decay peak with different integration window widths. (a) has a width of 400 samples, (b) has a width of 900 samples. Here, IW refers to the integration window and SS to the start sample. Each bin has a width of 93.3 ADU.

As can be seen in Figure 4.3, if the start sample location began the integration window at 4400 samples, a significant portion of the pulse will be excluded in the processing. The same is true for a smaller window (e.g. 300 samples) that begins to early (e.g. at 3666 samples), and misses the pulse as well. This will result in a non-Gaussian distribution like the one shown in Figure 4.5(a). Therefore, these two parameters must be optimized to avoid missing segments of a signal, while also limiting the background or other noise included in the integration window.

4.3.2 Optimizing QUADIS Parameters

The achinos sensor was used during the ^{37}Ar calibration test, and the output from one channel was selected for data analysis. Commonly referred to as the "South" or "Far" channel, each signal is sourced from the six achinos anodes located furthest away from the support rod. The SAMBA trigger is based on the South channel, and it has an almost spherically symmetric electric field compared to the "North" or "Near" channel, which is asymmetric around the support rod.

To best find optimal values for the start sample location and the integration window size (also known as "samples from after trigger"), a range of values is selected. SAMBA tries to centre the raw pulse in the middle of the event window, which has a total width of 8333 samples (= 8000 μs). Therefore, the centre sample at 4166, and all signals are ideally centred at this point[1]. The start sample location is varied

[1]SAMBA is not able to successfully centre all signals, hence the choice of a wider spread of integration window widths and start sample locations.

from −16% to +16% of that value in 4% increments [2]. The integration window size begins at a width of 400 samples and increases by 100 sample increments to 1200 samples. The integration window width cannot be larger than 1400 due to the existence of negative baseline transients in the data caused by electronic noise. From this, there are nine different start sample locations and nine different integration window sizes, allowing for a total of 81 different combinations to be tested.

A wider range of parameters (and therefore more unique combinations) was not chosen due to the computational costs of running this analysis. For each parameter set, it takes 1 central processing unit (CPU) approximately 2.5 hours to run the QUADIS analysis. Running the 81 parameter sets selected here takes over 1 CPU-week for this 4-hour run. When choosing the range of each parameter selected, an optimization must be made between the amount of information produced and the time it will take to produce that information.

4.3.3 Initial Processing

To begin the process of optimizing the two different parameters, the same four-hour run had to be processed with the QUADIS software 81 separate times. This accounted for all possible combinations of the nine different values for the integration window, and the nine values chosen for the start sample location. The processing was done through a Python script on a remote server located at Queen's University. To limit the resources used on this server, the processing was completed in batches and saved to the storage on the server.

The ROOT files created by QUADIS are converted into Python dictionaries using the PyRoot package. This allows for data analysis to occur in a Python 3 environment, particularly in a Jupyter Notebook. Due to the limited RAM on the remote server at Queen's University, only specific variables from each processed file were accessed, preventing 81 separate files with 635 MB of data each from being loaded at the same time.

During the loading process, cuts were applied to each of these data to minimize both processing time and the computer memory used. A list of the cuts standard for the NEWS-G collaboration can be found in Appendix A. An important cut made selects the expected 2.8 keV ^{37}Ar decay events, based on a control processed run with a clearly defined peak at this energy. This ensures that only these high-energy

[2] Credit to Daniel Durnford for creating the Python code to run this software on the Queen's server.

events are considered, and low-energy events like the 270 eV decay are not included. A visualization of this cut is shown in Figure 4.6, with a lower limit of 4000 ADU and an upper limit of 12000 ADU.

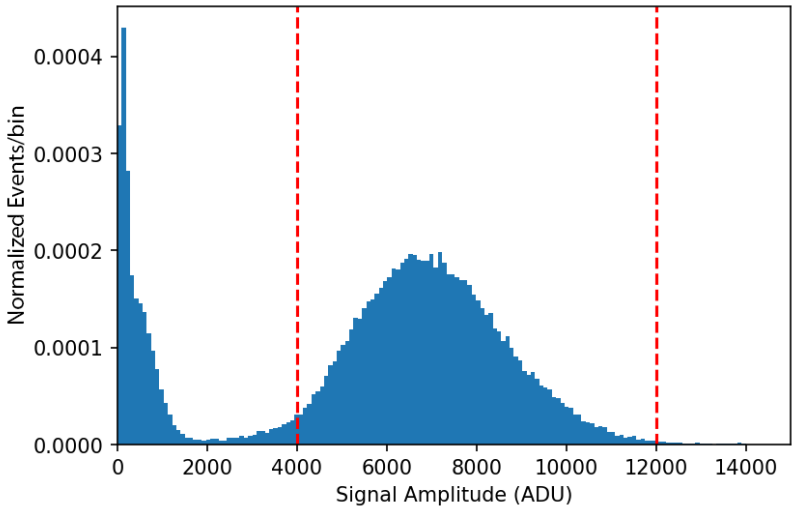

Figure 4.6: The two peaks produced by ^{37}Ar decay in the detector from the tj13s000 run. The two red lines indicate the bounds for the 2.8 keV cut. Low-energy background events are also visible at similar signal amplitudes to the lower part of the low-energy peak. Each bin has a width of 93.3 ADU.

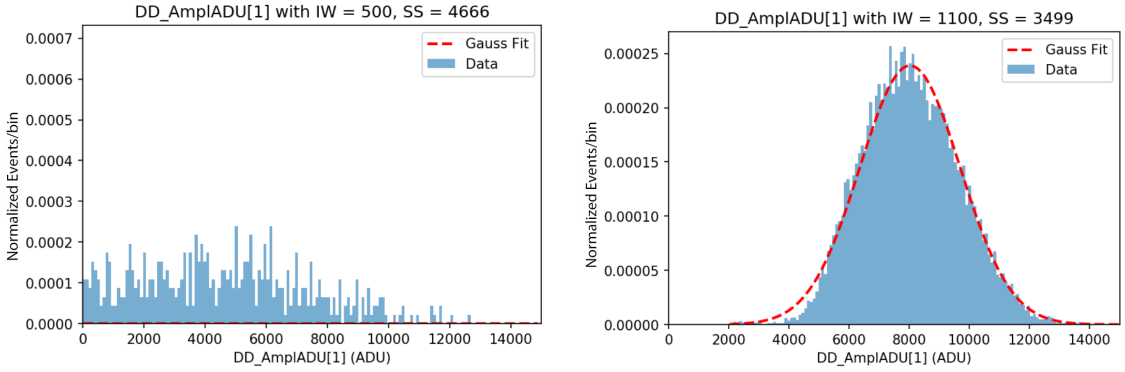

(a) (b)

Figure 4.7: Two histograms of the ^{37}Ar 2.8 keV decay peak with different processing parameters. (a) An example of data that does not follow a Gaussian distribution. (b) Data that closely follows a Gaussian distribution. Here, IW refers to the integration window and SS to the start sample. Each bin has a width of 93.3 ADU.

The selected events were then fit with a Gaussian function to find values for the mean and standard deviation. This fitting uses the "curve_fit" function from

the SciPy Python package, which utilizes a non-linear least-squares method [88]. As shown in Figure 4.7, the accuracy of the Gaussian fit depends on the initial processing parameters. Some of the parameter values create non-physical data since a positive amplitude proportional to the initial event is expected. This typically occurs when the pulses being considered are not contained within the integration window. This can be seen in Figure 4.7(a). The right-hand plot of Figure 4.7 shows processed data that properly reflects the response from the SPC with the 2.8 keV peak clearly defined.

4.3.4 Implementing Mean Value, Standard Deviation, and Resolution

The mean values of each Gaussian fit can be plotted and compared to remove outliers. The distribution of the mean values is shown in Figure 4.8 and is colour-coded. Any mean values that have a negative amplitude are non-representative of the actual detector response and should be omitted. According to Figure 4.8, any start sample location value greater than or equal to 4166 should be excluded from consideration. An additional cut was then applied to exclude mean values below 4000 ADU and to match the cut made in order to isolate the 2.8 keV energy peak. The remaining mean values from this cut are shown in Figure 4.9.

The amplitude resolution is based on the mean value μ and standard deviation σ of a Gaussian distribution, given by

$$\text{Resolution} = \frac{\sigma}{\mu}. \tag{4.3}$$

The value of the resolution relates the mean value to the width of the Gaussian distribution, which should be minimized. However, based on the results shown in Figure 4.10 the resolution does not vary greatly between the different parameters. This lack of variance indicates that a broadening of the Gaussian curve corresponds to an increasing mean value.

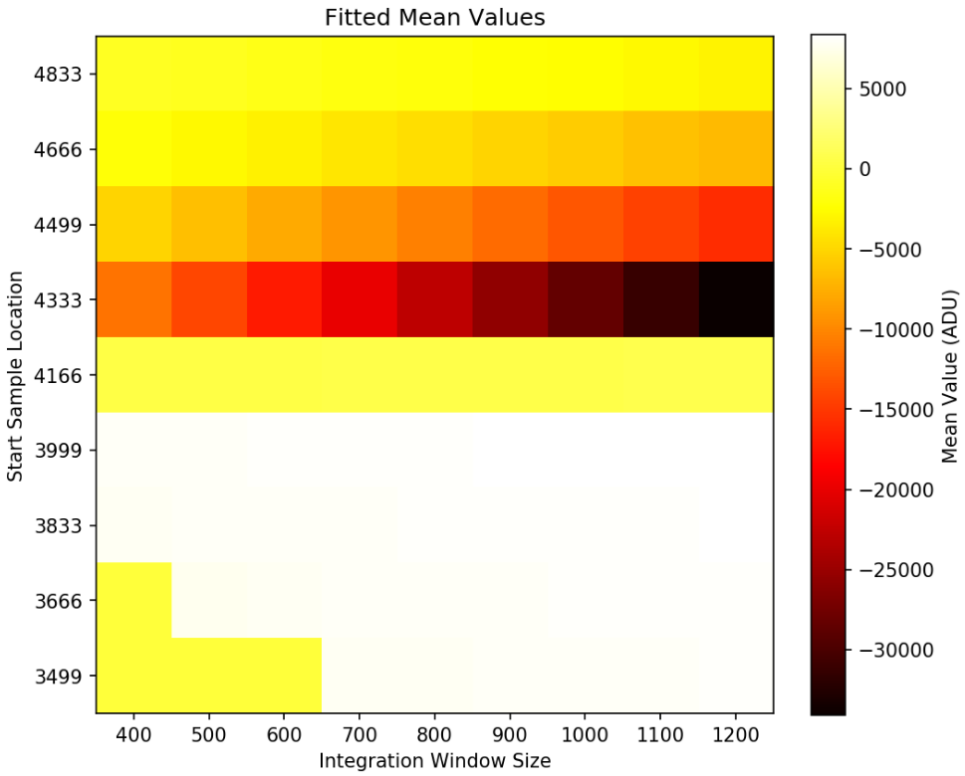

Figure 4.8: Mean values from the Gaussian fitting of the 2.8 keV peak of ^{37}Ar as a function of different start sample locations and integration window widths.

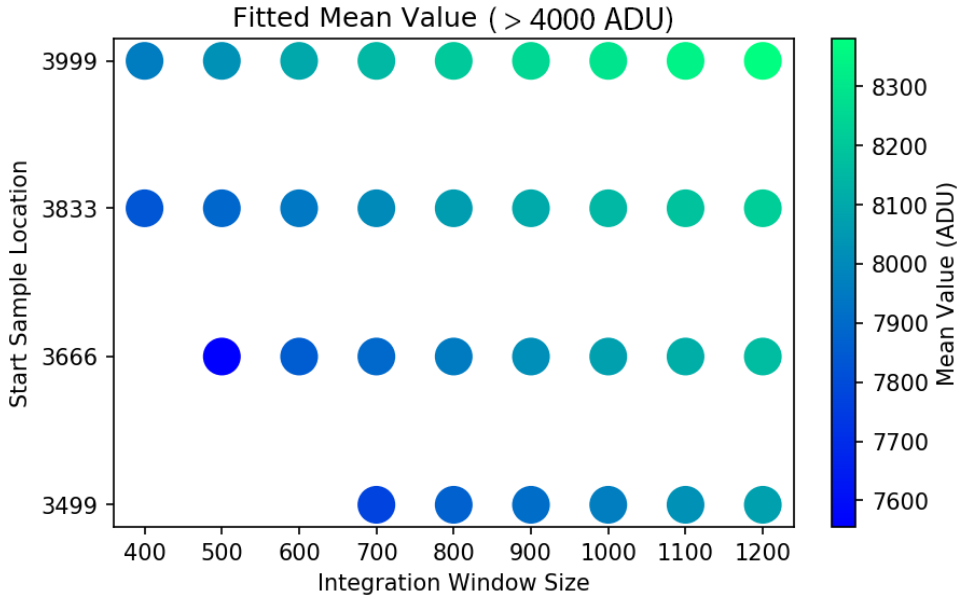

Figure 4.9: Mean values obtained with amplitudes over 4000 ADU as a function of different start sample locations (< 4166) and integration window widths.

The final variable from the Gaussian fit to analyze is the standard deviation. Figure 4.11 shows a plot of the standard deviation values for different start samples and integration window sizes. To determine the optimal values for these two parameters, the standard deviation should be minimized, indicating that the spread of the peak is also minimized. This ensures that the 2.8 keV decay signals in the detector are closer to the mean amplitude of the distribution. A larger standard deviation indicates that some electrons may be missing from the signal while an integration window that is too wide also creates a larger standard deviation.

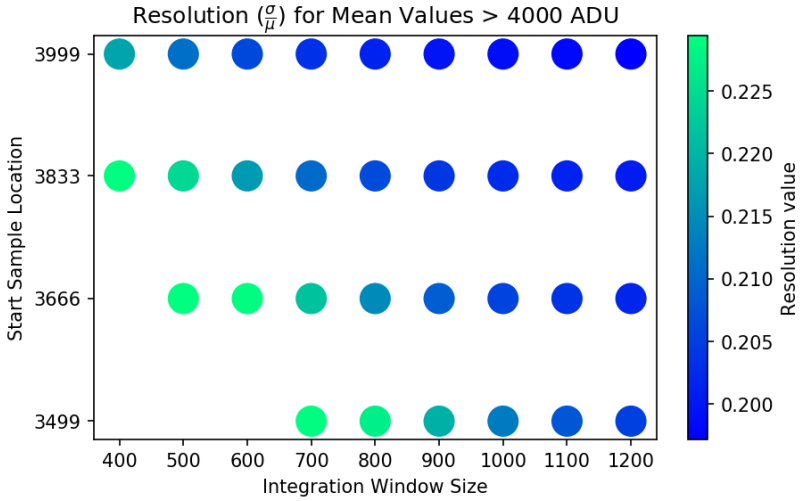

Figure 4.10: The resolution of selected data sets, based on mean amplitude values greater than 4000 ADU. Note that this follows the opposite trend as Figure 4.9.

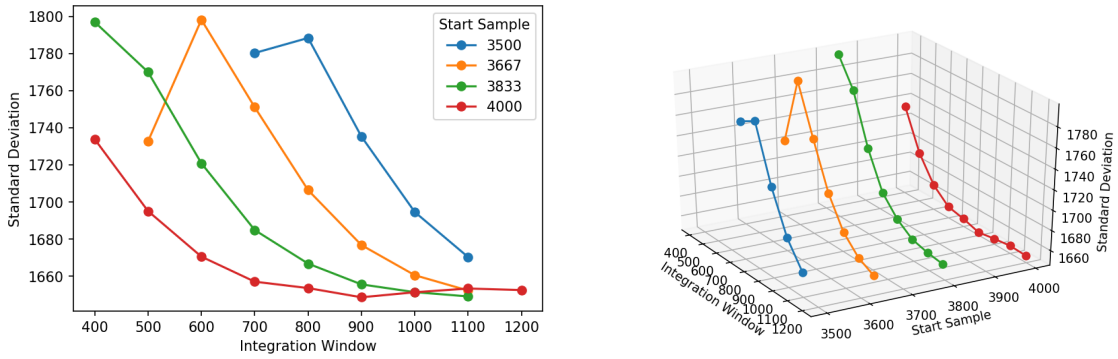

(a) (b)

Figure 4.11: The standard deviation values as a function of the integration window and start sample location for mean values above 4000 ADU. (a) 2-dimensional plot. (b) 3-dimensional plot.

By minimizing the standard deviation in the two plots in Figure 4.11, it becomes clear that start samples of 4000 (red curve) and 3833 (green curve) are ideal candidates. The absolute minimum for the standard deviation value is at a start sample of 4000 and an integration window width of 900 samples. From this process, these are the optimal processing parameters for use in QUADIS.

4.3.5 Cross Referencing Other Variables

Given the result from the parameterization, it is important to cross-reference the results with other values produced from the QUADIS processing. One such parameter is the rise time. Based on simulations of the rise time in the detector, the shape of the corresponding histogram from the 2.8 keV ^{37}Ar decay is well known[2].

A rise time histogram can be created from the run with the optimized parameters and compared to other runs with similar parameters that also have low standard deviation values. Plotting these data together will indicate if the previously found optimal parameters should be chosen, or if there exist better values when the rise time is taken into account.

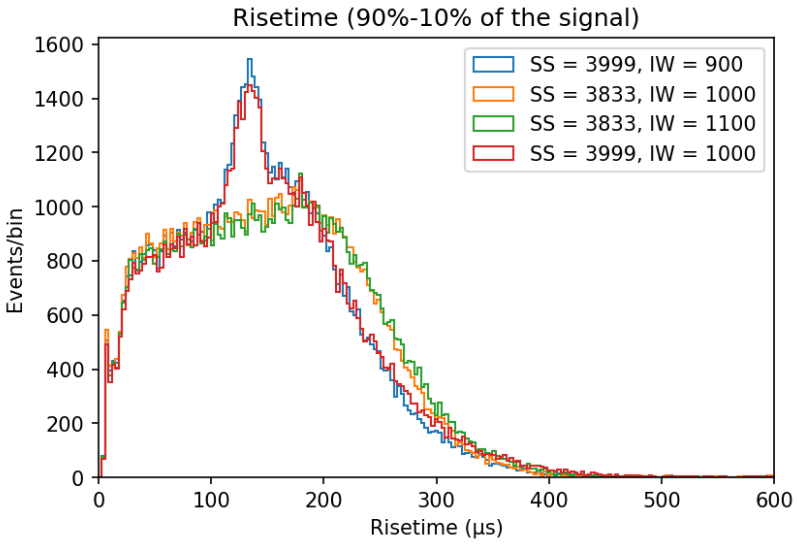

Figure 4.12: The rise time histograms for four separate parameter sets using various start samples and integration window widths. Each bin has a width of 30 μs.

In Figure 4.12, four of these runs are shown with different start sample locations and integration window sizes. The peak shown in both the red and blue colours

[2]Credit to Yuqi Deng for work on these simulations.

indicates that something non-physical is occurring during processing. Given this, the start sample location for the integration window occurs too late in many of the 2.8 keV pulses. This shortens the length of the rise time measured by QUADIS since the first portion of a pulse is missed, resulting in the artificial peak.

From this analysis, the optimal parameter for the start sample location falls before 4000, so the value of 3833 can be used instead. The optimal integration window size is found between 1000 samples and 1100 samples.

4.4 Final Results

Using fitting and optimization techniques from SPC signals of ^{37}Ar decays, the best values for two QUADIS input parameters were found. These are a start sample location of 3833 and an integration window width between 1000 and 1100 samples. These values are used in ongoing analysis for future results publications from the NEWS-G collaboration. Based on these values, the runs with the same detector conditions (e.g. gas mixture, pressure) can be processed. In doing so, less server time is needed and core files using these parameters can be accessed by collaboration members for further analysis. The same type of optimization applied here can be done using the optimal values found as the basis for a better-refined analysis. Similar to how the integration window and start sample location values were selected in the initial processing run, the optimal parameters for the integration window size can be treated as the upper and lower limits for new, finer window sizes. Meanwhile, the ideal start sample location can also be varied, the same as what was done with the centre of the window produced by SAMBA. This method would reduce the CPU time needed compared to running a test comparing the original values, but with higher resolution.

This method can be used for other ^{37}Ar calibration runs within an SPC, and can also be modified when using other sources, such as ^{55}Fe. This process can be automated from the submission of ROOT files into QUADIS to the final results for any relevant data. It can also be used to test other parameters to finely tune each parameter individually. With more parameters involved, however, the complexity and the processing time will greatly increase.

This parameter optimization process cannot be directly applied to the low-energy ^{37}Ar peak due to the non-Gaussian distribution of the energy peak. Low-energy background events are also present and are difficult to distinguish from 270

eV events. In future runs at SNOLAB, lower backgrounds from the environment and longer exposures will allow for improved statistics of low-energy calibration events.

With these results, data analysis for the NEWS-G detector itself can be made easier through the automated optimization of two important QUADIS parameters. Data processing is a very important aspect in the search for WIMPs, but before then, another factor must be controlled. Background activity has been mentioned numerous times, and reducing this activity is vital in the search for low-mass WIMPs. The next two chapters will explore removing a dominant background for the NEWS-G detector; radon.

Chapter 5

Radon

5.1 Radon and NEWS-G

5.1.1 Radon Sources and Progeny

Radon is a naturally occurring radioactive gas that is a daughter nuclide of radium. Common radium isotopes most often produced by either thorium or uranium, both of which are found in the crust of the Earth. The most abundant isotopes of uranium and thorium are uranium-238 (^{238}U) and thorium-232 (^{232}Th), which produce radon-222 (^{222}Rn) and radon-220 (^{220}Rn), respectively. These decay chains can be found in Figure 5.1.

Given that ^{232}Th and ^{238}U can be found in most materials, the resulting emanation of radon contributes to background signals in rare event searches. As discussed in Chapter 3, there are methods employed to reduce the radioactive background in detector materials.

Radon is a noble gas, meaning that 86 electrons are distributed to perfectly fill all six of its electron orbitals. This creates an inert particle that will only form bonds with highly electronegative atoms, like fluorine at high temperatures ($\sim 500^{\circ}$C) [89]. Due to the non-reactivity of radon, mechanical methods like radon traps or stripping columns are used to capture radon rather than chemical methods.

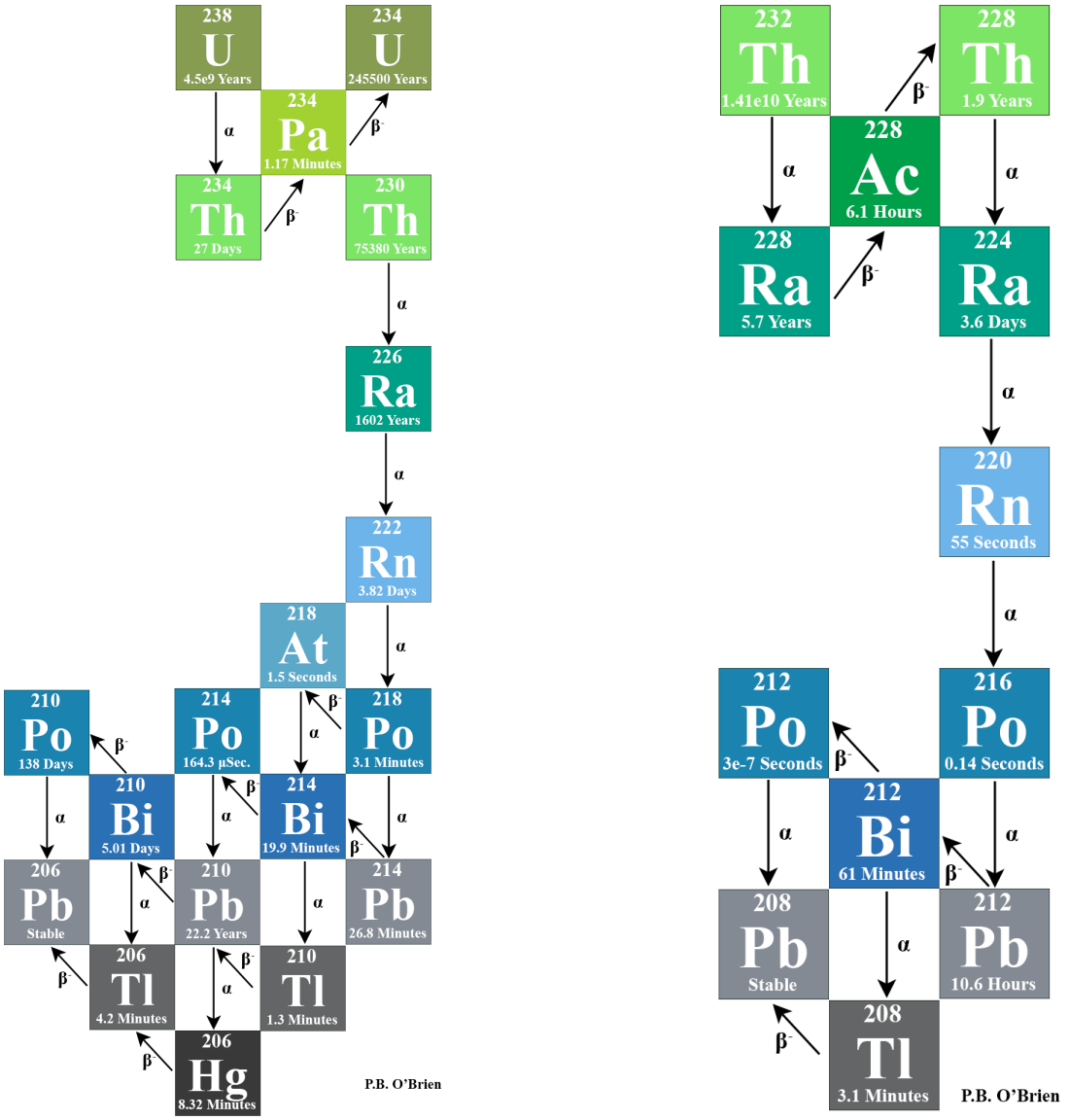

Figure 5.1: The decay chain for: (a) uranium-238. (b) thorium-232. While Rn^{220} is a short-lived isotope, Rn^{222} has a longer half-life. Within the decay chain of Rn^{222}, Pb^{210} has a half-life of 22.2 years, meaning it can stay in the detector for a long time [90].

Radon releases an alpha particle in its decay, losing four nucleons in the process as it converts to a polonium atom. Of interest are the two previously mentioned isotopes, ^{222}Rn and ^{220}Rn (thoron). These have respective half-lives of 3.8 days and 56 seconds [91]. The resulting polonium isotopes produced are not long-lived, with polonium-218 ^{218}Po having a half-life of only 3.1 minutes. These polonium isotopes

usually produce an alpha particle, but ^{218}Po and ^{216}Po can emit beta particles. Referring to Figure 5.1, there are other beta decays that take place in the radon decay which are recorded as low energy events in NEWS-G.

5.1.2 Radon in NEWS-G

As mentioned in the previous chapter, the emission of an alpha particle causes a path event that frees many electrons. The high volume of ions creates a signal with an amplitude that extends beyond the maximum readability of the electronics. The saturated event, an example of which is shown in Figure 5.2, can be easily identified as a high-energy alpha event. Secondary ions that are produced from this event can take up to several seconds to cease drifting, which alters the gain of the detector. During this period, low-energy rare events may not be detected due to the changing electric field. Low-energy background events are also produced in the detector from radon progeny. ^{218}Po and ^{216}Po can decay via beta emission as well as isotopes of lead, bismuth, thallium, and mercury.

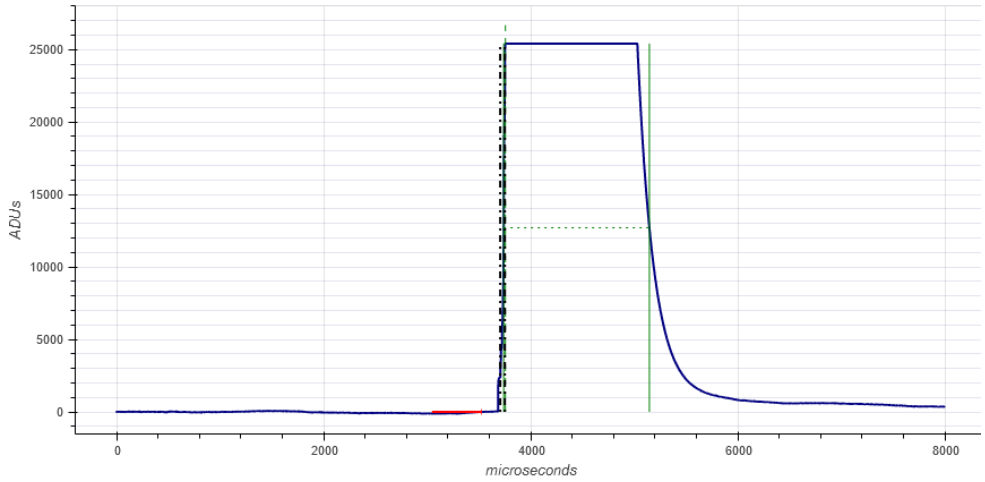

Figure 5.2: An example signal created from an alpha particle in the NEWS-G detector. As evidenced by the flat top of the pulse, the signal is saturated from the high-energy particle. While events like these are simple to exclude, low-energy events are created as a result, adding to the background activity.

An electroplating method (discussed in Section 3.3.1) has been developed to remove radon from the inner surface of the detector to mitigate the aforementioned background signals. In conjunction, low-activity materials are used in all components of the detector system, like the Gas Handling System (GHS). The achinos is also specially manufactured using low-activity materials, and new methods involving

3D resin printing are being investigated.

A major source of radon within the gas is the filter called the Getter. In the GHS, this filter is used to remove electronegative impurities, like water and oxygen, that interfere with ion drift. Typically used in vacuum systems, the absorbing material of the Getter emits radon as the gas passes through. Due to the importance of this component in the NEWS-G GHS, a method to trap the emitted radon, as well as naturally occurring radon, is required.

5.2 Radon Adsorption and Removal

5.2.1 Radon Adsorbing Materials and Mechanics

Since radon is a noble gas that is non-reactive with most other elements, it must be trapped through non-chemical methods. This trapping is based on several properties of radon, such as the size of an individual atom and its affinity for adhesion to other materials. This adhesion is also referred to as adsorption, which has been measured for radon with a variety of materials. These include polycrystalline metals [92], zeolites [93], and activated charcoal [94]. From previous studies, materials can be selected based on their enthalpy of adsorption of radon, and a filter can be constructed and tested.

Van der Waals forces dictate the adsorption of radon, so a higher surface area is desired. This can be achieved by using porous granules of a material [95]. The temperature also has a significant effect on radon trapping. In materials like activated charcoal, lower temperatures will increase its ability to adsorb radon [96].

Desorption also occurs in these trapping materials, meaning that radon can exit its adsorption sight. This material property indicates that the porous radon trapping materials are unable to trap all of the radon passing through them, leading to the re-emission of radon. Since radon can decay while passing through the trap, not all of the radon will be re-emitted. This re-emission and decay process within the radon trap is discussed in more detail in Chapter 6.

5.2.2 Activated Charcoal

Activated charcoal (also referred to as activated carbon) is used for radon removal in gases and is commonly found in radon mitigation systems like that of the DEAP-3600 detector [97, 98, 99]. Different activated charcoals under the same conditions

will perform differently as shown in Figure 5.3. They also demonstrate different adsorption levels when cooled to different temperatures and the amount of radon they adsorbed is measured by the radon adsorption factor K [95]. This value is calculated by Noel *et al.* as

$$K = \frac{A}{C} \text{ [m}^3\text{/kg]}, \tag{5.1}$$

where A is in Bq/m^3 trapped by the material, as measured by a germanium counter, and C (Bq/m^3) is the radon activity in the gas before entering the trap. To quantify K, gas is flowed through a radon source and into a buffer volume containing a diffusion radon detector. The radon activity of the gas is then measured again after passing through the radon trap (where the gas was then exhausted) and gas continues to flow until the output radon activity is stable. This implies an equilibrium between radon in the gas and radon adsorbed by the trap, and the values of A and C can then be measured.

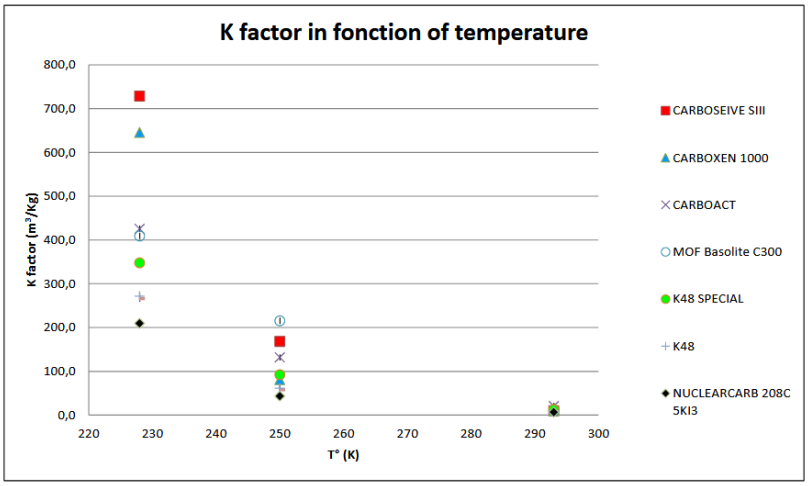

Figure 5.3: The relation between adsorption by different trapping materials based on the activated charcoal type and its temperature. Higher temperatures limit the amount of radon adsorbed [100].

For the testing discussed later in this chapter, Carboxen® 1000 (Sigma Aldrich) was selected based on its relatively high adsorption of radon at low temperatures. The process for manufacturing this material is highly controlled to produce a specific porous volume within the granules, and the granular size is between a 60- and 80-mesh (250 μm to 177 μm diameter). The material comes in powder form and has a surface area of 1200 m^2/g [101].

While previous experiments have used refrigerators or liquid nitrogen to cool the material, dry ice was used to cool the Carboxen® 1000 to around -80°C, decreasing the complexity of the cooling process. To reverse the adsorption process, activated charcoal can be heated to release the trapped gas molecules.

5.2.3 Silver Zeolite

Silver zeolite (also Ag-ETS-10) is another porous material, and the specific product used was produced by Extraordinary Adsorbents (EA) in Edmonton, Canada [102]. Zeolites are aluminum- and silicon-based minerals (aluminosilicates) that have a porous structure able to incorporate positive ions, like Ag^{2+}. These ions are not tightly held by the zeolite and can easily be exchanged with other like ions. The zeolite produced by EA differs slightly in its composition, replacing aluminum with titanium to create a titanosilicate. Zeolites have been shown to adsorb radon well due to their porous structure [93]. Since the silver zeolite is a new material, the background activity was measured using an ultra-low background germanium counter in SNOLAB. The results related to the various radon decay chains from an 8.9 g sample are shown in Table 5.1. The effects of silver zeolite on other gases like methane have not yet been well studied and preliminary results will be presented in Chapter 6.

^{238}U (^{226}Ra)	^{238}U (^{234}Th)	^{232}Th	^{210}Pb	^{228}Ac
987.90 ± 47.62	2022.00 ± 390.10	601.40 ± 43.04	3437.90 ± 2156.00	398.90 ± 76.70

Table 5.1: The background activity of Ag-ETS-10 sample measured at SNOLAB [103]. Isotope progeny in brackets were used to extrapolate the activity of the original element. Units are in mBq/kg.

5.2.4 The Radon Trap

Utilizing activated carbon and silver zeolite, I constructed a radon trap to contain these materials. To test them, the trap must be compatible with a gas circulation system I also designed and constructed. Several 20 cm lengths of 1.27 cm diameter stainless steel tubes were used to hold the trapping materials. To prevent any materials from escaping the trap, a small amount of fibreglass was used to cap either end of the filled tube. The radon trap is then connected to the 0.635 cm stainless steel piping making up the rest of the Radon Trapping System (RTS). An image of the radon trap is shown in Figure 5.4 along with the two important dimensions for calculating the volume of material present in the trap. The length of

the trap L_{Trap} and the inner diameter of the trap D_{Trap} are measured as 20.0 ± 0.1 cm and 1.270 ± 0.005 cm, respectively. The mass of the material within the trap is also important to know, and is recorded for each trapping material used.

In previous studies about radon trapping materials, some radon is adsorbed by the materials, while some radon can pass through the trap. Due to the high affinity for adsorption within targeted trapping materials, the flow rate of radon that does pass through the trap is greatly reduced relative to the flow rate in the rest of the system. From studies conducted by Karunakara *et al.*, the flow rate of radon through the trapping material differs with temperature [104]. This will be discussed in greater detail in Chapter 6.

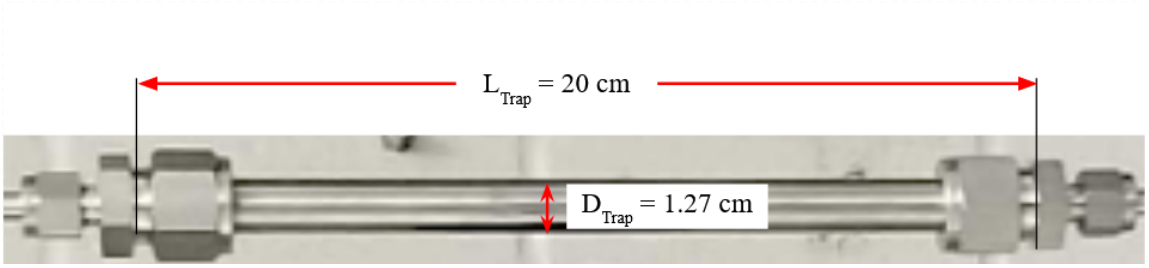

Figure 5.4: An image of the radon trap with the appropriate dimensions labelled. The length of the trap is $L_{\text{Trap}} = 20$ cm and the inner diameter is $D_{\text{Trap}} = 1.27$ cm. An adapter on either end of the trap connects it to the RTS.

5.3 Radon Trap Testing

5.3.1 Experimental Setup

To test the efficiency of the selected radon trapping materials with different gases, I designed and constructed a circulation system, as shown by the Piping and Instrumentation Diagram (P&ID) in Figure 5.5. The major components of this system are the radon trap, RAD7 (DURRIDGE Company Inc), Binary Gas Analyzer (BGA, Stanford Research Systems), desiccant, pressure gauge, and particulate filter. Not indicated in the P&ID is the vacuum pump, which is temporarily included to remove gas from the system. Unless otherwise indicated, the piping is stainless steel 1/4", connected via Swagelok connectors and adaptors.

The pressure gauge is used when the system is vacuumed and then when it is filled with a gas. Due to pressure limits for the RAD7, the system cannot exceed a relative pressure of 0.05 bar above atmospheric pressure. The pressure gauge has

been calibrated to Standard Atmospheric Pressure and acts as an indicator for when gas filling can be halted. It is important to include a particulate filter after the radon trap to prevent any granules of material from entering sensitive equipment within the RTS loop.

The RAD7 has humidity limitations as well, necessitating the use of a low-activity desiccant, also from DURRIDGE. Small amounts of water vapour may enter the RTS through the RAD7 due to unpreventable faults. Having a dry environment prevents water vapour from being adsorbed by the radon trap, which may affect the results from adsorption testing of other gases.

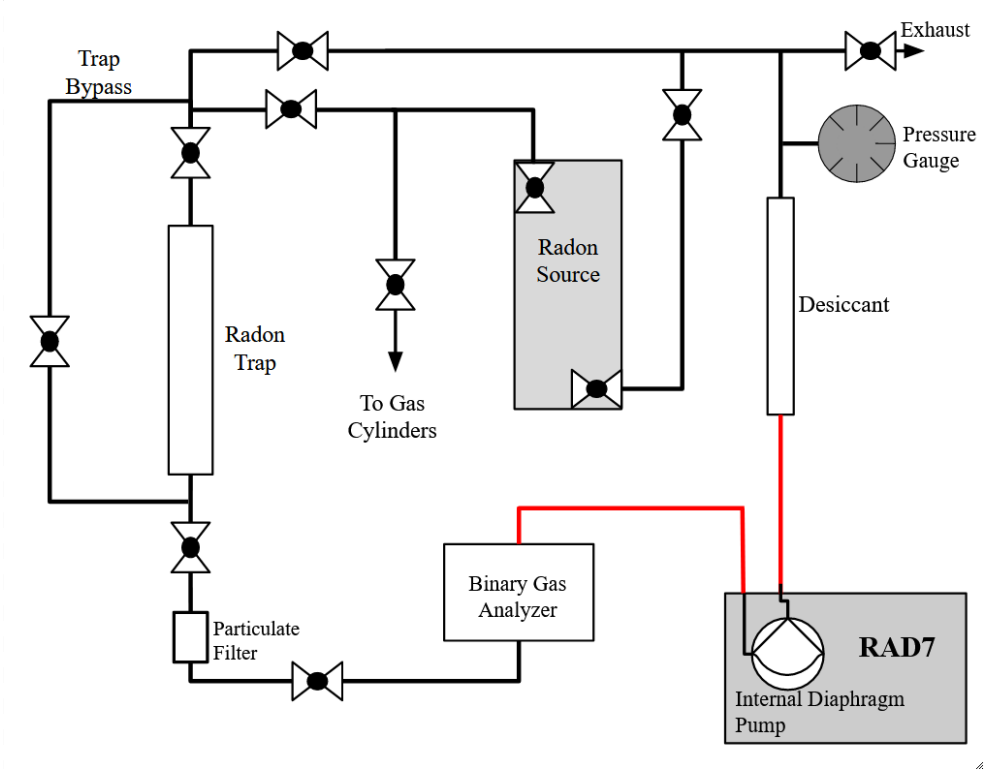

Figure 5.5: The P&ID for the RTS. All black lines are stainless steel tubing. Red lines denote polyvinyl tubing.

The RAD7

The RAD7 is a continuous radon monitoring device capable of spectral analysis for different radon isotopes. It can make this distinction based on the energy of an alpha particle emitted by various polonium isotopes. To determine the energy of the particle emitted, the RAD7 makes use of a semi-conductor that is surrounded by a high voltage hemisphere. When a radon atom decays through an alpha emission

within the hemisphere, a charged polonium particle is produced. This positive ion is forced onto the surface of the semiconductor by the electric field, where it then decays by emitting an alpha particle, creating a signal. The energy of the alpha particle is distinct for each polonium isotope. Based on a proprietary calibration process, the RAD7 can then distinguish the activity for each radon isotope. This process is shown in Figure 5.6. The device can measure alpha decays of ^{218}Po, ^{216}Po, ^{214}Po, ^{212}Po, and ^{210}Po.

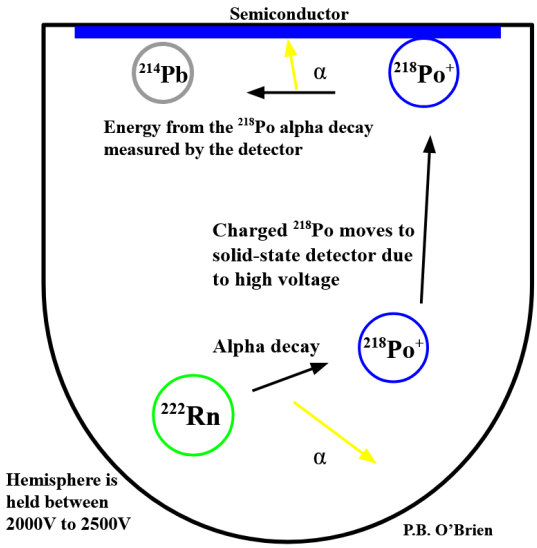

Figure 5.6: A diagram demonstrating the operation of the RAD7 with an example ^{222}Rn atom decay.

The RAD7 also contains a temperature and humidity sensor, the latter of which can be used to detect humid air leaking into the system. A diaphragm pump is also found in the RAD7 and can be used to circulate gas through the system at 1 L/min. In addition, there is an internal filter present to remove any particulates from a gas. The connections between these internal components were found to leak based on results from a helium leak detector. Measures were taken to mitigate these leaks, but the RAD7 could not be brought to the same level of vacuum as the rest of the RTS. The external connections of the RAD7 are shown in Figure 5.7.

The RAD7 has been well calibrated using known sources from DURRIDGE, and is able to account for factors such as high humidity through its on-board processing. There is also the possibility of "spillover" within the RAD7, in which a detected alpha decay of one polonium isotope is recorded as a different isotope. This spillover effect is also well-known, and is accounted for by the on-board processing. The main

source of error within the activity data recorded by the RAD7 is from the statistical error, which is discussed in detail in Chapter 6. The RAD7 also has a lower limit of activity that it can measure, based on the background activity of its internal components. As measured by DURRIDGE, the background activity is 1 count every two hours, which equates to 0.15 mBq.

Figure 5.7: An image of the RAD7 external interface. Vinyl tubing is attached to the inlet and outlet and the serial port interfaces with the CAPTURE ® (DURRIDGE Company Inc) software. The RAD7 can be controlled via the LCD screen and buttons.

The Binary Gas Analyzer

The BGA can determine either the purity of the gas or the composition of a binary gas mixture. It does this by measuring the speed of sound in a gas, which depends on the gas species and the temperature. By making accurate measurements of both values, the BGA can compare its measurements to a database of over 500 gases to determine the purity of a gas or the relative amounts of two gases in a mixture. An example readout from the BGA is shown in Figure 5.8 for a mixture of P3 argon-methane (P3 denotes a 97/3 mixture of argon/methane).

The BGA was primarily used to determine the relative concentration of methane in argon and monitor for methane adsorption. Previous evidence from NEWS-G runs indicate that an activated charcoal trap adsorbs methane. This has been tested, with the results discussed in Chapter 6. The BGA is also useful for finding leaks based on gas purity measurements. Small leaks can be identified based on long-term changes in the composition of the circulating gas. This method in combination with a helium leak detector (Agilent) allows for the rapid identification of leaks within the RTS.

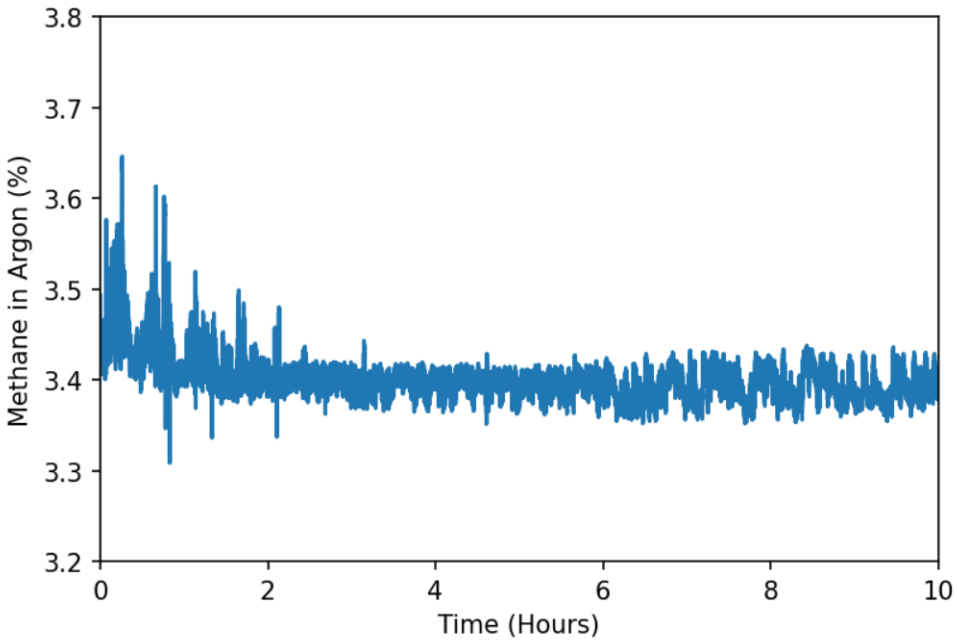

Figure 5.8: The relative concentration of methane in argon measured by the BGA. On average, there is a concentration of $3.40 \pm 0.03\%$ of methane for the P3 mixture.

The experimental error within the readout of the BGA depends on three factors: the accuracy of the speed of sound measurement; the gas temperature; the gas pressure. The configuration of the BGA for this experiment does not include a pressure transducer, and so only the error from the speed of sound measurement ($\pm 0.02\%$) and the temperature ($\pm 0.1°C$) can be determined. In Figure 5.8, statistical error is also included in the average value and is typically 1% of the value (i.e. 1% of 3.4%). The statistical errors is more significant than errors in the measurement, which are deemed negligible. The BGA device is pictured in Figure 5.9, including its touch interface.

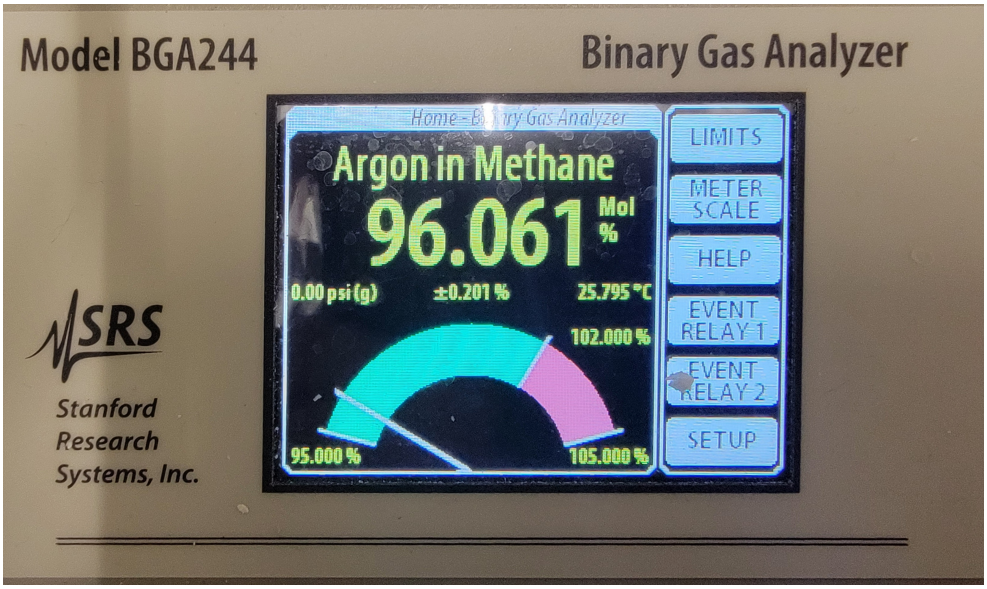

Figure 5.9: The BGA device and interface. Information on the touch display includes the temperature, relative gas concentration, and reading error. The red bar on the right side of the green semi-circle indicates a customized limit that notifies the operator about significant changes in the concentration. Pictured is the measurement of argon in methane.

5.3.2 Gases

The gases used for testing the radon trap were selected based on availability and relevance to the NEWS-G experiment. Since the intended gas mixture for the NEWS-G SNOLAB installation is methane and a noble gas, a premixed gas of argon and 3± 0.3% methane (Praxair) was selected to perform the test. Argon was used as a control gas so that the effects of methane on radon adsorption could be determined. Finally, nitrogen was also used for testing the RTS and commissioning runs.

Nitrogen (N_2) is a common gas that is inert and was available in a virtually limitless supply. During the construction of the RTS, N_2 was used to test the different components for leaks and longevity operations. It was also used both in circulation tests and flow-through tests, in which the gas passes through the system once before being exhausted. During this time, the laboratory supply of nitrogen was tested for background radon activity, and it was found that the activity was 0.14 ± 0.08 mBq, which matches the expected background activity of the RAD7.

N_2 is also utilized to clear the RTS between any two runs in a flow-through configuration. This prevents radon that may have been injected into the system from being circulated and also removes any other gas that may be present. Having

N_2 flow through the radon trap during a reset is important to remove radon that is released from the trap. This is discussed in more detail in Section 5.3.3.

While neon and xenon are being considered for use with the NEWS-G SNOLAB installation, argon was selected since it has similar properties, while having a lower cost. This is also why an argon-methane mixture was chosen.

5.3.3 Procedure

A standard testing procedure was created to ensure the uniformity of testing conditions.

Contaminant Removal and Regeneration

The first step is to remove any contaminants within the RTS. N_2 is flowed through the system and exhausted through a fume hood. During this time, the radon trap is then heated to 120°C for Carboxen and 160°C for silver zeolite to remove radon and other gases that may have been adsorbed by the trapping material ($\sim$ 20 minutes). The higher temperature used for silver zeolite is recommended by the manufacturer. The activity of the nitrogen passing through the heated radon trap is measured from the RAD7, and heating is stopped once the activity in a two-minute interval goes below the minimum sensitivity of the RAD7 (0.15 mBq). The nitrogen supply is then stopped and a turbo vacuum pump is connected to the exhaust of the system. Due to internal components in the RAD7, the minimum achievable vacuum within the RTS was found to be on the order of 10^{-5} Torr, while pressures on the order of 10^{-7} Torr were achieved when the RAD7 was removed from the system. During this vacuuming process, the radon trap is heated to remove any radon. The process of heating the radon trapping material to release adsorbed gases is known as the regeneration process.

RTS Filling and Circulation

The radon trap temperature is monitored by a thermocouple adhered to the exterior surface of the trap. Once the trap has returned to room temperature after a regeneration process, the RTS is filled with the appropriate gas. The pressure of the gas is monitored until the desired pressure of 0.02 bar above atmospheric pressure is achieved. Before filling, the BGA is set up to monitor the gas or gas mixture. Circulation then begins in the RTS by using the internal pump of the RAD7. In

cases where the RAD7 was removed from the system, an external pump with the same specifications (1 L/min) as the RAD7 pump was used.

(a) (b)

Figure 5.10: The radon source: (a) as produced by Pylon. (b) modified with stainless steel piping. The desiccant (right side white tube in (a)) was replaced with an inline desiccant that uses Swagewlok connections in a different section of the RTS.

Radon Injection

At this point, the procedure splits into one of two options: radon is injected into the system, or not. Radon is not introduced into the system in tests where radon may interfere with other results, such as the adsorption of methane in the radon trap. For this case, the next paragraph of the procedure is skipped.

To inject radon into the RTS, a modified flow-through radon source is used (Pylon 1025). The modifications to the source were made to limit any leaks that may occur when using plastic tubing. A before and after picture of the radon source is shown in Figure 5.10. The radon source uses dry radium-226 (^{226}Ra) to produce a calibrated quantity of ^{222}Rn, with an equilibrium activity of 0.93 kBq and a continuous rate of 117.49 mBq. Several valves can be opened to circulate the gas in the RTS through the source, which is done for 15 minutes for each test. The gas is then allowed to circulate for 21 hours to determine the background activity of the ^{222}Rn. While the expected half-life is 3.8 days, this can be confirmed in the analysis of the RAD7 data.

Radon Trap Opening

The radon trap is then opened while the bypass is closed, forcing the gas through the trap. At this point, the trap either remains at room temperature, or has been cooled to about -80°C using dry ice. A polystyrene box surrounds the trap and is refilled with dry ice throughout the run to ensure that a constant temperature is maintained. The effects of both temperatures will be discussed in Chapter 6. Once the test has finished, the radon trap is reset using the Contaminant Removal And Regeneration process outlined previously. An image of the full RTS is shown in Figure 5.11.

(a) (b)

Figure 5.11: An (a) head-on view and (b) top angle view of the RTS I constructed in the Piro Lab the University of Alberta (CCIS L2-243).

Chapter 6

Results and Discussion

6.1 Introduction to Analysis

The analysis of data produced from experiments conducted in the RTS can be directly applied to the construction of a radon trap for the NEWS-G experiment at SNOLAB. By observing the adsorption of radon by different materials, an optimized set of conditions can be found to maximize radon adsorption, while avoiding any radon that may be re-emitted from the trapping material. Specific parameters about this experiment like the pump flow rate, pressure, and gases used were chosen to create similar conditions to the NEWS-G GHS. This chapter is partitioned according to the trapping material and trap temperature, with another section highlighting the adsorption of methane within the Carboxen® 1000 (Carboxen) material. The data used is supplied by the RAD7 for the radon activity and by the BGA for the variations in methane concentration.

An important parameter that will be investigated in this analysis is the re-emission of radon from the trapping material. It has been noted in previous experiments (such as Abe *et al.*) that a portion of the radon that enters the trap can be re-emitted periodically [98]. This phenomenon is a concern for NEWS-G as the reintroduction of radon into the GHS and detector can lead to increased levels of background activity. Therefore, an ideal filling window can be found based on results from the experiments conducted in the RTS.

The RAD7 outputs the total activity of ^{222}Rn and ^{220}Rn and provides a percentage for each polonium isotope decay recorded. Of interest to this experiment is ^{222}Rn, since it is the longest-lived isotope. Therefore, the percentage of ^{218}Po is

multiplied by the total activity measured to give that of ^{222}Rn. This is given in counts per minute (cpm), which is then converted into Becquerels (Bq).

6.1.1 Radon Reduction Calculation

As mentioned in Chapter 5, the K factor was used to directly compare the adsorption abilities of different trapping materials [95]. Due to the differences in the experimental setup, this value cannot be calculated in the present work since the value of adsorbed radon could not be measured. This necessitates the definition of a new parameter to directly compare different runs in this closed-loop circulation system. The new parameter is the Radon Reduction Ratio (R-value) and is denoted by

$$R = \frac{A_0}{A_{f,\text{avg}}}, \tag{6.1}$$

where the value of A_0 is the activity of ^{222}Rn right before the trap is opened. The value of $A_{f,\text{avg}}$ is the average activity over a specified window whose size depends on the run. For a run at room temperature (RT), the window is ten hours wide and begins two hours after the activity within the trap is stabilized. The period of large fluctuations before this stable time is referred to as the stabilization time and begins when the radon trap is opened. For dry ice (DI) runs, the average activity window is measured between the stabilization time and the beginning of the radon re-emission. This window size is typically on the order of days.

Unpreventable leaks within the RTS (primarily within the RAD7) means that the radon activity decreased more rapidly than the expected 3.82 days half-life. As an example, the plot in Figure 6.1 shows the activity of radon circulating with the argon + 3% methane (Ar+M) mixture followed by the opening of the radon trap and then its regeneration. An exponential fit of the initial activity yields a half-life of 2.34 ± 0.05 days, only 61% of the expected half-life. The reduction in ^{222}Rn at a faster rate than its decay rate is also shown visually in Figure 6.1 by the green fitted curve. When the radon is re-emitted from the trap, it does not return to the expected activity.

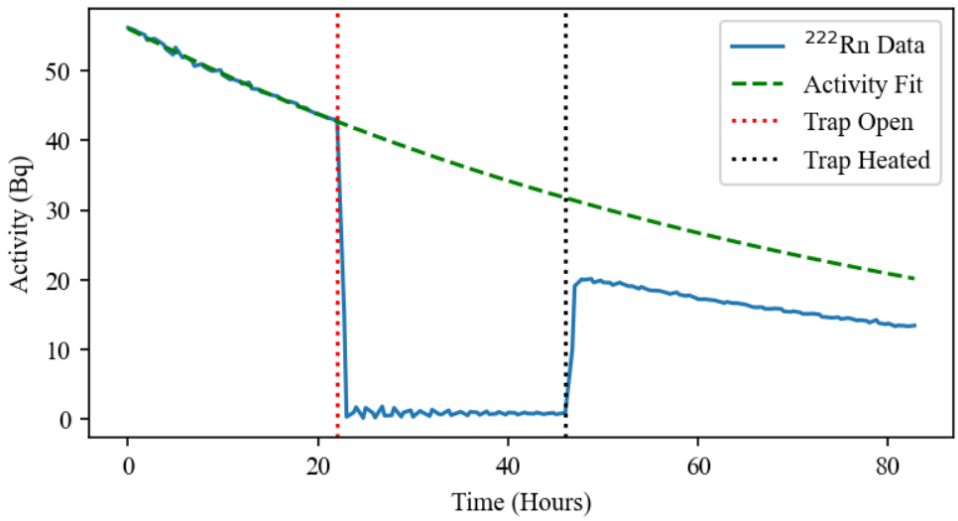

Figure 6.1: Radon activity with radon adsorption (trap open) and re-emission (trap heated and closed) highlighting leaks present in the RTS. The result was obtained using Ar+M gas mixture at ambient temperatures.

Due to the unreliability of a fit based on the activity of ^{222}Rn before the trap is opened, the value of A_0 is used as the initial activity. Given that a standard procedure is followed, the R-value is directly comparable across all runs.

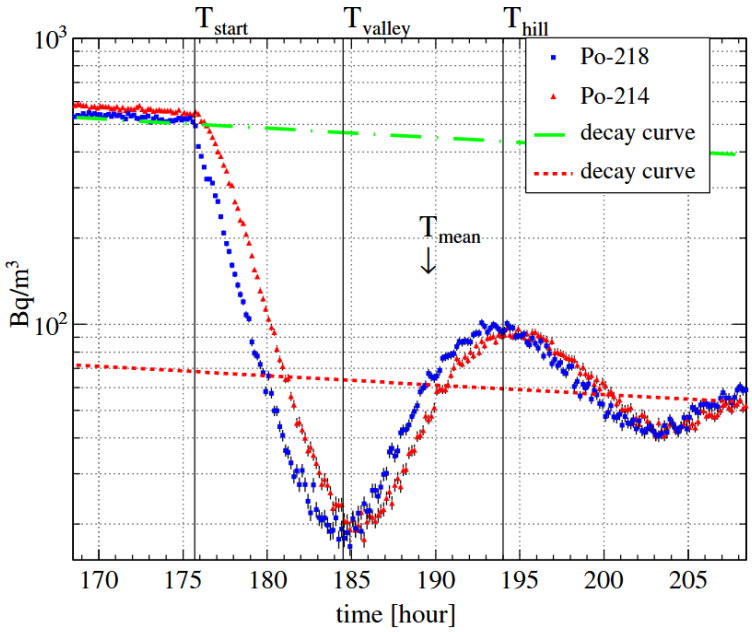

Figure 6.2: An example of the oscillations from a radon trap in the experiment conducted by Abe *et al.* T_{start}, T_{valley}, and T_{hill} are indicated by labels vertical lines [98].

6.1.2 Flow Rate Calculation

Experiments conducted by Abe *et al.* indicate that a mean propagation velocity of radon in activated charcoal compared to the propagation velocity of xenon can be found [98]. In this study, the trap temperature and gas species remained constant while the flow rates and trap lengths were altered. An adapted method from the one described by Abe *et al.* will be applied for this analysis to find the flow rate of radon f_{Rn} and methane $f_{\mathrm{CH_4}}$ in the Carboxen. The same method from Abe *et al.* to find T_{Rn} was used for silver zeolite materials.

To determine the value of f_{Rn}, the time it takes for the radon to pass through the trap must be known. This can be calculated based on the re-emission and re-adsorption of radon within the trap, an example of which is shown in Figure 6.2. Since the damped oscillations of the radon activity are periodic, the mean time T_{mean} can be calculated as

$$T_{\mathrm{mean}} = (T_{\mathrm{valley}} + T_{\mathrm{hill}})/2. \tag{6.2}$$

From Figure 6.2, the values of T_{valley} and T_{hill} correspond to the first minimum and maximum respectively after the trap is opened. From the T_{mean} value, the absolute time that it takes for radon to flow through the trap is given as

$$T_{\mathrm{Rn}} = T_{\mathrm{mean}} - T_{\mathrm{start}} \tag{6.3}$$

where T_{start} is the time when the radon trap was opened.

This method of calculations has several limitations since it requires the presence of multiple extrema. In cases where the activity oscillations are highly damped or in runs where there are long periods between a re-emission of radon, only one extremum may be present, limiting the capabilities of this calculation when applied to this work.

A modified method can be applied to account for multiple peaks that have fewer data within each peak. If the oscillation of radon activity is periodic, then the relative value of T_{mean} should be the same for any two adjacent hills and valleys. The average time between all of the hills and valleys can be found using the following equation:

$$T_{\mathrm{Rn}} = (T_{\mathrm{hill,avg}} + T_{\mathrm{valley,avg}})/2. \tag{6.4}$$

The values of $T_{\mathrm{hill,avg}}$ and $T_{\mathrm{valley,avg}}$ are calculated as

$$T_{\mathrm{hill,avg}} = \frac{1}{N}\sum_{n=2}^{N}(T_{\mathrm{hill,(n)}} - T_{\mathrm{hill,(n-1)}}) \tag{6.5}$$

$$T_{\mathrm{valley,avg}} = \frac{1}{N}\sum_{n=2}^{N}(T_{\mathrm{valley,(n)}} - T_{\mathrm{valley,(n-1)}}). \tag{6.6}$$

From these equations, the value of T_{start} does not need to be included since the relative times are already calculated. The length of the trap L_{trap} can then be used along with the diameter of the trap D_{trap} and the newly calculated T_{Rn} to find f_{Rn}. This is shown in Equation 6.7 and produces a value of flow in $\mathrm{m}^3/\mathrm{min}$.

$$f_{\mathrm{Rn}} = \frac{L_{\mathrm{trap}}\left(\frac{D_{\mathrm{trap}}}{2}\right)^2\pi}{T_{\mathrm{Rn}}} = \frac{V_{\mathrm{trap}}}{T_{\mathrm{Rn}}}[\mathrm{m}^3/\mathrm{min}]. \tag{6.7}$$

Given the dimensions of the trap highlighted in Chapter 5, $V_{\mathrm{Rn}} = 27.9$ mL $= 2.79\times10^{-5}$ m^3.

The retention time of radon within the trap will influence the size of future radon traps. If radon can stay in an extended trap for many half-lives, less radon will be re-emitted. This is beneficial for the NEWS-G detector, as it will allow the volume of the detector to be filled before any radon is re-emitted into the GHS. For example, if ^{222}Rn stays in the trap for 6 half-lives, only 1.56% of the original amount will remain after about 23 days.

6.1.3 Error Estimation

As mentioned in Chapter 5, the major source of error for the radon activity is the RAD7 statistical error. This is provided by the RAD7 and is measured as:

$$\delta N = 1 + \sqrt{N + 1} \tag{6.8}$$

where N is the number of counts recorded in a given time. In cycles with higher

counts, the addition of 1 to N becomes insignificant. For low counts the statistical error becomes significant and when no activity is recorded, the error is ± 4 counts/cycle. All of these values are adapted for only ^{222}Rn and converted to Bq.

The final element of error within the RAD7 originates from the background activity itself. Within the RAD7, low-activity materials are used to reduce this background, but they still contribute one count every two hours (0.15 mBq) as measured by DURRIDGE [105]. This indicates the sensitivity of the RAD7 and constitutes the minimum achievable sensitivity in the data.

As mentioned in Chapter 5, the BGA also has an error component to its data. Due to the precise speed of sound and temperature measurements, the largest source of error for the gas composition data is the statistical error. Since the BGA records data at about 3.5 Hz, the data can be averaged over ten measurements and the error is extracted from the standard deviation. This error is typically on the order of 1% of the concentration value.

6.2 Activated Charcoal Radon Adsorption

6.2.1 Room Temperature Testing

The first series of tests conducted with the Carboxen material occurred at RT, the ambient temperature of the Piro Lab. The measured RT stayed between 18°C and 24°C, as measured by the thermocouple attached to the exterior surface of the trap. The same analysis is applied for all three gases used (N_2, Ar, Ar+M) to measure the effects that the radon trap has on the activity of ^{222}Rn. To quantify this effect, three different values are extracted from the activity data, which are detailed in the following list.

1. **Time of Trap Opening** - The time the radon trap is opened is indicated by the vertical teal dashed line and denoted as t_0. It is also the time at which the initial activity A_0 is calculated, marked by a red dot.

2. **Stabilization Time** - This is the time where there are no longer large fluctuations of activity within the RTS. These fluctuations are damped oscillations from radon re-emission and re-adsorption whose extrema can be used to measure f_{Rn}. Stabilization time is represented by t_1 and marked by the yellow dashed line. From this value, the average activity $A_{\mathrm{f,avg}}$ window is determined and plotted as a solid red line.

3. **End Time** - The end time (t_2) is when the run has finished, which is marked by a red, dashed line. It is compared with t_1 to find the time in which the radon activity has no significant fluctuations.

The different times mentioned are summarized in a chart for each run, along with the values for A_0, $A_{\mathrm{f,avg}}$, and R.

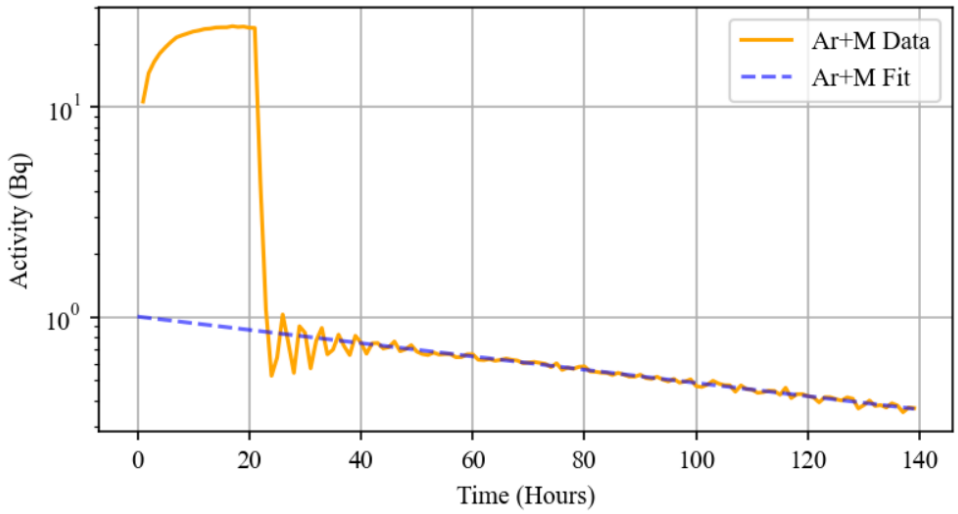

Figure 6.3: The Ar+M RT run with a fitted decaying exponential curve that indicates a half-life of 3.96 ± 0.07 days. The data was fit after the large fluctuations ended (close to 60 hours), and extended to the start time. The expected half-life of Rn^{222} is 3.82 days.

The 10-hour window was selected to find the value of $A_{f,\mathrm{avg}}$ based on the continual decay of non-trapped radon circulating in the RTS. As shown in Figure 6.3, the radon decay continues once the trap is opened and the activity has been stabilized. This decrease in activity has been fitted with a decaying exponential function which yields $t_{\frac{1}{2}} = 3.96 \pm 0.07$ days, which is very close to the expected half-life of 3.82 days for ^{222}Rn. During the 10-hour window used, the radon activity should decrease by only 7.3% by decay, which is smaller than the statistical uncertainty of the average.

Nitrogen

The first gas used for preliminary testing purposes was N_2. The following RT test was a proof-of-concept for the RTS and as a check whether the radon trapping material functioned as intended. Once the radon was injected into the circulation system, it was left for 22 hours before the radon trap was opened. As shown in Figure

6.4 at this time, the activity of radon rapidly decreases by close to two orders of magnitude.

Once the activity for the run was determined, the analysis mentioned in the previous section was applied, and is shown in Figure 6.4. This plot displays the activity in mBq for better comparison with the minimum sensitivity of the RAD7 (0.15 mBq). The various lines indicate different values that are found in the legend of the graph. Of note are the initial activity A_0 and the final average activity $A_{f,\text{avg}}$, which are used to calculate $R = 45 \pm 1$. All of the measured values are presented in Table 6.1.

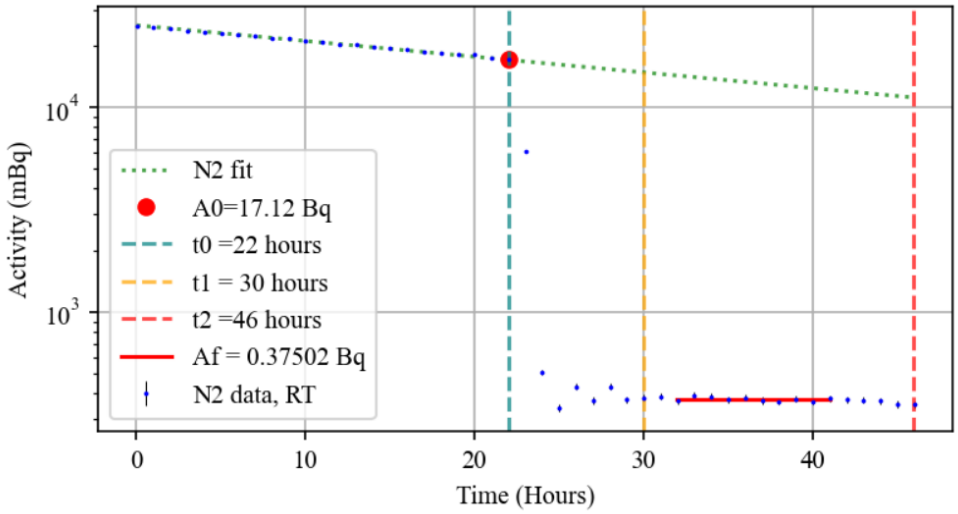

Figure 6.4: Activity of ^{222}Rn during the N_2 RT run using Carboxen with the included statistical error bars, zoning lines, and the fit of the initial activity (green dotted line).

A_0	t_0	t_1	t_2	$t_1 - t_0$	$A_{f,avg}$	R
17.12 Bq	22 h	30 h	46 h	8 h	0.38 ± 0.01 Bq	45 ± 1

Table 6.1: Values from the N_2 run using RT Carboxen.

From the analysis of this run, the R-value was found and can be compared to the value obtained from both the RT and DI temperature Carboxen runs. Much like the K-factor, this will also allow for a direct comparison between the silver zeolite and Carboxen runs. It was not possible to extract any meaningful value for f_{Rn} due to the limited extrema data available. When attempted, the error was several orders of magnitude higher than the value itself.

Argon

Following the same procedure as the previous section, the activity from the Ar RT run is shown in Figure 6.5. From the analysis, a value of $R = 53 \pm 2$ is calculated. This value is higher than the previous N_2 test and indicates a slightly better trapping performance. All of the numbers obtained from this analysis can be found in Table 6.2. This run additionally has large damped oscillations after the trap is opened that allow for extrema in the activity to be found, and f_{Rn} to be determined.

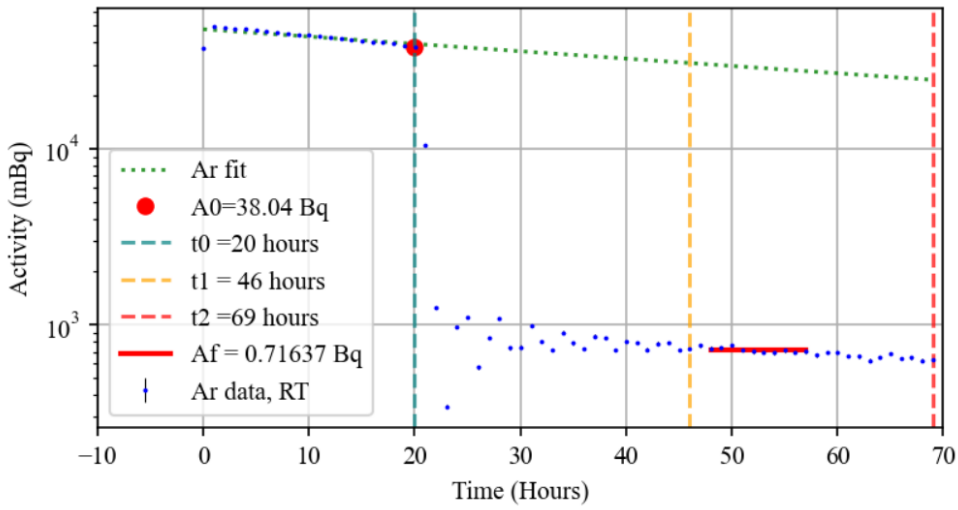

Figure 6.5: Activity of ^{222}Rn during the Ar RT run using Carboxen with the included statistical error bars, zoning lines, and the fit of the initial activity (green dotted line).

A_0	t_0	t_1	t_2	$t_1 - t_0$	$A_{f,\mathrm{avg}}$	R
38.04 Bq	20 h	46 h	69 h	26 h	0.72 ± 0.02 Bq	53 ± 2

Table 6.2: Values from the Ar run using RT Carboxen.

The cycle time for each data point presented in Figure 6.5 was one hour, meaning that activity is averaged across one hour. This cycle time decreases the resolution of points involving the oscillations and increases the uncertainty in the T_{Rn} value. With the use of the adapted calculation for T_{Rn}, this uncertainty can be reduced by including more hill-valley pairs, as described in Equation 6.4. The extrema values used are shown in Figure 6.6.

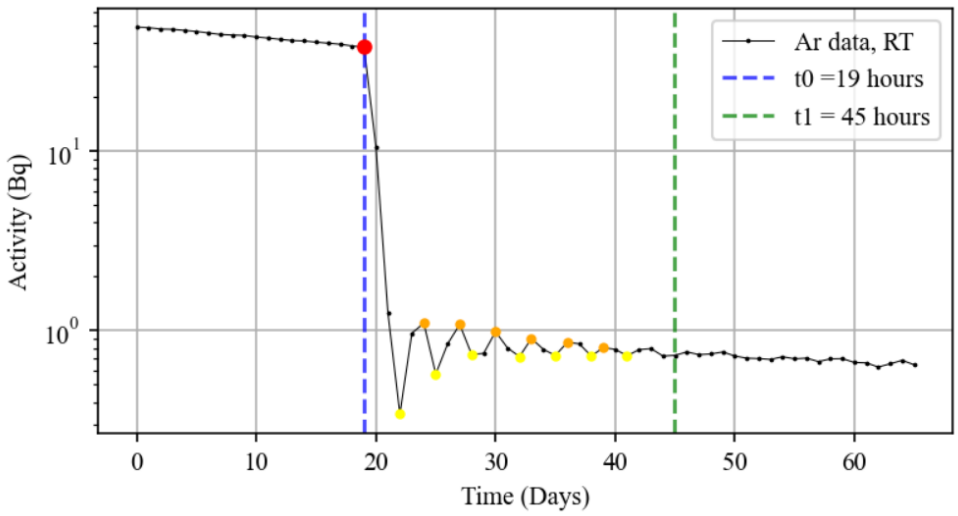

Figure 6.6: The extrema values for the damped oscillations of Ar in Carboxen at RT. The yellow points indicate local minima, while the orange points are for local maxima.

From these calculations, a value of $T_{\mathrm{Rn}} = 95 \pm 30$ minutes is found. The flow of radon through the trap is then calculated from Equation 6.7 as $f_{\mathrm{Rn}} = (1.17 \pm 3.8) \times 10^{-6}$ m^3/min. This rate can then be compared with other runs and used to determine an optimal length of the radon trap to prevent unwanted re-emission.

Argon-methane

The final run completed with the RT Carboxen material was with Ar+M. The calculated ^{222}Rn activity is shown in Figure 6.7, along with the significant values found in the analysis. Table 6.3 contains a summary of these values.

An important feature to note in Figure 6.7 is the difference in the initial activity (before the trap is open) when compared with N_2 and Ar. Here, the activity has a more gradual increase in activity at the beginning of the run compared to the pronounced jump in activity for the other two runs. Although all three runs underwent the same radon injection procedure, the RAD7 did not record the total activity for the Ar+M mixture, making it difficult to perform a decaying exponential fit of the initial activity. The addition of methane within the system is a probable cause for this behaviour, but further investigation is needed to understand the underlying mechanism.

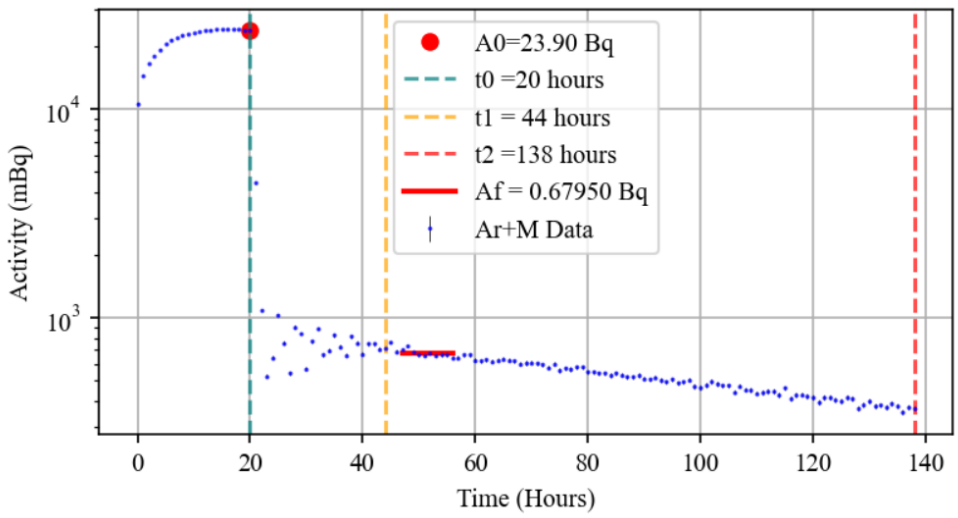

Figure 6.7: Activity of ^{222}Rn during the Ar+M RT run using Carboxen with the included statistical error bars and zoning lines.

A_0	t_0	t_1	t_2	$t_1 - t_0$	$A_{f,\text{avg}}$	R
23.90 Bq	20 h	44 h	138 h	24 h	0.68 ± 0.02 Bq	35 ± 1

Table 6.3: Values from the Ar+M run using RT Carboxen.

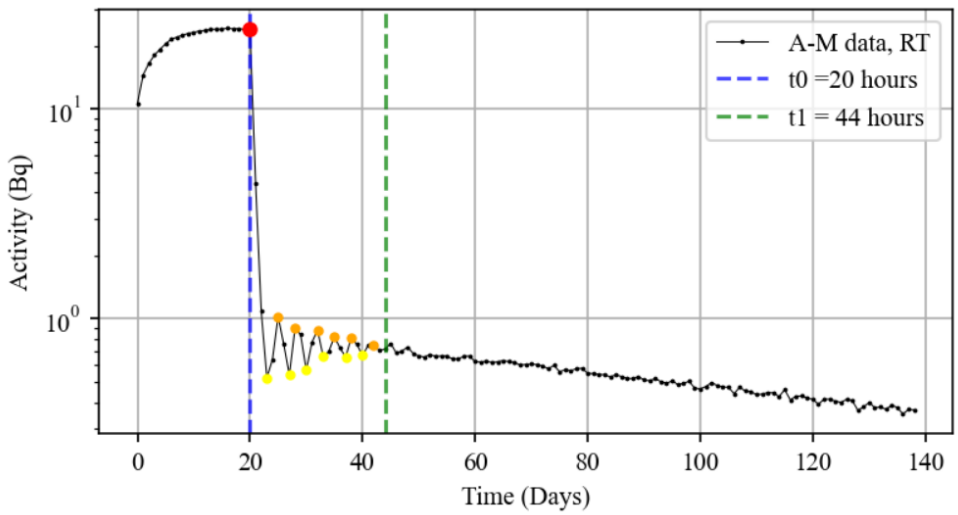

Figure 6.8: The extrema values for the damped oscillations of Ar+M in Carboxen at RT. The yellow points indicate local minima while the orange points are for local maxima.

The R-value obtained of 35 ± 1 is close to that of N_2 while being lower than that of Ar. From Figure 6.8, radon re-emission was observed with a value of $T_{\text{Rn}} =$

104 ± 27 minutes. Using this value in Equation 6.7, the flow of radon is found to be $f_{\mathrm{Rn}} = (1.08 \pm 4.2) \times 10^{-6}$ m^3/min. This is comparable to the value of f_{Rn} found for Ar, and the two values are within error of each other.

6.2.2 Room Temperature Results

The RT runs are plotted together in Figure 6.9 normalized to the A_0 value as a visual comparison of the radon adsorption. Also evident from this plot is the decay of the radon that continues to circulate through the RTS. The duration of the runs varies, but the R-values and flow rates are directly comparable. The results from all three runs at RT are summarized in Table 6.4, including the oscillation time ($t_1 - t_0$), initial activity (A_0), average final activity ($A_{f,\mathrm{avg}}$), R-value, and flow rate (f_{Rn}).

Gas	$t_1 - t_0$	A_0	$A_{f,\mathrm{avg}}$	R	f_{Rn}
N_2	8 h	17.12 Bq	0.38 ± 0.01 Bq	45 ± 1	NA
Ar	26 h	38.04 Bq	0.72 ± 0.02 Bq	53 ± 2	$(1.17 \pm 3.8) \times 10^{-6}$ m^3/min
Ar+M	24 h	23.90 Bq	0.68 ± 0.02 Bq	35 ± 1	$(1.08 \pm 4.2) \times 10^{-6}$ m^3/min

Table 6.4: Comparison of the different values obtained for each gas using RT Carboxen.

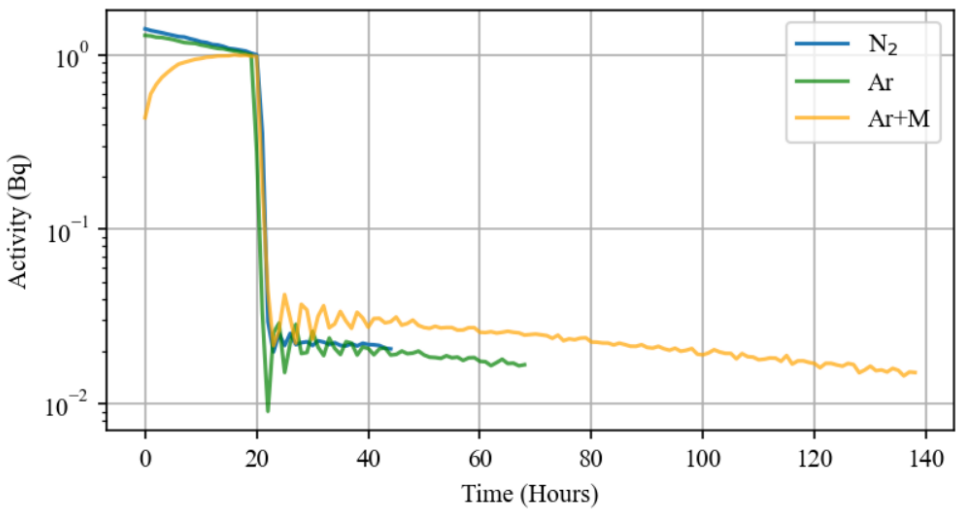

Figure 6.9: A comparison of all RT Carboxen runs normalized to A_0.

From the values presented in Table 6.4, the R-value for each gas is on the same order of magnitude when using the RT Carboxen. Although the R-value for Ar is

around 20% higher than for N_2 and Ar+M, the radon adsorption of this material is not significantly dependent on the species of gas.

The values found for f_{Rn} are within the range of error of each other, indicating that the species of gas does not affect the movement of radon within the trap. The study conducted by Abe *et al.* found that the flow rate of radon through the trap is dependent on the length (and therefore volume) of the trap as well as the flow rate of the primary gas. Given that the runs discussed above used the same 1 L/min pump and a consistent trap size, the results do not contradict Abe *et al.* when different gas species are used. These results also show that methane does not have a significant impact on the flow of the Carboxen radon trap at RT.

6.2.3 Dry Ice Temperature Testing

The experimental setup differs slightly for the DI radon trap in that it must be cooled. To effectively surround the trap in DI, a polystyrene container was constructed. Several iterations of this box were used, with the general trend geared towards a larger box for better trap coverage and longer times between refills. The frequency of refills also changed, but the trap was filled a minimum of once every 12 hours. These times were selected to ensure that the level of dry ice in its container did not go below the top of the radon trap. A 12 hour cycle was initially used before being switched to an 8 hour cycle to prevent larger fluctuations in the temperature between refills. An image of the RTS with the polystyrene box is shown in Figure 6.10. The temperature of the trap was monitored using a thermocouple device and manually recorded. The temperatures presented in the coming sections are averaged along with the standard deviation. Overall the frequent refilling aided in keeping the low temperature stable over time.

The analysis for the tests using DI tests varies from the RT tests. The re-emission of radon from the trap takes a significantly longer time (days compared to minutes) and the period in which radon is re-emitted must be defined. To do so, the time t_2 now indicates the start of the radon re-emission, while the new time t_3 (black, dashed line) denotes the end of the re-emission. The time of radon re-emission is then defined as

$$T_r = t_3 - t_2. \tag{6.9}$$

Another value that must be introduced when analyzing the DI runs is the total re-emission activity $A_{r,\text{tot}}$. This is the total activity re-emitted from the trap during the re-emission time and can be used to determine the quantity of radon that was released from the trap.

Figure 6.10: The cooling system for the radon trap is a customized polystyrene box capable of holding 4.5 kg of dry ice pellets.

For the analysis of these DI temperature runs, the background activity of the RAD7 must be considered. Since the minimum achievable activity of the RAD7 is 0.15 mBq, any values with a recorded value of 0 Bq are replaced with this minimum activity value. This sets a baseline that is necessary for proper analysis of the DI temperature runs. This type of adjustment is not necessary for the RT tests since there were no instances of no activity being measured.

Nitrogen

N_2 was once again used for the first DI test to ensure that the RTS operated as expected under colder conditions. The activity of ^{222}Rn is shown in Figure 6.11. The same analysis as discussed in Section 6.2.1 is used, including the changes made to t_2 and the addition of t_3.

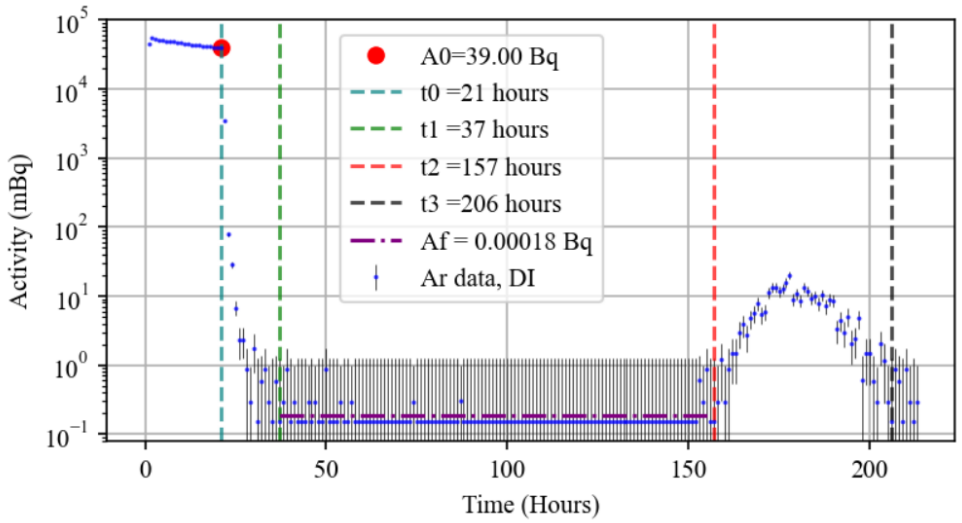

Figure 6.11: Activity of ^{222}Rn during the N_2 DI run using Carboxen with the included statistical error bars and zoning lines.

The values calculated from Figure 6.11 are presented in Table 6.5. In this instance, the $R = (2.13 \pm 0.87) \times 10^5$ is significantly higher than any of the RT runs, demonstrating the effectiveness of cooling the Carboxen. In these data, opening the trap decreases the radon activity by five orders of magnitude, and the lower sensitivity threshold of the RAD7 is reached at 0.15 mBq. Since radon decay cannot be measured below this threshold, the average activity could be calculated between t_1 and t_2 instead of using the same 10-hour window as the RT runs. The average trap temperature for this run was (-81.1 ± 5.1)°C, as measured by the exterior thermocouple.

A_0 (Bq)	t_0	t_1	t_2	t_3	$t_1 - t_0$	$t_3 - t_2$	$A_{f,\text{avg}}$ (Bq)	R
39.00	21	37	157	206	16	49	$(1.8 \pm 1.2) \times 10^{-4}$ Bq	$(2.13 \pm 0.87) \times 10^5$

Table 6.5: Values for the N_2 run using DI temperature Carboxen. Time values (t_n) are in hours.

The notable re-emission in Figure 6.11 between the red and black vertical lines has a $T_r = 49$ hours and a total activity of $A_{r,\text{tot}} = 0.29$ Bq. These values will set a baseline for comparison with other observed re-emission peaks. The value of $A_{r,\text{tot}}$ is three orders of magnitude above the $A_{f,\text{avg}}$-value. Should a radon re-emission occur in a similar radon trap connected to a NEWS-G detector while being filled, the alpha events would dramatically increase. Therefore, it is important to define

the optimal window of minimal activity in which gas can safely be injected into the detector.

Argon

The same procedure from the N_2 test was applied for the Ar gas circulating with the Carboxen trap at DI temperature. The activity after radon injection is shown in Figure 6.12 and is once again significantly lower once the trap is opened when compared to its RT equivalent. The zoning method is also used in Figure 6.12, with the results summarized in Table 6.6. The trap was held at a temperature of $(-82.6 \pm 4.7)°C$.

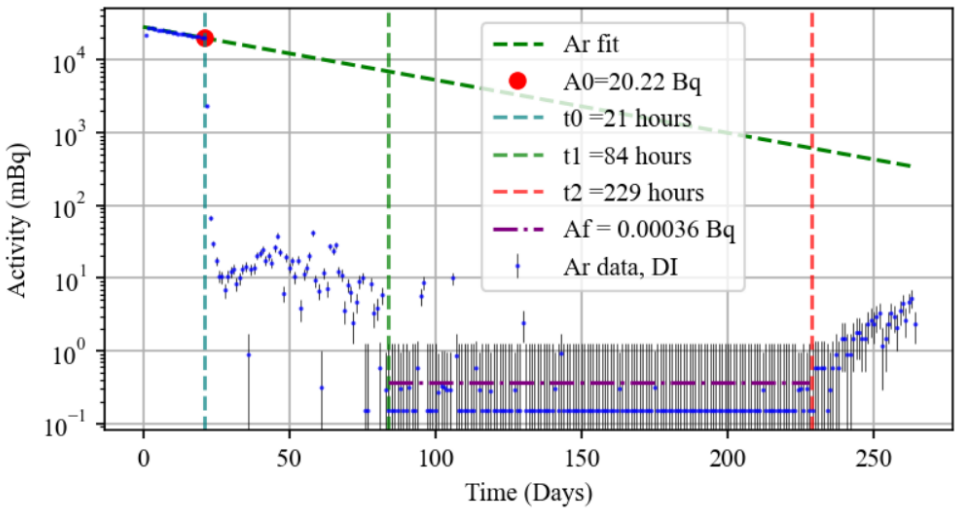

Figure 6.12: Activity of ^{222}Rn during the Ar DI run using Carboxen with the included statistical error bars and zoning lines.

As can be seen in Figure 6.12, the stabilization time $(t_1 - t_0)$ of this run is much longer than with other gases at DI temperature (64 hours compared to 16 hours in N_2). The reason for this effect is not known, but repeat tests could be conducted to determine if this is an effect from the Ar gas.

A_0 (Bq)	t_0	t_1	t_2	t_3	$t_1 - t_0$	$t_3 - t_2$	$A_{f,\text{avg}}$ (Bq)	R
20.22	21	84	229	NA	63	NA	$(3.6 \pm 1.2) \times 10^{-4}$	$(5.55 \pm 4.24) \times 10^4$

Table 6.6: Values for the Ar run using DI temperature Carboxen. Time values (t_n) are in hours.

The R-value for this run is determined to be $R = (5.55 \pm 4.24) \times 10^4$, which

is an order of magnitude lower than the one found for the N_2 DI test. This may hint at subtle differences for the adsorption of radon in Carboxen between N_2 and Ar that only become apparent at lower temperatures and activities. Something to note is that within the stabilization time, the peak value achieved once the trap was opened is on the same order of magnitude as the re-emission peaks from other DI temperature runs. No conclusions can be made about this longer stabilization period and more tests are required to investigate the cause of this behaviour.

Argon-methane

The final gas that utilized the Carboxen at DI temperature is the Ar+M gas mixture. The results from this test are important for the NEWS-G experiment since a similar gas composition will be used in the SNOLAB installation. The ^{222}Rn activity is shown in Figure 6.13, along with results from the zoning method. The relevant values were extracted and presented in Table 6.7. The average temperature of the radon trap was (-75.3 ± 3.8)°C.

The results from this test yield a value of $R = (8.14 \pm 4.31) \times 10^4$, which is also an order of magnitude lower than with the N_2 DI run. This is also closer to the R-value for Ar, indicating that the adsorption of radon with Carboxen may have a dependence on the gas species. The re-emission of radon from the trap lasted for $T_r = 56$ hours, during which the total re-emitted activity was $A_{r,\text{tot}} = 0.38$ Bq. Both values are similar to those obtained in the N_2 DI run. This again highlights the importance of finding the optimal window for gas injection by using the value of $t_2 - t_1$. It is noted that the stabilization time for this run was significantly longer than for the N_2 DI test and future tests are needed to understand the effect argon may have on initial radon adsorption.

When the radon was injected into the system, the activity of the radon did not reach a maximum like with N_2 and Ar, instead gradually increasing similarly to the Ar+M RT run. This provides further evidence that methane is affecting the measurement of radon in the RAD7 and future investigations may yield interesting results.

A second test under the same conditions was run to check the repeatability of the results from this run. Due to issues with the RAD7, leaks introduced a higher concentration of radon into the system from the surrounding environment, compromising the data taken within the run. The overall radon background after the trap was opened produced an average activity an order of magnitude higher

than the previous DI runs. Due to time constraints, it was not possible to repeat this test, but this highlights the importance of ensuring that components like the RAD7 are leak-tight for working with a system like the RTS.

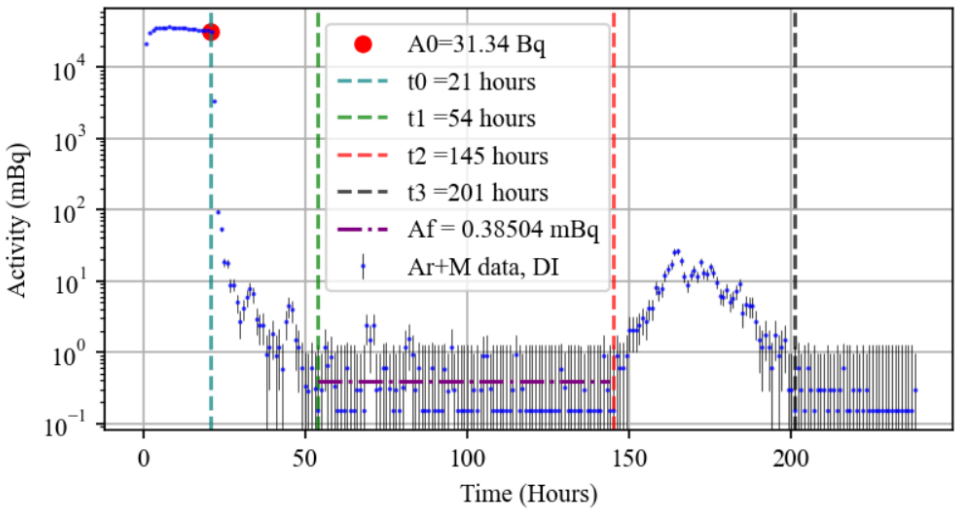

Figure 6.13: Activity of ^{222}Rn during the Ar+M DI run using Carboxen with the included statistical error bars and zoning lines.

A_0 (Bq)	t_0	t_1	t_2	t_3	$t_1 - t_0$	$t_2 - t_1$	$A_{f,\text{avg}}$ (Bq)	R
31.34	21	54	145	201	33	91	$(3.9 \pm 4.3) \times 10^{-4}$	$(8.14 \pm 4.31) \times 10^4$

Table 6.7: Values for the Ar+M run using DI temperature Carboxen. Time values (t_n) are in hours.

6.2.4 Dry Ice Temperature Results

The results from all of the DI temperature runs have been compiled in Table 6.8, and a comparison plot of the three separate runs is shown in Figure 6.14. Compared to the RT plot of the same nature, the activities do not need to be normalized since they all contain the minimum recording of activity from the RAD7. Overall, the performance of the DI temperature trap is vastly superior to that of the RT trap by three orders of magnitude. This confirms the performance of activated charcoal traps tested previously and indicates that a colder trap will be better for the NEWS-G detector.

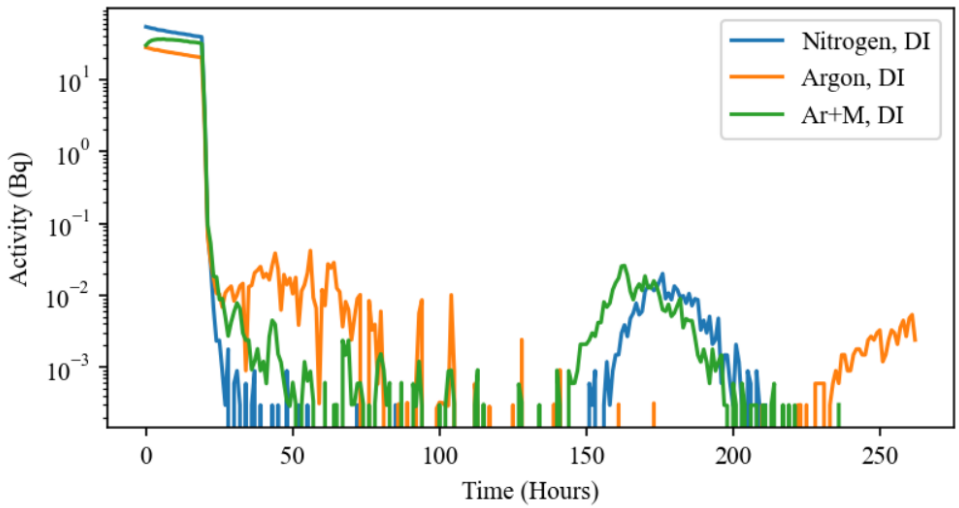

Figure 6.14: A comparison of the activity for each of the gases with the DI temperature Carboxen trap.

Gas	A_0	$A_{f,\text{avg}}$	R	Re-emission Window
N_2	39.00 Bq	$(1.8 \pm 1.2) \times 10^{-4}$ Bq	$(2.13 \pm 0.87) \times 10^{5}$	49 h
Ar	20.22 Bq	$(3.6 \pm 1.2) \times 10^{-4}$ Bq	$(5.55 \pm 4.24) \times 10^{4}$	NA
Ar+M	31.34 Bq	$(3.9 \pm 4.3) \times 10^{-4}$ Bq	$(8.14 \pm 4.31) \times 10^{4}$	56 h

Table 6.8: Notable values obtained for each gas from the DI temperature Carboxen runs.

By comparing the R-values, it is clear that radon was better adsorbed when N_2 was used as the carrier gas, which also had the shortest stabilization time. Given that the other two gases contain argon, this may hint at subtle effects that the gas species can have on radon adsorption. Such effects have been previously observed as shown in Figure 6.15, in which the radon adsorption is measured by the K-factor.

From the study conducted, it is suggested that there is competition for adhesion between radon and its carrier gas. The gas CF_4 has a similar radius to radon ($r_{\text{Rn}} = 100$ pm versus $r_{\text{CF}_4} = 107$ pm) resulting in strong competition between the two gas particles, and less radon getting adsorbed. While CF_4 was not used in the study I conducted, it does demonstrate the effect of carrier gases on radon adsorption. Argon also has a similar radius to radon ($r_{\text{Ar}} = 97$ pm), which may explain the decrease in R-value when compared to the N_2 ($r_{\text{N}_2} = 75$ pm) DI run. Further tests are needed to confirm this effect, and different gases and gas mixtures can be used.

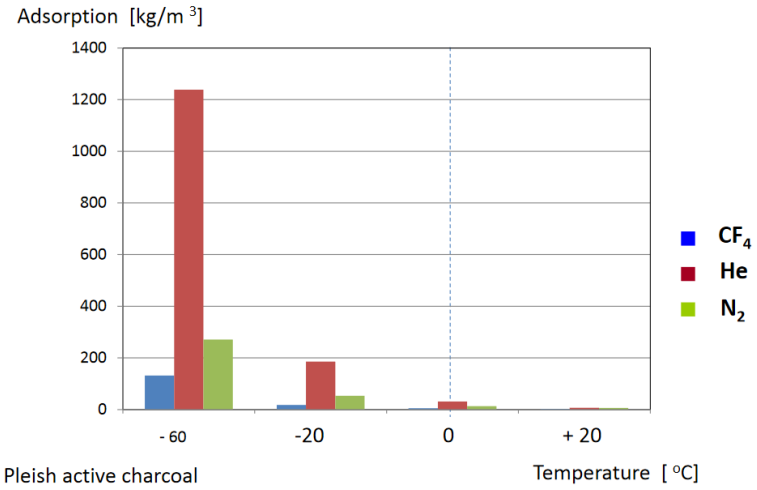

Figure 6.15: A comparison of the radon adsorption in Pleish [*sic*] active charcoal using different gases at different temperatures [106]. The Pleisch Company is another manufacturer of activated charcoal.

The addition of methane into argon produces an R-value experiences a jump of 47% compared to pure argon. While the influence of methane on the adsorption of radon can be better studied through repeat testing, the adsorption of methane at DI temperature with Carboxen is discussed in Section 6.4.

As mentioned with the Ar+M DI test, a repeat of these tests could not be conducted due to both laboratory constraints, time restraints, and leaks present within the system. It is noted that all of the tests presented in this thesis were completed without leaks, unless otherwise mentioned. More useful data can be collected from similar tests to confirm several of the results discussed above. An important test is to allow the RTS to run for longer times at DI temperatures. This longer run would allow for a potential second re-emission peak to be observed, allowing for a calculation for f_{Rn} in Carboxen.

6.3 Silver Zeolite Radon Adsorption

The other trapping material used in the RTS was silver zeolite produced by Extraordinary Adsorbents in Edmonton, Alberta. This is a new material being investigated for the NEWS-G experiment for radon mitigation. It has been tested with xenon as the carrier gas, but not with methane [102]. The following tests explore radon adsorption using the Ar+M gas mixture at RT and DI temperatures.

6.3.1 Room Temperature Test

The RT test used the same procedure and trap size as the Carboxen tests, with the only difference being the alternate trapping material. For the RT test, only Ar+M was used due to time restraints and the relevance of this gas mixture to the NEWS-G experiment. The activity recorded by the RAD7 is shown in Figure 6.16, along with the zones, A_0, and A_{favg}.

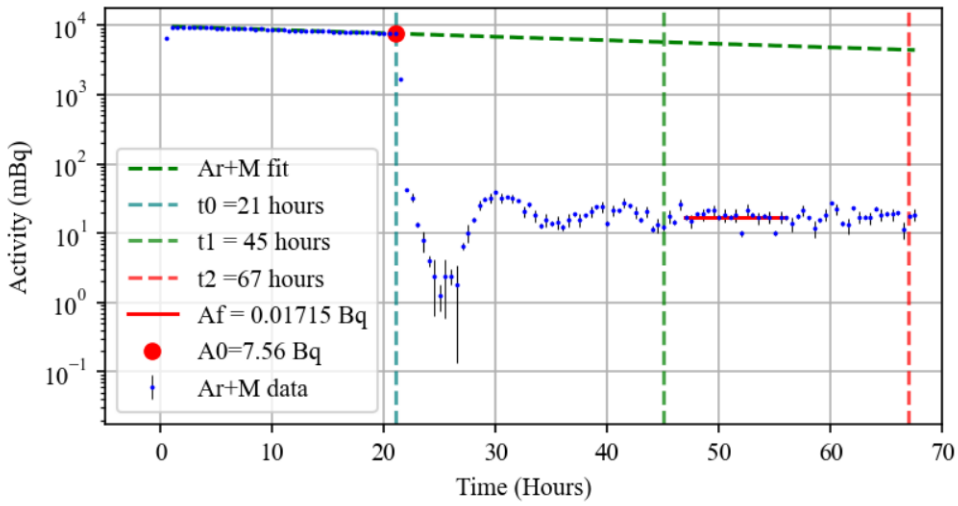

Figure 6.16: The ^{222}Rn activity with circulated Ar+M through the silver zeolite trap at RT.

A_0	t_0	t_1	t_2	$t_2 - t_1$	$A_{f,\text{avg}}$	R
7.56 Bq	21 h	45 h	67 h	32 h	$(1.7 \pm 0.4) \times 10^{-2}$ Bq	$(4.40 \pm 0.90) \times 10^2$

Table 6.9: Values for the Ar+M run using RT silver zeolite.

The R-value calculated for the silver zeolite shown in Table 6.9 is significantly higher than the RT runs using Carboxen by an order of magnitude. This indicates an overall better performance with more radon being adsorbed.

Since there are fewer significant activity extrema in these data when compared to the RT runs, the same method of finding T_{Rn} as in Abe *et al.* has been followed. In this case, only the extrema values for the first valley and hill are found, as shown in Figure 6.17 resulting in $T_{\text{Rn}} = 390 \pm 7$ min. The value calculated using Equation 6.7 is $f_{\text{Rn}} = (2.85 \pm 0.01) \times 10^{-7}$ m^3/min. When compared to the Carboxen RT runs, this value is also an order of magnitude lower, which demonstrates the better performance of this trapping material.

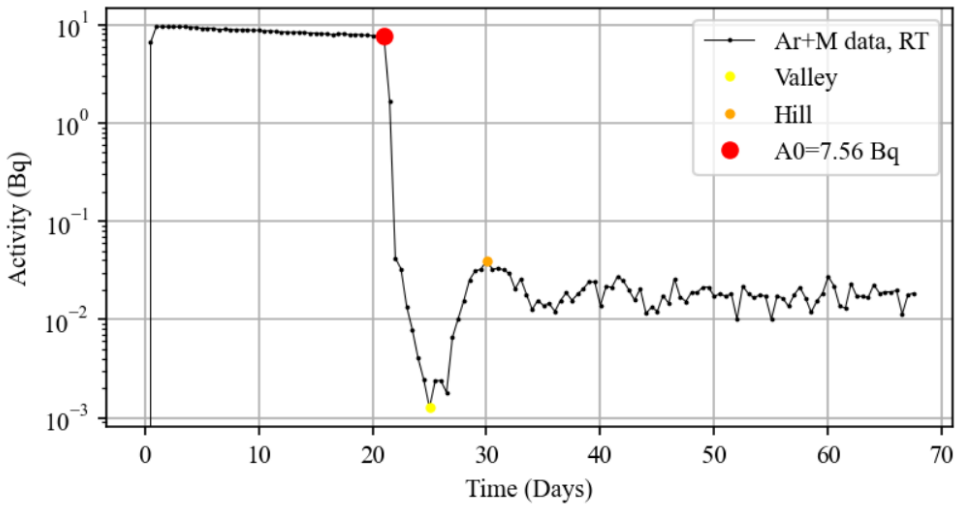

Figure 6.17: The hill and valley points used to calculate the value for f_{Rn} in silver zeolite at RT using an Ar+M mixture.

6.3.2 Dry Ice Temperature Test

A run using DI temperatures silver zeolite was performed to compare it to the Carboxen run under the same conditions. As with the RT silver zeolite run, the Ar+M mixture was used in circulation. The resulting activity from this test is shown in Figure 6.18, along with the appropriate zones and their corresponding values. Also shown in this plot is a fitted curve of the intial ^{222}Rn decay, along with a re-emission that occurred from the trap being regenerated towards the end of the test. The temperature of the trap exterior for this test was (-81.0 ± 3.7)°C.

Much like the DI temperatures tests with Carboxen, there is a significant decrease in radon activity once the trap is open. The stabilization time is 24 hours, which is closer to that of the N_2 DI run in Carboxen than the Ar+M DI run.

As shown in Table 6.10, the calculated R-value is comparable in magnitude to that of the other two DI runs involving Ar. Here the performance is slightly less than all of the previous DI runs. This indicates that not all of the radon is being trapped within the silver zeolite or that the background activity is higher. Due to the similarities in the values for $A_{f,\mathrm{avg}}$ for all of the DI runs ($\sim 10^{-4}$ Bq), repeats of these tests using a more sensitive radon detector are recommended.

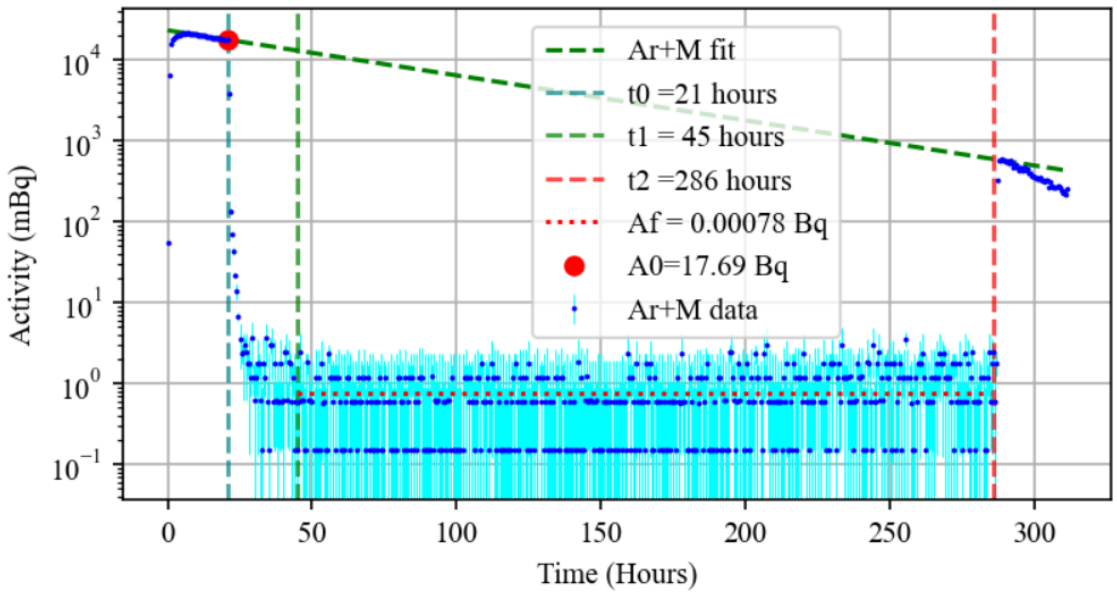

Figure 6.18: Activity of ^{222}Rn during the Ar+M DI run using silver zeolite with the zoning lines. The calculated statistical error bars are shown in cyan.

A_0	t_0	t_1	t_2	$t_2 - t_1$	$A_{f,\text{avg}}$	R
17.69 Bq	21 h	45 h	286 h	241 h	$(7.8 \pm 6.3) \times 10^{-4}$ Bq	$(2.27 \pm 1.02) \times 10^4$

Table 6.10: Values for the Ar+M run using DI temperature silver zeolite.

No natural re-emission occurred throughout the span of the test, but the radon trap was regenerated by being heated to 160°C for 20 minutes. During this period of radon re-emission the activity returned to the expected level based on the fit of the initial activity. This demonstrates that the radon was adsorbed by the silver zeolite and not lost through other means during this run. During the re-emission at the end of the run, the radon decay slope is more negative than the expected decay rate from the fit. This implies the potential presence of a leak after the trap was regenerated. Time constraints led to this test being stopped just after 300 hours, but it is recommended to repeat this test for a longer period to confirm if radon re-emission occurs in a way similar to the Carboxen material. A longer term test with multiple re-emission peaks would allow for a calculation of f_{Rn} for silver zeolite at this temperature.

6.4 Activated Charcoal Methane Adsorption

The first occasion where the effects of a loss of methane were observed came from a run of a 30 cm diameter SPC at Queen's University. The NEWS-G detector is sensitive to the concentration of methane, and it was noticed that the signal produced correlated with a decreased methane concentration over time as gas was circulated. While the cause of the methane loss was not investigated, it was suspected that the radon trap material was also adsorbing methane.

When testing the methane adsorption with the Carboxen material, the RAD7 was removed from the system and an external diaphragm pump with the same flow rate (1 L/min) was used. This was done to avoid leaks from the RAD7, while still allowing circulation in the RTS.

6.4.1 Room Temperature Test

The first test conducted to measure the adsorption of methane utilized the Ar+M gas mixture at RT. Using the BGA, the relative methane concentration in argon can be measured and monitored during the entire run with computer software. The Ar+M gas was first allowed to circulate for a 24 hours so the initial concentration of methane could be determined. The system stability could also be checked at this point to ensure that no leaks were present. The radon trap was then opened for 24 hours, followed by it being heated and closed. This procedure provided information about how much methane is adsorbed by the Carboxen at RT and if the adsorbed methane could be recollected by regenerating the trap.

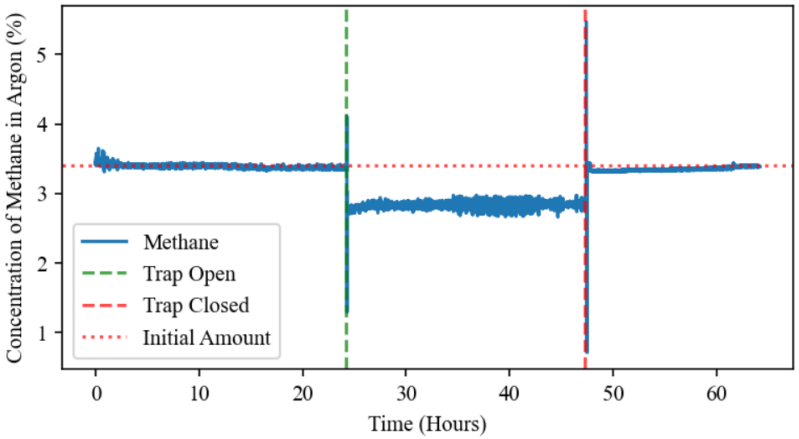

Figure 6.19: Relative concentration of methane in argon with the opening, heating, and closing of the Carboxen trap.

The concentration is measured as a percentage, and the amount of methane in argon is presented in Figure 6.19. From these data, the average initial concentration is $3.38 \pm 0.03\%$. Once the trap is opened, the concentration of methane drops to $2.83 \pm 0.06\%$. After heating and closing the trap the methane concentration returns to $3.34 \pm 0.09\%$, indicating that any methane adsorbed is re-emitted when the trap is regenerated. This method concludes that methane was removed from circulation by the Carboxen. The remainder of the test demonstrates that there were no leaks within the RTS, validating this result.

6.4.2 Dry Ice Temperature Test

The same procedure was applied to test the adsorption of methane in Carboxen at DI temperatures. Figure 6.20 shows the concentration of methane in argon before and after the radon trap is open. While the small peaks and dips in the data correspond to the DI reservoir being refilled, the overall upward trend is indicative of a small leak within the RTS. Through the process of DI sublimation and refilling, variances in the temperature of the trapping material occur, altering its adsorption capabilities.

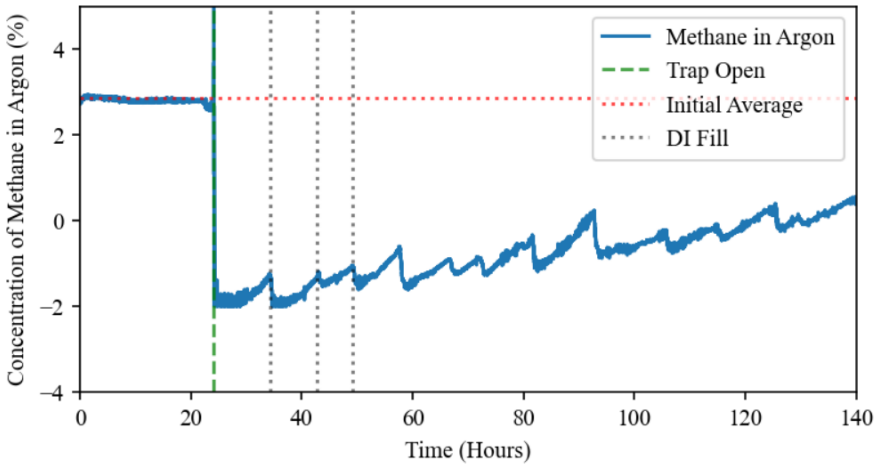

Figure 6.20: The concentration of methane as a function of time while using a DI temperatures Carboxen radon trap. The black, vertical, dotted lines indicate the times in which the DI was refilled, and filling corresponds to a local maxima, followed by an immediate drop.

The initial average concentration of methane circulating in the trap was found to be $2.82 \pm 0.04\%$. Once the trap was opened, the concentration drops to a value of $-1.90 \pm 0.11\%$. Given that it is physically impossible to have a negative ratio

between the concentration of two gases, this most likely corresponds to a drop in pressure when the cold radon trap was opened to the RTS. Since the BGA is sensitive to changes in pressure and no pressure monitoring system was used for this test, it is likely that the change in pressure would produce a shifted readout.

When focusing on the concentration immediately following the opening of the radon trap, a pattern of methane re-emission is evident. A window of three hours is shown in Figure 6.21 with various peaks. Using a peak-finding algorithm created for this analysis, it was found they are consistently periodic, with a period $T_{CH_4} = 41.16 \pm 0.05$ minutes. The flow rate of methane within the radon trap can then be calculated using Equation 6.7 and is found to be $f_{CH_4} = (5.416 \pm 0.004) \times 10^{-6}$ m^3/min. Since the re-emission of methane occurs every 41 minutes compared to the days that it takes for radon to re-emit at DI temperature, it can be concluded that the methane has a significantly higher flow rate than radon in Carboxen.

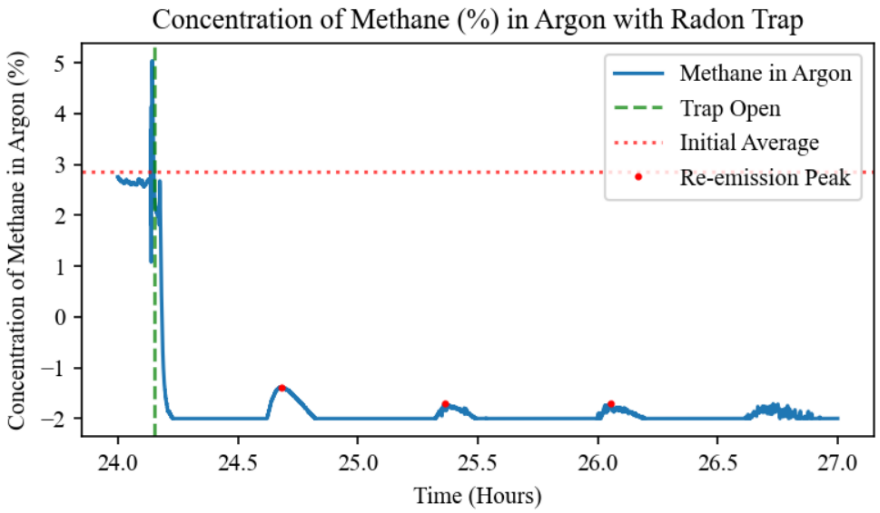

Figure 6.21: A three hour window surrounding the opening of the radon trap at in Carboxen at DI temperatures. The re-emission peaks are indicated with red dots.

Due to time restraints, the adsorption of methane in silver zeolite could not be studied and it is recommended to run such tests. Another constraint in these tests was a lack of a pressure sensor for the BGA, which would allow the device to account for sudden changes in pressure like when the cold trap is opened to the RTS.

6.5 Discussion

Through testing different radon trap configurations and parameters, the data obtained provides useful information about the ideal configuration for a radon trap to be used with the NEWS-G detector. The important parameters from these tests are summarized in Table 6.11, including the important R-value. This value was defined so that different gases, trapping materials, and temperatures could be directly compared on a unitless scale. In essence, the higher this value is, the better a material is at adsorbing a known quantity of radon in a closed circulation system.

Gas	Temp.	A_0 (Bq)	$A_{f,\text{avg}}$ (Bq)	R	f_{Rn} (m^3/min)
N_2	RT	17.12	0.38 ± 0.01	45 ± 1	NA
Ar	RT	38.04	0.72 ± 0.02	53 ± 2	$(1.17 \pm 3.8) \times 10^{-6}$
Ar+M	RT	23.90	0.68 ± 0.02	35 ± 1	$(1.08 \pm 3.8) \times 10^{-6}$
N_2	DI	39.00	$(1.8 \pm 1.2) \times 10^{-4}$	$(2.13 \pm 0.87) \times 10^{5}$	NA
Ar	DI	20.22	$(3.6 \pm 1.2) \times 10^{-4}$	$(5.55 \pm 4.24) \times 10^{4}$	NA
Ar+M	DI	31.34	$(3.9 \pm 4.3) \times 10^{-4}$	$(8.14 \pm 4.31) \times 10^{4}$	NA
Ar+M (SZ)	RT	7.56	$(1.7 \pm 0.4) \times 10^{-2}$	$(4.41 \pm 0.90) \times 10^{2}$	$(2.85 \pm 0.01) \times 10^{-7}$
Ar+M (SZ)	DI	17.69	$(7.8 \pm 6.3) \times 10^{-4}$	$(2.27 \pm 1.02) \times 10^{4}$	NA

Table 6.11: The significant values for RT and DI temperatures runs using Carboxen and silver zeolite. The silver zeolite runs are identified with (SZ).

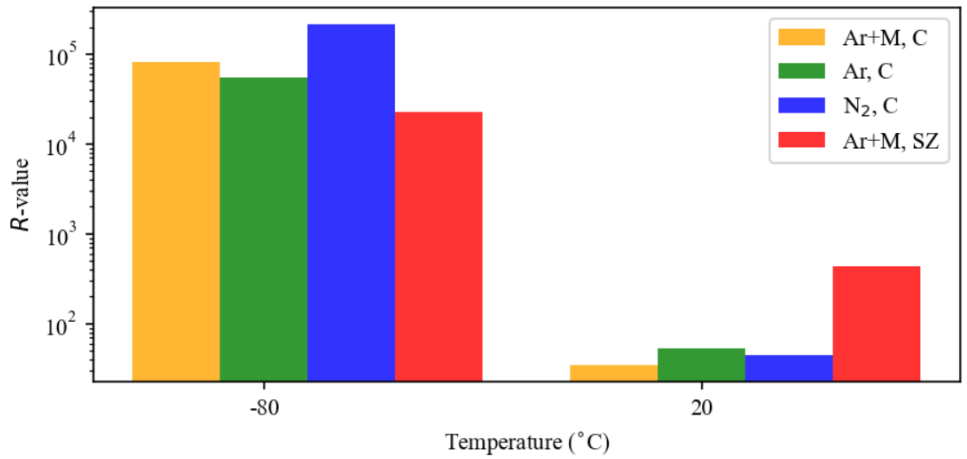

Figure 6.22: The various R-values for the three gases used at RT and DI temperature along with the two different trapping materials (C for Carboxen and SZ for silver zeolite).

The various R-values have been plotted as shown in Figure 6.22 as a direct comparison between all tests. From these results, it is clear that the optimum configuration is a DI temperature trap with nitrogen acting as the carrier gas. However,

the values for $A_{f,\text{avg}}$ are all on the same order of magnitude (10^{-4} Bq), indicating potential limitations in the sensitivity of the RAD7 and the existence of background activity from the RTS.

For future tests, a different method of cooling is recommended. Due to the variability in the DI level between fillings of the surrounding polystyrene trap, the trapping material experienced temperature fluctuations. By keeping the trapping material at a consistent and accurate temperature, any variation in radon activity, as a result, could be mitigated. A method capable of varying the temperature would also be useful in examining trends in adsorption as the temperature of the material changes. It is also recommended to continuously monitor the trap temperature through the use of a thermocouple and integrated computer software. For the previous tests presented, the temperature was recorded manually from the thermocouple readout.

A major setback throughout the use of the RTS was the presence of leaks within the RAD7. Since most connections within the RTS were stainless steel and from the same manufacturer (Swagelok), leaks were limited and easily sourced from the beginning using a helium leak detector. The vinyl tubing that was used to connect the RAD7 to the RTS along with the internal connections of the RAD7 posed issues. Leaks could be eliminated from the RAD7 but would be found after several completed tests. While the cause of these leaks is unknown, it is something to be mindful of in future tests involving a RAD7 device. The RAD7 also has limitations in terms of its sensitivity. Given that the device has a minimum achievable activity of 0.15 mBq, a more sensitive device would be preferred for further testing of highly adsorbent materials.

As mentioned previously, the molecular/atomic size of the carrier gas has been shown to affect the radon adsorption in activated charcoal. While repeat testing is required with the gases used in this test, there are notable differences between the N_2 DI temperature run and the DI temperature runs containing Ar and Ar+M.

6.5.1 Radon Trapping for NEWS-G

The development of a radon mitigation system for the NEWS-G detector is at the forefront of this testing. Several conclusions from these experiments can be made concerning the implementation of this system.

The first conclusion is the temperature of the trapping material used. In both

Carboxen and silver zeolite, the trapping of radon at DI temperature increased several orders of magnitude when compared to the RT runs. This has been shown in numerous other experiments and should be applied to the NEWS-G radon trap. It is, however, not recommended to use DI as the coolant method due to the need for frequent supervision and the variability in trap temperature. Instead, a more hands-off approach is recommended in the form of a refrigeration unit. Another possibility for cooling is the use of a liquid nitrogen-containing vessel along with a heating element around the trap to control the temperature. Regardless of the method of cooling, the trap should be maintained at a constant temperature. Further studies into operating the radon trap at lower temperatures are recommended.

The silver zeolite performs better than Carboxen at RT based on the R-value, but limitations with the RAD7 makes the distinction between these two materials at DI temperatures difficult. Due to the lack of radon adsorption testing with silver zeolite, more testing should be completed. A device with a lower minimum activity threshold is recommended for better measurements of the performance of these materials.

One such sensitive device that may work well is an SPC. At the Piro Lab, a 30 cm diamter SPC prototype (UofA SPC) is being commissioned to carry out various tests. Alpha particles can be identified from the output of this detector, and proper calibration may allow it to distinguish between alpha decay energies. Another benefit of using the spherical detector is that there is no vinyl tubing; the prototype uses the same stainless steel connections as the RTS. The UofA SPC was originally planned to be integrated with the RTS, but time constraints due to the COVID-19 pandemic delayed this operation significantly.

Due to radon re-emission at low temperatures, it is recommended that any circulating gas be injected into the detector after the Stabilization Time but before the re-emission of the radon. Based on the volume of the NEWS-G detector being about 1436 L, then a pump flowing at 1 L/min will be able to fill the sphere in just under 24 hours. Every DI temperature run could easily accommodate this time window.

Strong evidence for the trapping of methane was found in these tests. Considering the adsorption of methane and the sensitivity of the NEWS-G experiment to methane concentration, a device monitoring its amount is needed. The BGA has proven very useful in providing accurate methane measurements in a binary gas but

is affected by sudden changes in the temperature and pressure. A new methane monitoring system that utilizes laser spectroscopy is being developed in the Piro Lab. An investigation concerning methane adsorption in silver zeolite could not be conducted and further tests are recommended to characterize and estimate its potential effects.

Chapter 7

Conclusion

Through observations of galactic rotation curves, gravitational lensing, and CMB anisotropies, the invisible mass that makes up 27% of the universe has been well studied, but a DM particle continues to elude discovery. Many experiments are being conducted globally in an effort to search for this particle with the NEWS-G collaboration among them. The NEWS-G SPC is aimed at reaching previously unseen sensitivities to probe the extent of a potential low-mass (1 GeV/c^2) WIMP. To do so, many components must come together to create a detector that is ideal for the detection of DM. The two major components of this thesis describe very different, but important, aspects of the SPC detector to provide optimal conditions and analysis.

The development of optimal processing parameters for the QUADIS software discussed in Chapter 4 introduce the importance of accurate data representation when analyzing the data. Through proper calibration, the response of the SPC to a new event such as a WIMP nuclear recoil can be well characterized. For any data to be collected with the intention of detecting a WIMP passing through the volume of the detector the background activity must be reduced. A method to reduce the amount of radioactive material within the inner surface of the detector has been well covered [74], while the investigation of radon removal from the gaseous volume is described in Chapter 6. Both of these studies are critical in achieving low-sensitivities with the SPC and potentially discovery a long sought-after DM particle.

7.1 QUADIS Parameter Optimization

The optimization of several processing parameters for the QUADIS software used with NEWS-G are necessary to ensure the consistency of the data being analyzed throughout the collaboration. Using the analysis of ^{37}Ar calibration data collected at the LSM facility, the value of two highly influential processing parameters were optimized. The optimal value for the integration window width is between 1000 and 1100 samples, while the best start sample location for that window is at 3833 samples. These values were found to optimize each recorded pulse while minimizing any background activity present in the data.

The implementation with this parameter optimization method can be applied to any calibration run in the same way. If there are events in the detector with a well-known energy, the events can be isolated and appropriate parameters can be found. This process can also be automated so that an optimized data set is produced after a calibration run has completed. While the automation of this process may be more involved at first, the groundwork has been laid for this to occur.

7.2 Radon Trapping

Mitigation of radon gas within the volume of the detector will reduce the detector background activity, allowing for low-energy rare-event searches to take place in the SNOLAB facility. To ensure that the radon mitigation system is optimized to produce ideal conditions for the detector gas, a variety of gases and radon trapping materials were tested at different temperatures using an apparatus (the RTS) that I designed and constructed. Several parameters of the GHS and NEWS-G detector were taken into consideration during the testing, like the flow rate and gas composition.

By testing at two different temperatures, it was shown that there is a marked improvement when the trapping material is cooled using dry ice to around -80°C. Through the comparison of two different porous material types, activated charcoal and silver zeolite, it was found that silver zeolite outperforms activated charcoal at room temperature. Further testing is required of the zeolite material but the results so far show promise for its use in radon trapping applications.

The materials were also proven to adsorb methane, a gas critical for the operation of the SPC detector. The measurements concerning the adsorption of methane

in Carboxen indicate that extra measures must be implemented to ensure that a proper concentration of methane is injected into the metal sphere. The BGA played a pivotal role in monitoring gas purity and relative gas concentrations in a binary gas mixture and the use of such a system is recommended for the NEWS-G Gas Handling System. Work is also being done in the Piro Lab to investigate the use of laser spectroscopy to monitor the absolute amount of methane found in gas mixtures. The method being researched involves monitoring methane through its adsorption of infrared light produced by a laser. By using a photodetector to determine the amount of light absorbed as it passes through the gas, the absolute concentration of methane can be determine with an accuracy on the order of 1 ppm.

Due to several time and lab constraints, repeat testing of the experiments discussed in Chapter 6 were not possible and more testing is required to confirm some of the discussed results. Several additions can also be made to the RTS to provide further data such as a flow meter and a more sensitive radon activity measurement device. The sphere being commissioned in the Piro Lab at the University of Alberta is already a prime candidate a radon detector that can be easily connected to the RTS to replace the RAD7. The flow meter will provide better information on the flow rate of the primary gas and calculations similar to those presented in Abe *et al* [98] can be done for different gases, trapping materials, and trap temperatures.

Other materials may also be of interest to determine their ability to trap radon, as well as other gases like methane. While silver zeolite was used in this research, other zeolites may provide varying levels of performance. Cooperation with Extraordinary Adsorbents in Edmonton offers a host of new types of materials, both zeolite and otherwise, to test. Polycrystalline metals like copper and nickel have shown high affinities for radon adsorption at temperatures below $-100°C$ and could be interesting radon trapping candidates [92]. Since low temperatures are needed for radon to be significantly mitigated, an improved cooling system is required for the NEWS-G installation at SNOLAB. Having such a system would allow for studies into the optimal temperature to remove radon without adsorbing methane.

Bibliography

[1] Gianfranco Bertone and David Merritt. "Dark matter dynamics and indirect detection". In: *Modern Physics Letters A* 20.14 (2005), pp. 1021–1036.

[2] *NEWS-G @ SNOLAB*. NEWS-G. Apr. 23, 2017. URL: https://news-g.org/news-snolab/ (visited on 06/17/2021).

[3] Kenneth S Krane. *Modern physics*. John Wiley & Sons, 2019.

[4] Gianfranco Bertone and Dan Hooper. "A History of Dark Matter". In: *Reviews of Modern Physics* 90.4 (Oct. 15, 2018), p. 045002. ISSN: 0034-6861, 1539-0756. DOI: 10.1103/RevModPhys.90.045002. arXiv: 1605.04909. URL: http://arxiv.org/abs/1605.04909 (visited on 05/11/2021).

[5] Edvige Corbelli and Paolo Salucci. "The extended rotation curve and the dark matter halo of M33". In: *Monthly Notices of the Royal Astronomical Society* 311.2 (2000), pp. 441–447.

[6] Henri Poincaré. "La voie lactée et la théorie des gaz". In: *Bulletin de la société astronomique de France* 20 (1906), pp. 153–165.

[7] JC Kapteyn. "First attempt at a theory of the arrangement and motion of the sidereal system, May 1922". In: *ApJ* 55 ().

[8] J. H. Oort. "The force exerted by the stellar system in the direction perpendicular to the galactic plane and some related problems". In: *Bulletin of the Astronomical Institutes of the Netherlands*. Vol. 6. North Holland Publishing Company, 1932, p. 249. URL: https://hdl.handle.net/1887/6025 (visited on 05/11/2021).

[9] Edwin Hubble and Milton L Humason. "The velocity-distance relation among extra-galactic nebulae". In: *The Astrophysical Journal* 74 (1931), p. 43.

[10] Fritz Zwicky. "The redshift of extragalactic nebulae". In: *Helvetica Physica Acta* 6 (1933), pp. 110–127.

[11] Fritz Zwicky. "On the Masses of Nebulae and of Clusters of Nebulae". In: *The Astrophysical Journal* 86 (1937), p. 217.

[12] Wendy L Freedman et al. "The Carnegie-Chicago Hubble program. VIII. An independent determination of the Hubble constant based on the tip of the red giant branch". In: *The Astrophysical Journal* 882.1 (2019), p. 34.

[13] Horace W Babcock. "The rotation of the Andromeda Nebula". In: *Lick Observatory Bulletin* 19 (1939), pp. 41–51.

[14] Jan Hendrik Oort. "Some problems concerning the structure and dynamics of the galactic system and the elliptical nebulae NGC 3115 and 4494". In: *Astrophysical Journal* (1940), pp. 91–273.

[15] Vera C Rubin and W Kent Ford Jr. "Rotation of the Andromeda nebula from a spectroscopic survey of emission regions". In: *The Astrophysical Journal* 159 (1970), p. 379.

[16] Vera C Rubin, W Kent Ford Jr, and Norbert Thonnard. "Rotational properties of 21 SC galaxies with a large range of luminosities and radii, from NGC 4605(R= 4kpc) to UGC 2885(R= 122 kpc)". In: *The Astrophysical Journal* 238 (1980), pp. 471–487.

[17] Keren Sharon et al. "Discovery of multiply imaged galaxies behind the cluster and lensed quasar SDSS J1004+ 4112". In: *The Astrophysical Journal Letters* 629.2 (2005), p. L73.

[18] Naohisa Inada et al. "A gravitationally lensed quasar with quadruple images separated by 14.62 arcseconds". In: *Nature* 426.6968 (2003), pp. 810–812.

[19] Douglas Clowe et al. "A direct empirical proof of the existence of dark matter". In: *The Astrophysical Journal Letters* 648.2 (2006), p. L109.

[20] DJ Fixsen et al. "The cosmic microwave background spectrum from the full cobe* firas data set". In: *The Astrophysical Journal* 473.2 (1996), p. 576.

[21] Nabila Aghanim et al. "Planck 2018 results-VI. Cosmological parameters". In: *Astronomy & Astrophysics* 641 (2020), A6.

[22] Ruth Durrer. "The cosmic microwave background: the history of its experimental investigation and its significance for cosmology". In: *Classical and Quantum Gravity* 32.12 (2015), p. 124007.

[23] Planck Collaboration et al. "Planck 2015 results. XIII. Cosmological parameters". In: *Astronomy & Astrophysics* 594 (Oct. 2016), A13. ISSN: 0004-6361, 1432-0746. DOI: 10.1051/0004-6361/201525830. arXiv: 1502.01589. URL: http://arxiv.org/abs/1502.01589 (visited on 05/12/2021).

[24] Herbert Jesse Rood. "The Dynamics of the Coma Cluster of Galaxies." In: *Ph. D. Thesis* (1965).

[25] Simon DM White. "Mass segregation and missing mass in the Coma cluster". In: *Monthly Notices of the Royal Astronomical Society* 179.2 (1977), pp. 33–41.

[26] John F Meekins et al. "Physical sciences: X-rays from the coma cluster of galaxies". In: *Nature* 231.5298 (1971), pp. 107–108.

[27] Marco Battaglieri et al. "US cosmic visions: new ideas in dark matter 2017: community report". In: *arXiv preprint arXiv:1707.04591* (2017).

[28] Jihn E Kim and Gianpaolo Carosi. "Axions and the strong C P problem". In: *Reviews of Modern Physics* 82.1 (2010), p. 557.

[29] Ken Croswell. *The universe at midnight: Observations illuminating the cosmos*. Simon and Schuster, 2002.

[30] C Alcock et al. "The MACHO Project Large Magellanic Cloud microlensing results from the first two years and the nature of the galactic dark halo". In: *The Astrophysical Journal* 486.2 (1997), p. 697.

[31] Charles Alcock et al. "The MACHO project: microlensing results from 5.7 years of Large Magellanic Cloud observations". In: *The Astrophysical Journal* 542.1 (2000), p. 281.

[32] Clyde L Cowan et al. "Detection of the free neutrino: a confirmation". In: *Science* 124.3212 (1956), pp. 103–104.

[33] SS Gershtein and YB Zeldovich. "GERSHTEIN 1966". In: *Pisma Zh. Eksp. Teor. Fiz* 4 (1966), p. 174.

[34] Max Aker et al. "Improved upper limit on the neutrino mass from a direct kinematic method by KATRIN". In: *Physical review letters* 123.22 (2019), p. 221802.

[35] Andrzej K Drukier, Katherine Freese, and David N Spergel. "Detecting cold dark-matter candidates". In: *Physical Review D* 33.12 (1986), p. 3495.

[36] Stefano Giagu. "WIMP dark matter searches with the ATLAS detector at the LHC". In: *Frontiers in Physics* 7 (2019), p. 75.

[37] WB Atwood et al. "The large area telescope on the Fermi gamma-ray space telescope mission". In: *The Astrophysical Journal* 697.2 (2009), p. 1071.

[38] Oscar Adriani et al. "An anomalous positron abundance in cosmic rays with energies 1.5–100 GeV". In: *Nature* 458.7238 (2009), pp. 607–609.

[39] Christoph Weniger. "A tentative gamma-ray line from dark matter annihilation at the Fermi Large Area Telescope". In: *Journal of Cosmology and Astroparticle Physics* 2012.08 (2012), p. 007.

[40] R Abbasi et al. "Multiyear search for dark matter annihilations in the Sun with the AMANDA-II and IceCube detectors". In: *Physical Review D* 85.4 (2012), p. 042002.

[41] Gordon Kane and Scott Watson. "Dark matter and LHC: What is the connection?" In: *Modern Physics Letters A* 23.26 (2008), pp. 2103–2123.

[42] Mark W Goodman and Edward Witten. "Detectability of certain dark-matter candidates". In: *Physical Review D* 31.12 (1985), p. 3059.

[43] Jonathan Engel, Stuart Pittel, and Petr Vogel. "Nuclear physics of dark matter detection". In: *International Journal of Modern Physics E* 1.01 (1992), pp. 1–37.

[44] SP Ahlen et al. "Limits on cold dark matter candidates from an ultralow background germanium spectrometer". In: *Physics Letters B* 195.4 (1987), pp. 603–608.

[45] Celine Bœhm et al. "How high is the neutrino floor?" In: *Journal of Cosmology and Astroparticle Physics* 2019.01 (2019), p. 043.

[46] J Cooley. "Overview of non-liquid noble direct detection dark matter experiments". In: *Physics of the Dark Universe* 4 (2014), pp. 92–97.

[47] R Agnese et al. "Projected Sensitivity of the SuperCDMS SNOLAB experiment". In: *Physical Review D* 95.8 (2017), p. 082002.

[48] C Amole et al. "PICASSO, COUPP and PICO-search for dark matter with bubble chambers". In: *EPJ Web of Conferences*. Vol. 95. EDP Sciences. 2015, p. 04020.

[49] Mark Guy Boulay, Deap Collaboration, et al. "DEAP-3600 dark matter search at SNOLAB". In: *Journal of Physics: Conference Series*. Vol. 375. 1. IOP Publishing. 2012, p. 012027.

[50] LJ Flores et al. "Physics reach of a low threshold scintillating argon bubble chamber in coherent elastic neutrino-nucleus scattering reactor experiments". In: *Physical Review D* 103.9 (2021), p. L091301.

[51] Ioannis Giomataris et al. "A novel large-volume spherical detector with proportional amplification read-out". In: *Journal of Instrumentation* 3.09 (2008), P09007.

[52] NJT Smith. "The SNOLAB deep underground facility". In: *The European Physical Journal Plus* 127.9 (2012), pp. 1–8.

[53] Quentin Arnaud et al. "First results from the NEWS-G direct dark matter search experiment at the LSM". In: *Astroparticle Physics* 97 (2018), pp. 54–62.

[54] Georges Charpak et al. "The use of multiwire proportional counters to select and localize charged particles". In: *Nuclear Instruments and Methods* 62.3 (1968), pp. 262–268.

[55] Glenn F Knoll. *Radiation detection and measurement*. John Wiley & Sons, 2010.

[56] Hans Frischholz. *Generation and distribution of radio-frequency power in LEP*. Tech. rep. 1985.

[57] Craig E Aalseth et al. "A shallow underground laboratory for low-background radiation measurements and materials development". In: *Review of Scientific Instruments* 83.11 (2012), p. 113503.

[58] Q Arnaud et al. "Spherical Proportional Counter: A review of recent developments". In: *Journal of Physics: Conference Series*. Vol. 1029. 1. IOP Publishing. 2018, p. 012006.

[59] Kai Siegbahn. "Book Review: Radiation Detection and Measurement, by Glenn Knoll; Wiley, New York, 2000; Price (hardcover), US 98.95; ISBN: 0-471-07338-5". In: *Nuclear Instruments and Methods in Physics Research A* 454.2-3 (2000), pp. 528–529.

[60] J. Derré. "Pulse shape in the SPC prototype". 2007. URL: `https://newsgorg.files.wordpress.com/2018/07/pulse-shape-in-the-spc-prototype.pdf` (visited on 08/08/2021).

[61] D Combecher. "Measurement of W values of low-energy electrons in several gases". In: *Radiation Research* 84.2 (1980), pp. 189–218.

[62] Ioannis Katsioulas, Patrick Knights, and Konstantinos Nikolopoulos. "Estimation of the ionisation quenching factor in gases from W-value measurements". In: *arXiv preprint arXiv:2105.01414* (2021).

[63] Daniel Durnford. *A Novel Approach to Account for the Fano Factor*. Presented at the CAP Congress, Halifax. 2018.

[64] P-A Amaudruz et al. "First results from the DEAP-3600 dark matter search with argon at SNOLAB". In: *Physical review letters* 121.7 (2018), p. 071801.

[65] Ioannis Katsioulas, NEWS-G collaboration, et al. "Recent advancements of the NEWS-G experiment". In: *Journal of Physics: Conference Series*. Vol. 1468. 1. IOP Publishing. 2020, p. 012058.

[66] A Giganon et al. "A multiball read-out for the spherical proportional counter". In: *Journal of Instrumentation* 12.12 (2017), P12031.

[67] P Knights, Konstantinos Nikolopoulos, and Marie-Cécile Piro. "NEWS-G: Search for Light Dark Matter with a Spherical Proportional Counter". In: *40th International Conference on High Energy Physics*. 2020, p. 639.

[68] Shinzou Kubota. "Non-metastable Penning effect in the alpha-particle ionization of inert gas mixtures". In: *Journal of the Physical Society of Japan* 29.4 (1970), pp. 1017–1029.

[69] Kenneth S Krane and Kenneth S Krane. *Modern physics*. Wiley New York, 1996.

[70] Alan D McNaught, Andrew Wilkinson, et al. *Compendium of chemical terminology*. Vol. 1669. Blackwell Science Oxford, 1997.

[71] D.J. Griffiths. *Introduction to Electrodynamics*. Cambridge University Press, 2017. ISBN: 978-1-108-35714-2. URL: https://books.google.ca/books?id=Kh4xDwAAQBAJ.

[72] Stephen Hawking. *The Dreams That Stuff Is Made Of: The Most Astounding Papers of Quantum Physics–and How They Shook the Scientific World*. Running Press Adult, 2011.

[73] DG Kelly et al. "The production of Ar-37 using a thermal neutron reactor flux". In: *Journal of Radioanalytical and Nuclear Chemistry* 318.1 (2018), pp. 279–285.

[74] NEWS-G. Collaboration et al. "Copper electroplating for background suppression in the NEWS-G experiment". In: *arXiv:2008.03153 [astro-ph, physics:hep-ex, physics:physics]* (Aug. 7, 2020). arXiv: 2008.03153. URL: http://arxiv.org/abs/2008.03153 (visited on 08/11/2020).

[75] National Nuclear Data Center. *NuDat 2.8 Chart of Nuclides*. 2021. URL: https://www.nndc.bnl.gov/nudat2/ (visited on 06/17/2021).

[76] Eric W Hoppe et al. "Cleaning and passivation of copper surfaces to remove surface radioactivity and prevent oxide formation". In: *Nuclear Instruments and Methods in Physics Research Section A: Accelerators, Spectrometers, Detectors and Associated Equipment* 579.1 (2007), pp. 486–489.

[77] S Davies, JA Rees, and DL Seymour. "Threshold ionisation mass spectrometry (TIMS); a complementary quantitative technique to conventional mass resolved mass spectrometry". In: *Vacuum* 101 (2014), pp. 416–422.

[78] A Alessandrello et al. "Measurements of internal radioactive contamination in samples of Roman lead to be used in experiments on rare events". In: *Nuclear Instruments and Methods in Physics Research Section B: Beam Interactions with Materials and Atoms* 142.1-2 (1998), pp. 163–172.

[79] A. Brossard. "Optimization of spherical proportional counter backgrounds and response for low mass dark matter search". PhD thesis. Queen's University and Université Paris-Saclay, 2020.

[80] F. Vazquez de Sola Fernandez. "Solar KK Axion search with NEWS-G". PhD thesis. Queen's University, 2020.

[81] *Swiss Army knife for engineers*. 2021. URL: https://redpitaya.com/ (visited on 08/09/2021).

[82] E Armengaud et al. "Performance of the EDELWEISS-III experiment for direct dark matter searches". In: *Journal of Instrumentation* 12.08 (2017), P08010.

[83] Rene Brun and Fons Rademakers. "ROOT—An object oriented data analysis framework". In: *Nuclear Instruments and Methods in Physics Research Section A: Accelerators, Spectrometers, Detectors and Associated Equipment* 389.1-2 (1997), pp. 81–86.

[84] Robert W Kiser and WH Johnston. "The Radioactivity of Argon-371, 2". In: *Journal of the American Chemical Society* 81.8 (1959), pp. 1810–1813.

[85] PW Dougan, KWD Ledingham, and RWP Drever. "The L/K-capture ratio of argon 37". In: *Philosophical Magazine* 7.75 (1962), pp. 475–482.

[86] Georges Audi et al. "The NUBASE evaluation of nuclear and decay properties". In: *Nuclear physics A* 729.1 (2003), pp. 3–128.

[87] NEWS-G. Collaboration et al. "Precision laser-based measurements of the single electron response of SPCs for the NEWS-G light dark matter search experiment". In: *Physical Review D* 99.10 (May 20, 2019), p. 102003. ISSN: 2470-0010, 2470-0029. DOI: 10.1103/PhysRevD.99.102003. arXiv: 1902.08960. URL: http://arxiv.org/abs/1902.08960 (visited on 11/13/2019).

[88] Pauli Virtanen et al. "SciPy 1.0: Fundamental Algorithms for Scientific Computing in Python". In: *Nature Methods* 17 (2020), pp. 261–272. DOI: 10.1038/s41592-019-0686-2.

[89] Paul R Fields, Lawrence Stein, and Moshe H Zirin. "Radon fluoride". In: *Journal of the American Chemical Society* 84.21 (1962), pp. 4164–4165.

[90] Brookhaven National Laboratory National Nuclear Data Center. *NuDat (Nuclear Structure and Decay Data)*. Mar. 2008.

[91] Cathleen Fry and Michael Thoennessen. "Discovery of the astatine, radon, francium, and radium isotopes". In: *Atomic Data and Nuclear Data Tables* 99.5 (2013), pp. 497–519.

[92] R. Eichler and M. Schädel. "Adsorption of Radon on Metal Surfaces: A Model Study for Chemical Investigations of Elements 112 and 114". In: *The Journal of Physical Chemistry B* 106.21 (May 2002), pp. 5413–5420. ISSN: 1520-6106, 1520-5207. DOI: 10.1021/jp015553q. URL: https://pubs.acs.org/doi/10.1021/jp015553q (visited on 01/23/2020).

[93] I Bikit et al. "Radon adsorption by zeolite". In: *Radiation Measurements* 72 (2015), pp. 70–74.

[94] Bernard L Cohen and Ernest S Cohen. "Theory and practice of radon monitoring with charcoal adsorption." In: *Health Physics* 45.2 (1983), pp. 501–508.

[95] Raymond Noel et al. "Measuring and understanding radon adsorption in microporous materials". In: *AIP Conference Proceedings*. Vol. 1672. 1. AIP Publishing LLC. 2015, p. 070001.

[96] Lu Guo et al. "The temperature dependence of adsorption coefficients of 222Rn on activated charcoal: an experimental study". In: *Applied Radiation and Isotopes* 125 (2017), pp. 185–187.

[97] P-A Amaudruz et al. "Radon backgrounds in the DEAP-1 liquid-argon-based Dark Matter detector". In: *Astroparticle Physics* 62 (2015), pp. 178–194.

[98] K. Abe et al. "Radon removal from gaseous xenon with activated charcoal". In: *Nuclear Instruments and Methods in Physics Research Section A: Accelerators, Spectrometers, Detectors and Associated Equipment* 661.1 (Jan. 1, 2012), pp. 50–57. ISSN: 0168-9002. DOI: 10.1016/j.nima.2011.09.051. URL: http://www.sciencedirect.com/science/article/pii/S0168900211018468 (visited on 02/20/2020).

[99] K Pushkin et al. "Study of radon reduction in gases for rare event search experiments". In: *Nuclear Instruments and Methods in Physics Research Section A: Accelerators, Spectrometers, Detectors and Associated Equipment* 903 (2018), pp. 267–276.

[100] J. Busto. "Radon adsorption in nanoporous carbon materials". Low Radioactivity Techniques - LRT 2013. 2013. URL: https://agenda.infn.it/event/5248/contributions/57602/ (visited on 07/29/2021).

[101] *High Purity Carbon Adsorbents for Sample Preparation and Chromatographic Applications*. URL: https://www.sigmaaldrich.com/CA/en/technical-documents/technical-article/analytical-chemistry/purification/high-purity-carbon-adsorbents (visited on 07/28/2021).

[102] Steven M Kuznicki et al. "Xenon adsorption on modified ETS-10". In: *The Journal of Physical Chemistry C* 111.4 (2007), pp. 1560–1562.

[103] SNOLAB. *SNOLAB Gamma Counter 2 (Canberra Well Detector) Results*. 2021. URL: https://www.snolab.ca/users/services/gamma-assay/Canberra_Well_newsg_master.html (visited on 09/21/2021).

[104] N Karunakara et al. "Evaluation of radon adsorption characteristics of a coconut shell-based activated charcoal system for radon and thoron removal applications". In: *Journal of Environmental Radioactivity* 142 (2015), pp. 87–95.

[105] *RAD7 Electronic Radon Detector User Manual*. English. DURRIDGE Company Inc. June 22, 2021. URL: https://durridge.com/documentation/RAD7%20Manual.pdf (visited on 07/30/2021).

[106] J. Busto. "Adsorption of radioactive noble gases in microporous materials". GDR Neutrino (NEUTRINO Research Group) Meeting. 2019. URL: https://indico.in2p3.fr/event/19474/contributions/75247/ (visited on 07/28/2021).

Appendix A

Data Cuts

The data cuts below were applied during the QUADIS processing parameter optimization process for the tj13s000 run. These removed unwanted events that were not relevant to the 2.8 keV decay energy of ^{37}Ar. Cuts that use the term "raw" refer to values obtained from the raw pulse. Other values like the amplitude are obtained for the doubly deconvolved data. These cuts were produced by the NEWS-G collaboration.

Cut Name	Explanation
Laser	Removes any laser channel events with an amplitude greater than 4500 ADU
Basic	Checks that the pulse has a width > 0, the start time $<$ stop time
zoomDD	Removes events with a rise time > 350 μs and with amplitude > 14000 ADU
PSD1	Pulse discrimination cut that ensure the raw width is between 140 and 500 samples, the raw rise time $< 500\mu$s, and the raw rise time:raw width < 1.1
PSD2	Limits the raw rise as (raw rise) < 1.875(raw width) -262.5
rise1	Limits the rise time between 10 and 50 μs
cross2	Limits the doubly deconvolved integral < 100000
northCut	Removes events that were only detected by the North channel
corrCut	A correction cut supplied by Daniel Durnford
KShell	A cut that isolates only 2.8 keV ^{37}Ar events

Table A.1: Cuts applied to the ^{37}Ar data analyzed in Chapter 4 with the pure methane run tj13s000.